A NOVEL CONCEPT FOR PHASE ERROR CORRECTION IN SUPERCONDUCTIVE UNDULATORS: THEORY AND EXPERIMENTAL VERIFICATION

Zur Erlangung des akademischen Grades eines
DOKTORS DER NATURWISSENSCHAFTEN
von der Fakultät Physik der Univeristät (TH)
Karlsruhe

genehmigte

DISSERTATION

von

Dipl.-Ing Daniel Wollmann
aus Dresden

Tag der mündlichen Prüfung: 12.12.2008

Referent: Prof. Dr.rer.nat. T. Baumbach

Korreferent: Prof. Dr.rer.nat. G. Quast

Abstract

Present synchrotron light sources make extensive use of insertion devices like wigglers, undulators or wavelength-shifters. Among these, undulators are the most advanced sources for the generation of synchrotron radiation. The photons generated by a single electron add up coherently along the electron trajectory. In order to do so the oscillatory motion of the electron has to be in phase with the emitted photons along the whole undulator. Small magnetic errors can cause unwanted destructive interferences. In standard permanent magnet undulators the magnetic errors are reduced by applying shimming techniques. Superconductive undulators have higher magnetic fields than permanent magnet undulators but shimming is more complex. In this thesis a novel passive shimming method based on superconductive closed loops is presented. It is shown that coupled superconductive loops installed along the surface of the superconductive undulator coil can significantly reduce the destructive effect of the field errors. The concept was verified by a proof of principle experiment.

Kurzfassung

In Synchrotronstrahlungsquellen wird die Strahlung, die von sogenannten *Insertion Devices* erzeugt wird, umfassend genutzt. Zu dieser Gruppe gehören Wiggler, Undulatoren und Wellenlängenschieber. Undulatoren sind dabei die am weitesten entwickelten Quellen zur Erzeugung von Synchrotronstrahlung. Die Photonen, die von einem Elektron auf seiner Trajektorie durch den Undulator erzeugt werden, können kohärent interferieren. Damit dies möglich ist, muss die oszillatorische Bewegung des Elektrons entlang des Undulators immer in Phase mit den emittierten Photonen sein. Kleine Fehler im Magnetfeld können dabei zu unerwünschter destruktiver Interferenz führen. In Permanentmagnet-Undulatoren werden die Feldfehler durch sogenanntes *Shimming* korrigiert. Supraleitende Undulatoren erreichen höhere Feldstärken als Permanentmagnet-Undulatoren, jedoch ist die Korrektur von Feldfehlern komplexer. In dieser Arbeit wird ein neuartiges, passives Shimming Konzept, das auf geschlossenen supraleitenden Schleifen basiert, vorgestellt. Mit Hilfe eines Experiments konnte gezeigt werden, dass ein gekoppeltes Schleifensystem die Feldfehler in einem Undulator signifikant reduzieren kann.

CONTENTS

1. INTRODUCTION

Light is the mostly used probe for studying the properties of matter. Since more than three decades, electron storage rings provide synchrotron radiation in a wide spectral range from hard X-rays to the far infrared. Except for the comparably narrow spectral region, where laser sources exist, storage ring synchrotron radiation sources exceed any other source in terms of *flux* ([photons/(s mm^2 mrad 0.1%BW)]), *brightness* ([photons/(s mrad^2 0.1%BW)]), and *brilliance*([photons/(s mm^2 mrad^2 0.1%BW)]) by far. As a consequence, synchrotron radiation is used for a huge field of applications. With hard X-ray methods, such as diffraction, scattering, reflection, absorption and fluorescence spectroscopy, materials and processes can be investigated. Soft X-rays are, for instance, used for lithography in micro/nanofabrication and for investigations of magnetic structures. In addition THz radiation is essentially non-destructive and can be used to yield spectroscopic fingerprints of molecules, allowing to single out species in imaging applications [Zha02]. Today, more than 70 synchrotron radiation facilities are in operation, under construction or in planning worldwide. A recent overview of facilities and applications can be found in [Mos04, MWY04, Lab].

Synchrotron radiation has first been observed in 1947 at the 70 MeV synchrotron of General Electric at Schenectady, New York. In the 1st generation of synchrotron radiation sources in the 1950s and 60s the users had only parasitic access to the accelerators built for high energy physics. With growing demand the 2nd generation of synchrotron radiation sources was built in the 1970s and early 80s. These sources were dedicated to the production of synchrotron radiation. Besides expanding the availability of synchrotron radiation, the development of new sources was focused on improving the quality of radiation. This led to the 3rd generation sources, which extensively use insertion devices like wigglers, undulators or wavelength-shifters to improve the *flux*, *brightness*, and *brilliance* of the synchrotron radiation.

Undulators are the most advanced sources of highly brilliant X-rays. Up to now mainly permanent magnet undulators are used. The magnetic field strength at a given undulator period length is limited by the material properties of the permanent magnets [BHK$^+$06]. In order to overcome these limits and thereby extend the accessible spectral range of synchrotron radiation, ideas were discussed to replace the permanent magnets by superconductive wires. After first experiments in the 1970's [Far80, ABB$^+$80] the development of superconductive undulators was resumed in the early 1990's [MKH91, BZJIW90]. In 1999, a superconductive undulator with a period length of 3.8 mm was built at the Forschungszentrum Karlsruhe and successfully tested at the Mainz Microtron MAMI [HHM$^+$99]. Soon after that a prototype with a period length $\lambda_u = 14$ mm and a length of 10 periods was built together with the industrial partner ACCEL Instruments [RMG$^+$02]. This was followed by the construction of a 50 period undulator for single pass accelerators (FELs) and, later, by a 100 period undulator for the ANKA storage ring, both with a period length of 14 mm. The latter was installed at ANKA in March 2005 [BHK$^+$06, CHK$^+$06]. It was shown that a narrow-gap superconductive undulator can be reliably operated in a storage ring under standard user operation conditions [KRH$^+$05]. This so-called SCU14 was the first superconductive undulator installed in a storage ring. Currently an improved superconductive undulator with a period length of 15 mm is under construction in collaboration with Babcock Noell GmbH, Würzburg, Germany, and will be installed at ANKA in 2009.

The spectral properties of the synchrotron radiation produced by an undulator depend mainly on the quality of the undulator magnetic field: amplitude and phase of the magnetic field must be within small tolerances over the complete length of the undulator. The field quality is quantified by the so-called phase error. Techniques for phase error correction, the so-called shimming, of permanent magnet undulators with magnetized metal strips are state of the art. For superconductive undulators shimming with additional superconductive correction coils was proposed and experimentally tested [CRS$^+$03, PDB$^+$05, Wol05, WBC$^+$06].

In the first part of this thesis the influence of mechanical tolerances on the phase error of superconducting undulators is investigated. In the second part active shimming methods to compensate field errors using correction coils are studied. With these classical methods shimming is an iterative and time consuming process of measuring, applying shim coils and verifying the improved field quality. In the third part a novel shimming concept based on superconductive closed-loops is presented [WBR08, WBP$^+$08c, WBP$^+$08b]. This novel concept automatically minimizes field errors. The system works in the following way: high temperature superconductive closed-loops on top of the undulator coils enclose one or several undulator periods. In case each of the enclosed poles produces a perfect field (no phase error) the integral magnetic flux through the loops is zero and the induced current into the loop is zero. As soon as the field in one of the poles deviates from its ideal value a current is induced in the loop which compensates the field deviation.

This concept was verified in a proof of principle experiment and the results of this experiment are explained and summarized at the end of this thesis.

2. SYNCHROTRON RADIATION AND INSERTION DEVICES

The angular distribution of the synchrotron radiation emitted by an electron moving in a storage ring light source with a velocity $v \sim c$ can be derived by transforming the relativistic motion of the electron into its rest frame. The bending magnets accelerate the electron and the accelerated charged particle emits electromagnetic radiation mainly perpendicular to its acceleration vector. In the electron's rest frame the angular distribution of the radiation is identical with the angular distribution of a Hertz dipole ($\cos^2 \Theta$). In the laboratory frame, due to the Lorentz boost, this axial symmetrical radiation distribution is collimated into the forward direction. This radiation cone has an rms opening angle of $\Theta'_{rms} \approx \frac{1}{\gamma}$ [Wil92a, Wie03a]. This behaviour is sketched in figure 2.1. At the ANKA energy of 2.5 GeV and $\gamma = 5000$ the opening angle is $\Theta'_{rms} \approx 0.2\,\mathrm{mrad}$. The power of the emitted synchrotron radiation is

$$P_\gamma \propto \frac{E^4}{\rho^2}, \tag{2.1}$$

with the particle energy E and the bending radius ρ.
The spectrum covers a wide range of wavelengths used from the far infrared to hard X-rays and is characterized by the so-called critical frequency

$$\omega_c = \frac{3}{2} c \frac{\gamma^3}{\rho}. \tag{2.2}$$

The critical frequency divides the integrated radiation power into two equal parts [Wil92a, Wie03a]. The radiation spectrum of the ANKA bending magnets, with the critical photon energy $\epsilon_c = \hbar\omega_c = 6.29\,\mathrm{keV}$ is shown in figure 2.2. The parameters of the electron storage ring ANKA are listed in table 2.1.

To improve the quality of the synchrotron radiation and to meet the needs of different applications, insertion devices are extensively used in third generation synchrotron light sources. These insertion devices are installed in the straight sections

Energy	2.48 GeV
Circumference	110.4 m
Emittance	50 nmrad
Dipole radius	5.559 m
Dipole field	1.5 T
Maximum beam current	200 mA

Tab. 2.1: Technical parameters of the electron storage ring ANKA.

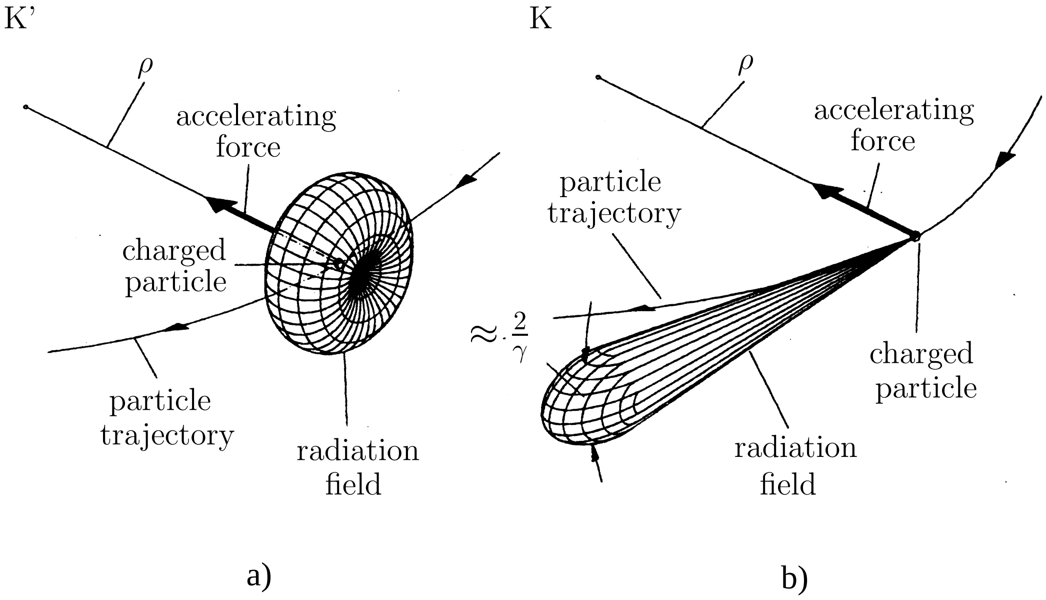

Fig. 2.1: Angular distribution of the electro-magnetic radiation emitted by a transversely accelerated relativistic charged particle: a) in its rest frame K'; b) in the laboratory system K. after [Wil92a]

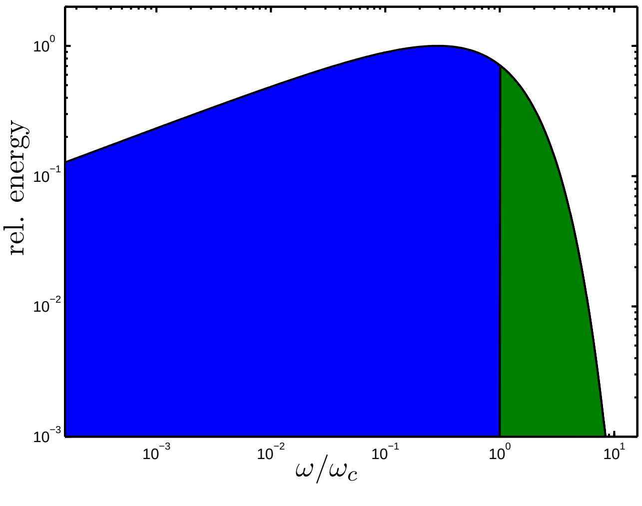

Fig. 2.2: Synchrotron radiation spectrum of the ANKA bending magnets. Courtesy A.-S. Mueller

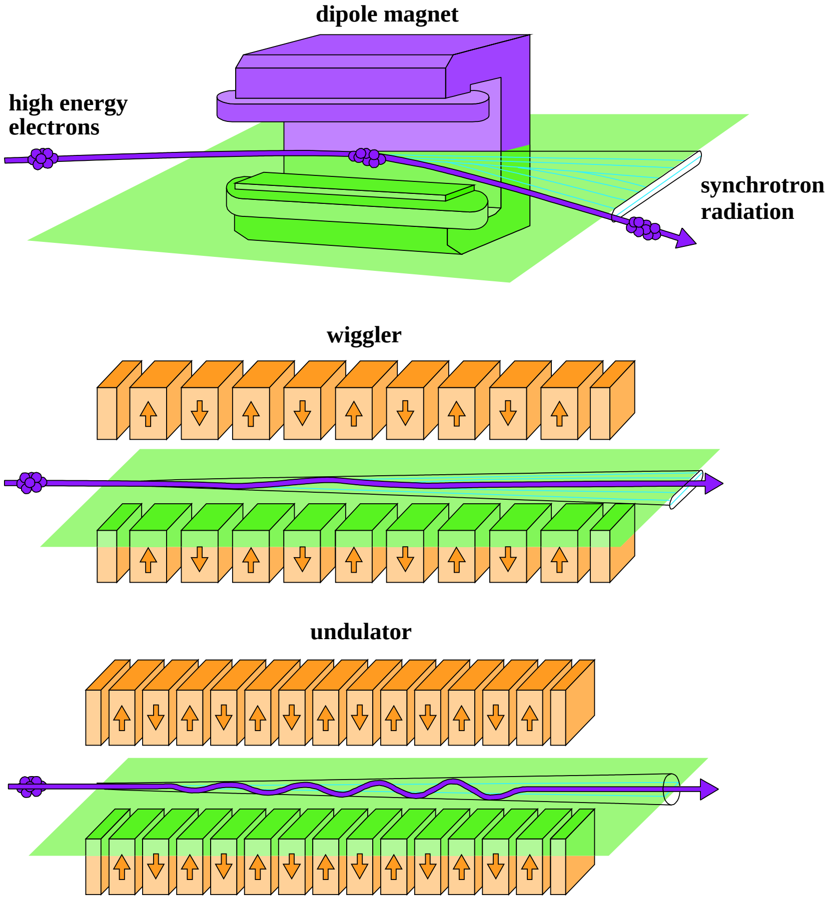

Fig. 2.3: The three main sources for synchrotron radiation: bending magnet (top), wiggler (center), undulator (bottom). Courtesy ESRF.

of synchrotron radiation sources. The group of insertion devices includes wigglers, undulators and wavelength-shifters. Figure 2.3 shows a comparison of the three main sources - bending magnets, wigglers and undulators - of synchrotron radiation in current light sources. A comparison of the calculated spectra emitted by an ANKA bending magnet, an ANKA wiggler and the ANKA superconductive undulator (SCU14) is plotted in figure 2.4. Comparable to bending magnets wigglers emit also a broad spectrum. The intensity of the radiation emitted by a wiggler increases linearly with the number of periods n. Due to interference the emitted photons in an undulator are concentrated in sharp lines. The intensity in the first harmonic is increased by n^2 compared to a bending magnet, where n is the number of undulator periods.

A detailed discussion of the physics of synchrotron radiation can be found in [Hof04, Wie03b, Wie03c, Wil92b].

In the following the undulator concept is discussed briefly.

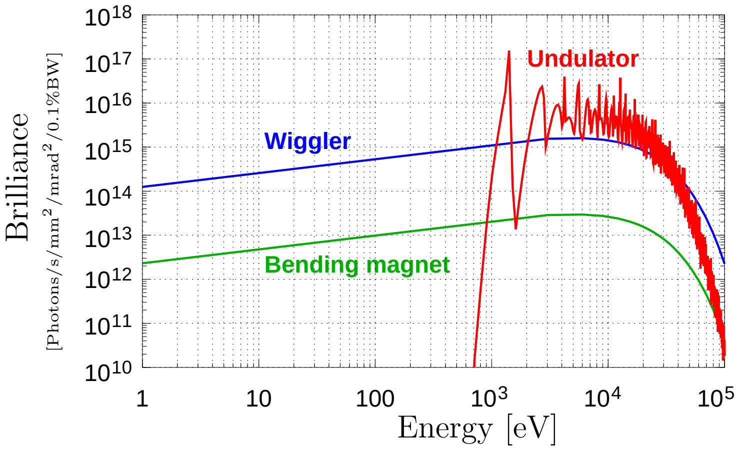

Fig. 2.4: Comparison of the calculated radiation spectra emitted by an ANKA bending magnet, an ANKA wiggler and the ANKA SCU14. Courtesy R. Butzbach.

2.1 Types of undulators

All different types of undulators, permanent magnet undulators, normal conducting and superconductive undulators, consist of two arrays of equidistantly spaced magnet poles. Figure 2.5 shows the inner part of a superconductive undulator with the superconductive wire bundles (red), the current direction in the wire bundles (arrows), the iron body and poles (green) and the electron trajectory (blue). The superconductive wire bundles consist of several electrically insulated parallel wires. Figure 2.5 was produced with the finite element program Opera-3D [VF], which allows to compute magnetic fields. A schematic drawing of a permanent magnet undulator is shown in figure 2.6. Permanent magnet undulators are assembled from single magnet blocks. The arrows indicate the direction of the magnetization of each block. In hybrid undulators a combination of permanent magnets and iron poles increase the field on axis.

For a mathematical description in the following the cartesian coordinate system in the undulator with the origin and the x- and z-axis in the midplane as shown in figure 2.5 and 2.6 will be used. The z-axis is parallel to the beam, the y-axis is vertical and the x-axis horizontal.

The vertical magnetic field component of planar undulators varies with z. In the vicinity of the z-axis the longitudinal (B_z) and the transverse field components (B_x) are comparably weak. Therefore, in first order approximation the magnetic field in an undulator is

$$\mathbf{B} = \begin{pmatrix} 0 \\ B_y \\ 0 \end{pmatrix}$$

with $B_y(z) = \tilde{B}\cos(\frac{\lambda_u}{2\pi}z)$, where λ_u is the period length of the undulator (see figure 2.5) and $\tilde{B}$ is the amplitude of the magnetic field. $\tilde{B}$ depends mainly on the gap width g between the two undulator bars, the period length λ_u of the undulator and the properties of the magnetic material or the current density, respectively.

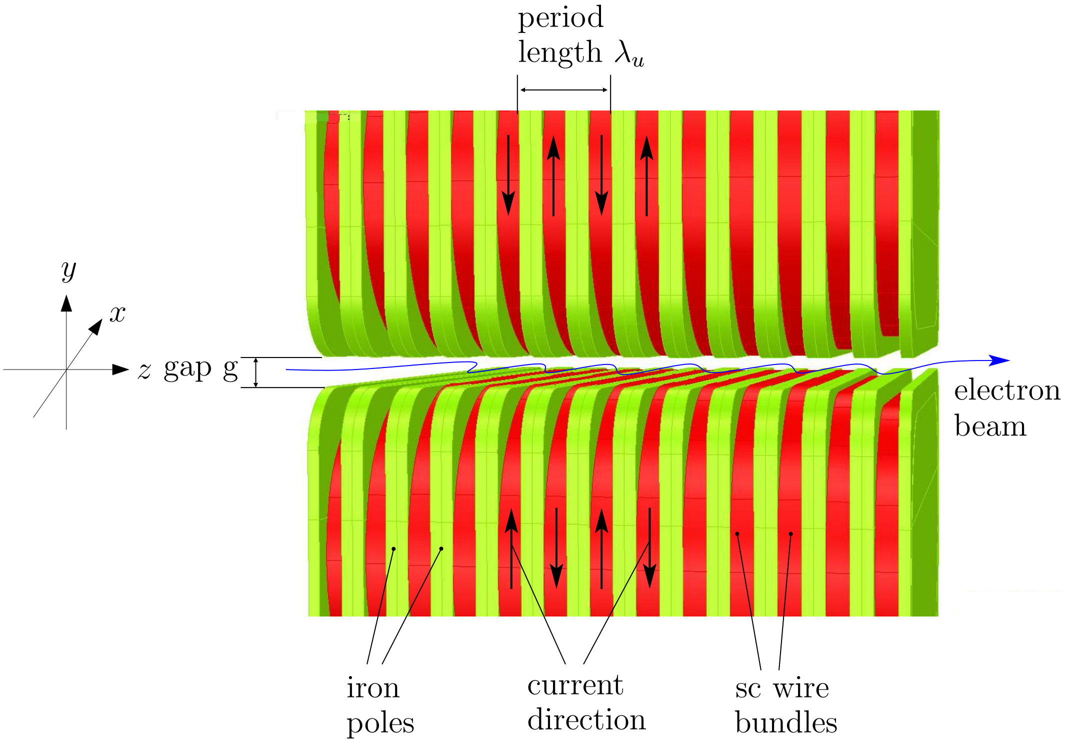

Fig. 2.5: Principle layout of a superconductive undulator, with iron poles and body (green), superconductive wire bundles (red), the electron trajectory (blue), the gap width g and the period length λ_u.

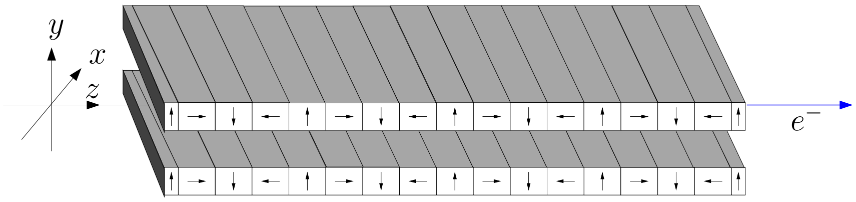

Fig. 2.6: Schematic drawing of a permanent-magnet undulator.

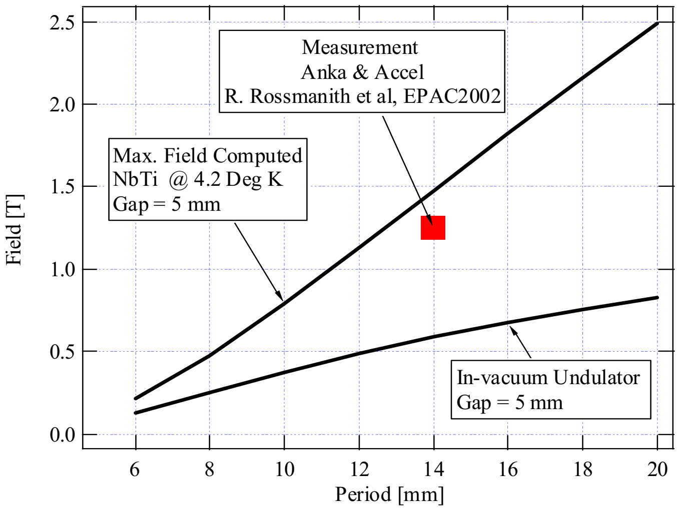

Fig. 2.7: Comparison of the achievable calculated maximum field strength for superconductive NbTi and in-vacuum permanent magnet undulators. The measured maximum magnetic field of the ANKA SCU14 is symbolized by the red square. [Ell03]

Most of the undulators in use are permanent magnet undulators. Superconductive undulators have, for a given gap width and a given period length, higher fields and can be tuned electrically. Figure 2.7 shows a comparison of the calculated maximum achievable field strength for superconductive NbTi undulators and permanent magnet undulators. The red square shows the measured maximum magnetic field strength of the SCU14 at ANKA.

2.2 Equations of motion for an electron in an undulator field

A relativistic electron traveling along the z-axis of an undulator oscillates in x-direction around the z-axis. This motion is caused by the Lorentz-force

$$\mathbf{F} = m_e \gamma \dot{\mathbf{v}} = e\mathbf{v} \times \mathbf{B}, \tag{2.3}$$

with $\gamma = \frac{1}{\sqrt{1-(\frac{|\mathbf{v}|}{c})^2}}$, the electron rest mass m_e, the electron charge e, the speed of light in vacuum c, the vector of the magnetic field of the undulator $\mathbf{B}$ and the vector of the electron velocity

$$\mathbf{v} = \begin{pmatrix} v_x \\ 0 \\ v_z \end{pmatrix}.$$

Equation 2.3 can be written as

$$\begin{pmatrix} \dot{v}_x \\ 0 \\ \dot{v}_z \end{pmatrix} = \frac{e}{m_e \gamma} \begin{pmatrix} -v_z B_y \\ 0 \\ v_x B_y \end{pmatrix}. \tag{2.4}$$

It is assumed that $v_z \gg v_x$ and $v_z \approx \beta c = const$, with $\beta = \frac{|\mathbf{v}|}{c}$ [KSW91, Wil92c]. Replacing the time by the variable z the equations of the electron motion in the undulator can be written as

$$\begin{aligned}
\frac{d^2}{dz^2}x(z) &= -\frac{e}{m_e\gamma\beta c}\cdot B_y = -\frac{e\tilde{B}}{m_e\gamma\beta c}\cdot\cos\left(\frac{2\pi}{\lambda_u}z\right), && (2.5)\\
\frac{d}{dz}x(z) &= -\frac{e}{m_e\gamma\beta c}\cdot I_1(z) = -\frac{e\tilde{B}\lambda_u}{2\pi m_e\gamma\beta c}\cdot\sin\left(\frac{2\pi}{\lambda_u}z\right), && (2.6)\\
x(z) &= -\frac{e}{m_e\gamma\beta c}\cdot I_2(z) = \frac{e\tilde{B}\lambda_u^2}{4\pi m_e\gamma\beta c}\cdot\cos\left(\frac{2\pi}{\lambda_u}z\right). && (2.7)
\end{aligned}$$

The first field integral

$$I_1(z) = \int\limits_{z_0}^{z} B_y(z')\,dz',$$

describes the deflection angle of the electron and the second field integral

$$I_2(z) = \iint\limits_{z_0}^{z} B_y(z')\,dz'^2$$

the displacement of the electron.

Insertion devices in storage rings have to be transparent to the beam, i.e. the transverse position and angle of the e-beam at the entrance and the exit of the device must be equal. This translates into the conditions

$$I_1(z) = \int\limits_{z_{entry}}^{z_{exit}} B_y(z')\,dz' = 0$$

and

$$I_2(z) = \iint\limits_{z_{entry}}^{z_{exit}} B_y(z')\,dz'^2 = 0.$$

The maximum deflection angle of an electron is

$$\Theta_w = \frac{d}{dz}x_{max}(z) = \frac{e\tilde{B}\lambda_u}{2\pi m_e\gamma\beta c}.$$

The deflection parameter K is

$$K = \frac{e\tilde{B}\lambda_u}{2\pi m_e c} = 0.0934\cdot\lambda_u[mm]\cdot\tilde{B}[T]. \tag{2.8}$$

With the assumption $\beta \approx 1$, the maximum deflection angle is

$$\Theta_w = \frac{1}{\gamma}K. \tag{2.9}$$

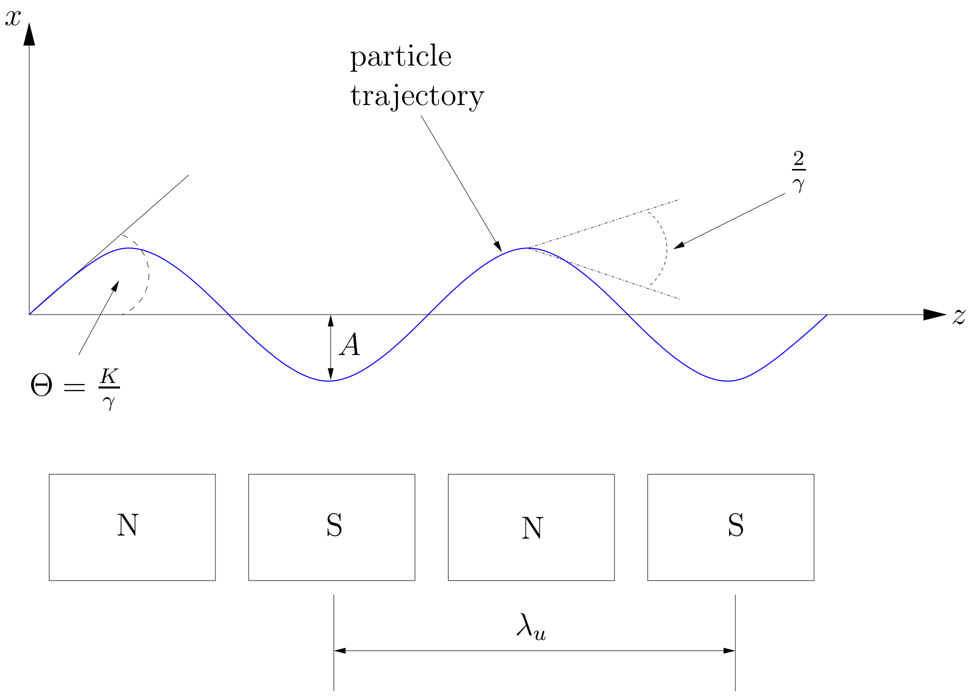

Fig. 2.8: Trajectory of an electron passing through the magnetic field of an undulator and emitting light into the forward direction.
Parameters are: the deflection parameter K, the maximum deflection angle Θ_w, the maximum electron displacement A and the relativistic factor γ.

By definition the maximum deflection angle of an electron in an undulator is relatively small compared to other insertion devices like wigglers [Mue05]. With $K \approx 1$ this yields

$$\Theta_w \sim \frac{1}{\gamma}.$$

Therefore light is emitted into a narrow forward cone. Figure 2.8 illustrates the electron trajectory, the deflection parameter K, the maximum deflection angle Θ_w and the emitted light cone with an opening angle of $1/\gamma$ [KSW91, Wil92c, Mue05, OE03].

2.3 Synchrotron radiation from undulators

The radiation emitted along the trajectory of an electron overlaps and can interfere [Jac99a, Hof04]. As a result an undulator emits a line spectrum, which is given by the undulator equation

$$\lambda_L = \frac{\lambda_u}{2k\gamma^2}\left(1 + \frac{K^2}{2} + \Theta^2\gamma^2\right). \tag{2.10}$$

k is the number of the harmonic and Θ the observation angle. It is important to note, that on axis, i.e. $\Theta = 0$, only odd harmonics are observed ($k = 1, 3, 5, ...$). Outside

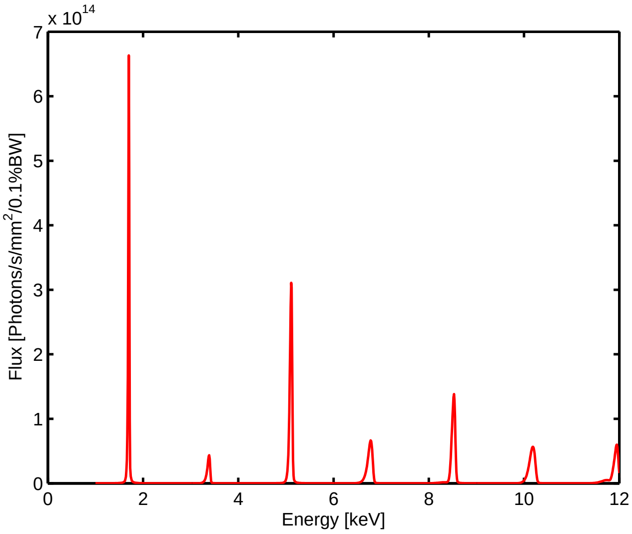

Fig. 2.9: Simulated radiation spectrum of a 100 period undulator with the period length $\lambda_u = 14\,\mathrm{mm}$, a peak field of $\tilde{B} = 1.3\,\mathrm{T}$ at an electron beam energy of $E = 2.48GeV$, a natural emittance of $\epsilon_x = 1\,\mathrm{nmrad}$ and a beam current of $I_{beam} = 100\,\mathrm{mA}$. The spectrum was calculated with the software SPECTRA for a pinhole of $1\,\mathrm{mm}^2$ in the distance of $30\,\mathrm{m}$. Courtesy F. Burkart and A. Bernhard

the axis, even harmonics are also present, with inferior spectral properties [Cla04a]. The undulator spectrum has its maximum at the fundamental wavelength ($k = 1$, $\Theta = 0$) [Wil92c]. The relative line width of the emitted spectrum is proportional to $1/n$, with n the number of periods of the undulator. The quality of the radiated spectrum also depends on the electron beam parameters especially the emittance, i.e. the phase space volume of the electron beam. Figure 2.9 shows the spectrum of a 100 period undulator with the period length $\lambda_u = 14\,\mathrm{mm}$ and a peak field of $\tilde{B} = 1.3\,\mathrm{T}$. The spectrum was calculated with the software SPECTRA [TK] for an electron beam with the energy $E = 2.48GeV$, a natural emittance $\epsilon_x = 1\,\mathrm{nmrad}$ and a beam current of $I_{beam} = 100\,\mathrm{mA}$. The graph shows the spectral flux through a $1\,\mathrm{mm}^2$ pinhole at a distance of $30\,\mathrm{m}$. Due to a finite angular acceptance and a finite e-beam emittance not only the odd harmonics but also Doppler peaks in front of the even harmonics can be seen. Figure 2.10 shows a measured spectrum of the ANKA SCU14 at a gap width $g = 8\,\mathrm{mm}$ and a coil current of $I = 500\,\mathrm{A}$, i.e. a field on axis of $\tilde{B} \approx 0.4\,\mathrm{T}$

From equation (2.10) it can be seen that the wavelength of the emitted radiation depends on the deflection parameter K and therefore on the amplitude of the magnetic field (see equation (2.8)). By increasing the amplitude of the magnetic field via increasing the current I in the superconductive undulator the wavelength of the emitted radiation is also increased ($\tilde{B} \sim I$). This is called *tuning*. Figure 2.11 shows the tuning curves of the SCU14 installed at ANKA assuming its design parameters (100 periods, $\lambda_u = 14\,\mathrm{mm}$, $K_{max} = 2$) and the ANKA beam parameters. Including the 7th harmonic a spectral range from about 1.4 keV to 29 keV is covered.

The combination of high photon energies, especially at higher harmonics, and

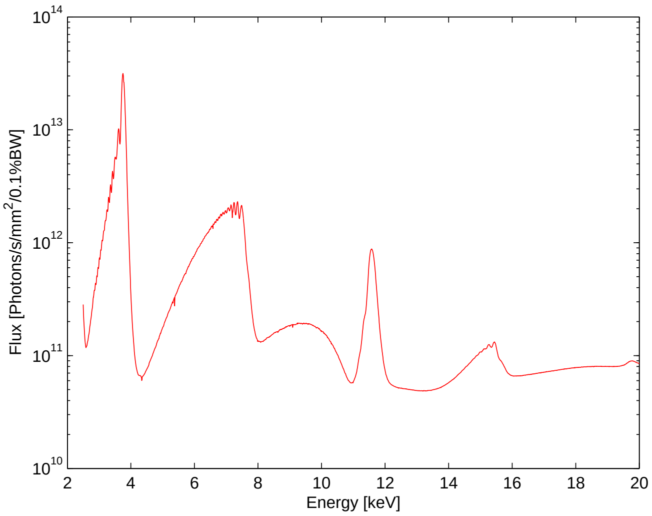

Fig. 2.10: Measured spectrum of the SCU14 installed at ANKA at a gap width $g = 8\,\mathrm{mm}$ and a coil current of $I = 500\,\mathrm{A}$. The flux through a $50\,\mu$m-pinhole at 14 m distance, normalized with respect to $1\,\mathrm{mm}^2$, is plotted. Courtesy B. Kostka and A. Bernhard

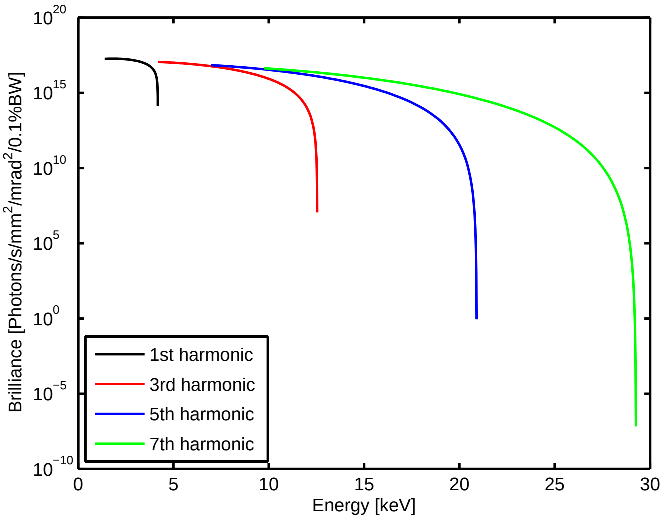

Fig. 2.11: Tuning curves of the SCU14 installed at ANKA: 100 periods, $\lambda_u = 14\,\mathrm{mm}$, $K_{max} = 2$). The curves were calculated with the software SPECTRA. Courtesy F. Burkart and A. Bernhard

a high flux makes undulators interesting for the use in synchrotrons. Their ability for self interference is the basis for Free Electron Lasers. In an undulator most of the photons are emitted into a small forward cone and interfere. The interference requires that the magnetic field amplitude must be uniform over the complete length. Deviations of this uniformity cause a broadening of the relative line width of the fundamental line and a suppression of the higher harmonics. This leads to a reduction in *brightness* ([Photons/s/mrad^2/0.1%BW]) and *brilliance* ([Photons/s/mm^2/mrad^2/0.1%BW]) of the emitted synchrotron radiation. Therefore deviations of the field amplitude have to be corrected [KSW91].

2.4 The phase error

A measure to describe the quality of the magnetic field of an undulator is the so-called phase error.
Relativistic electrons emit white light, when deflected. In an undulator, the electrons continuously emit white light into a narrow cone around the forward direction (z-axis). The maximum deflection angle Θ_w (see equation (2.9)) of the electrons is smaller than the opening angle of the cone ($\sim 1/\gamma$). Therefore the cones overlap and the photons emitted by a single electron interfere. The interference is constructive when the photon is in phase with the electron oscillation. This leads to the previously described line spectrum (see equation (2.10) and figure 2.9).
Disturbances of the uniformity of the magnetic field, like variations in the field amplitude $\tilde{B}$ or the period length λ_u from period to period, cause a change of the length of the electron trajectory. This yields a phase slip between electron and photon (see figure 2.12). A phase slip between the electron and the photon causes a line broadening and intensity reduction of the emitted lines because the constructive

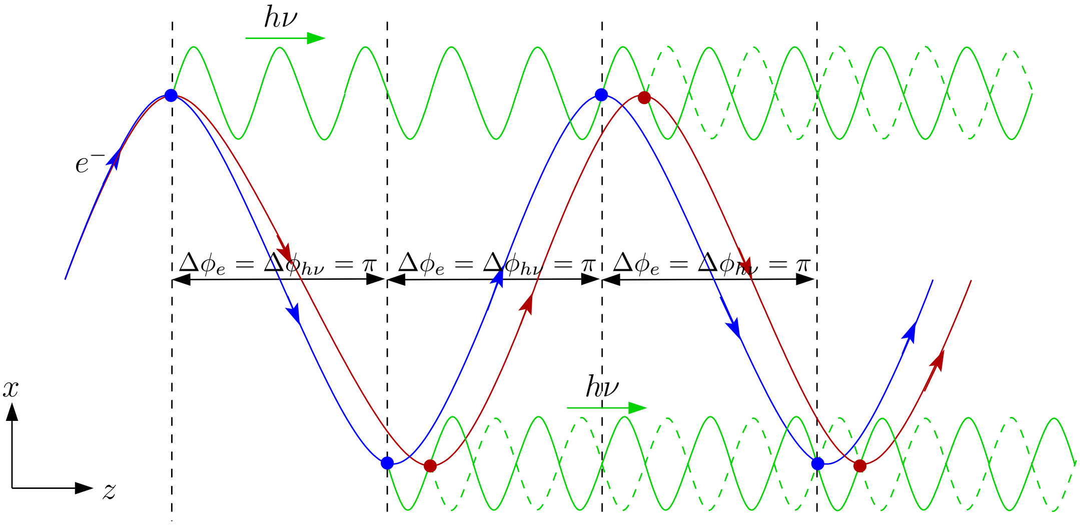

Fig. 2.12: Schematical drawing of the required correlation between the electron motion (blue) in the magnetic field of an undulator and the emitted light (green) with one wavelength to achieve constructive interference.

interference occurs at different wavelengths for different parts of the undulator. This is especially true for higher harmonics, which are more sensitive against a phase slip [OE03, Cla04b].

The phase difference between photon and electron for the half period i ($i = 1...2n$) of an undulator with n periods is [Wil]

$$\Phi_i = \frac{2\pi}{\lambda_u}\left(\frac{2(\frac{e}{m_e c})^2 J(z_i) - (z_i - z_0)K^2}{2 + K^2}\right), \tag{2.11}$$

(see Appendix A) with

$$J(z_i) = \int\limits_{z_0}^{z_i}\left(\int\limits_{z_0}^{z} B_y(z')dz'\right)^2 dz = \int\limits_{z_0}^{z_i}\left(I_1(z)\right)^2 dz.$$

The phase difference is important for the superposition of the radiation. $\tilde{\Phi}_i$ is therefore $\Phi_i \mod 2\pi$:

$$\tilde{\Phi}_i = \begin{cases} \Phi_i \mod 2\pi & \text{if } |\Phi_i \mod 2\pi| > \pi \\ 2\pi - |\Phi_i \mod 2\pi| & \text{if } |\Phi_i \mod 2\pi| \geq \pi \end{cases}. \text{ [Ber]} \tag{2.12}$$

The rms phase error of an undulator is calculated as the root mean square of all phase differences in the $2n$ undulator half periods

$$\Phi_{error} = \sqrt{\frac{\sum_{i=1}^{2n}(\tilde{\Phi}_i)^2}{2n}}. \tag{2.13}$$

A detailed derivation of the phase error from the equations of the electron motion in a magnetic field of an undulator is given in Appendix A. The phase differences at the ends of an undulator are in general disproportional large due to finite lenght effects. For that reason it is conventional to ignore the first and last two or three periods when calculating the rms phase error of an undulator [Cla04b].

3. MAGNETIC FIELD ERRORS CAUSED BY FINITE MECHANICAL TOLERANCES

In superconductive undulators field errors are mainly caused by finite mechanical tolerances. In addition possible error sources are variations in the quality of the pole material and persistent currents. Both are not considered in this thesis.

In a first step the possible mechanical deviations appearing in superconductive coils are described and their influence on the magnetic field is analyzed. In addition it is shown how deviations in the pole height and the wire bundle position act differently on the field and how they can be distinguished from each other.

3.1 Types of mechanical deviations

The principle layout of a superconductive undulator is shown in figure 3.1. It is made of two opposing superconductive coils. The structural basis of a superconductive coil is the coil body. It is made from iron or another magnetically soft material. One undulator period consists of two poles and two grooves. The body can be either made from a full block or assembled from disks. It is possible to use single pole and groove disks, but also half periods (pole and groove), full periods and even undulator parts of ten or more periods are imaginable.

The superconducting wire is wound around the coil body in such a way, that the current direction in neighbouring grooves is opposite. The superconducting wires usually have round or rectangularly shaped cross-sections. The latter eases the placement of the wires in the grooves. In the following all superconducting wires in one groove are called *wire bundle.*

The finite tolerances in the manufacturing of the coil body and the finite tolerances in positioning the wire bundle lead to field errors. A cut through a short superconductive coil along the undulator axis with exaggerated mechanical deviations is shown in figure 3.2. The distances of poles and wire bundles to the beam axis vary around a nominal value, which is defined by the gap width. In addition, the period length can vary.

The influences of the different mechanical deviations on the magnetic field for single pole and wire bundle errors are simulated with the program Radia [ECC97, CEC97]. The magnetic field of the inner 10 periods of a 30 period superconductive undulator with a period length $\lambda = 14\,\mathrm{mm}$, a gap width $g = 5\,\mathrm{mm}$ and a nominal field amplitude $\tilde{B}$=1.35 T was calculated.

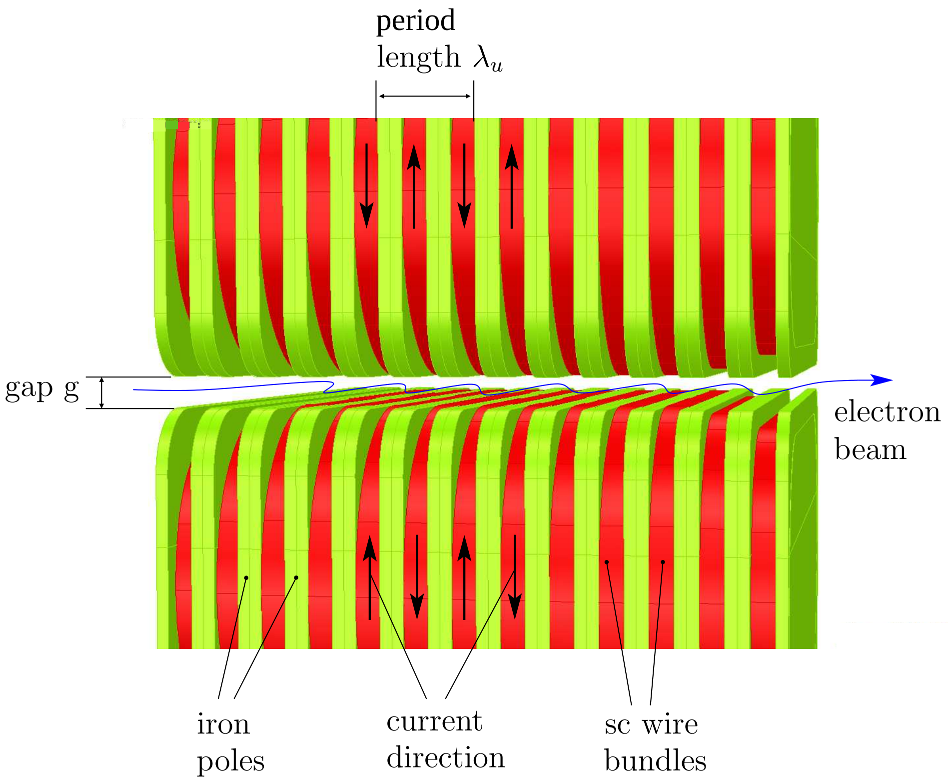

Fig. 3.1: Principle layout of a superconductive undulator, with iron poles and body (green) and superconductive wire bundles (red)

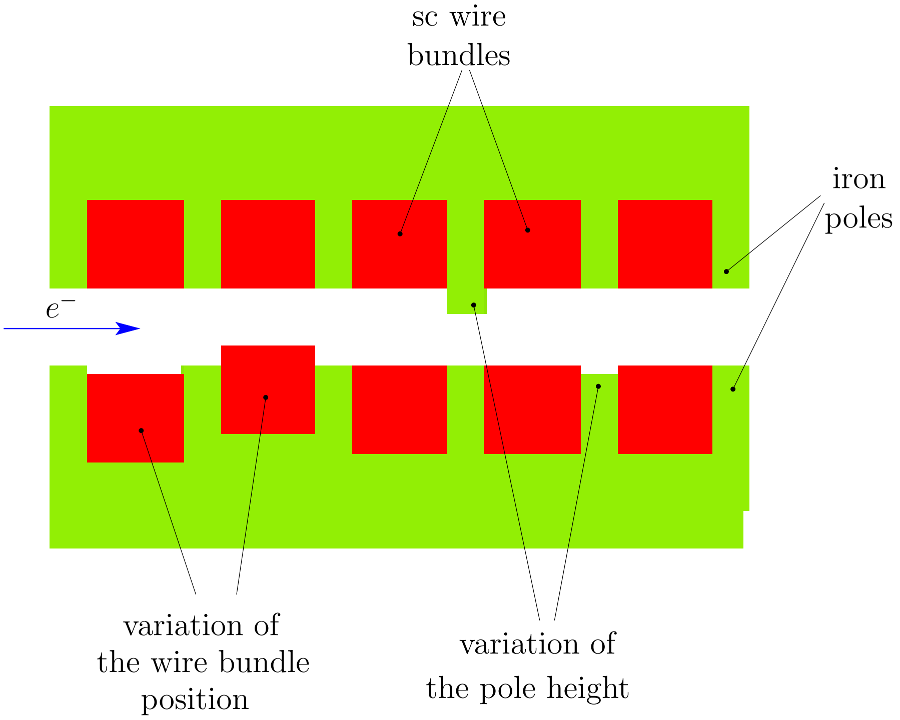

Fig. 3.2: Cut of a superconductive undulator with deviations of pole height and wire bundle position.

3.1.1 Variation of the pole position

The left plot of figure 3.3 shows the magnetic field along the beam axis (z) of an undulator with a significantly increased amplitude at the 5th minimum (red arrow). This is caused by a pole moved 500 μm closer to the beam axis . The plot on the right of figure 3.3 shows the difference field (red) between an ideal undulator field (black, dashed) and the disturbed field.

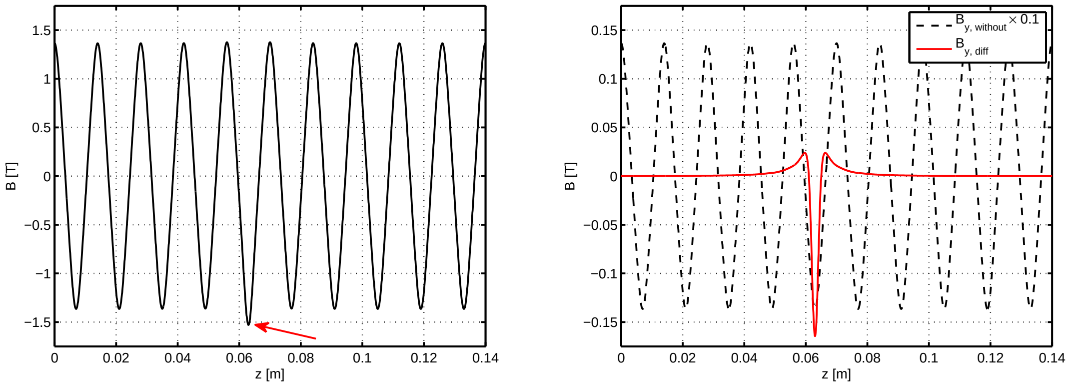

Fig. 3.3: Disturbed field (left) and difference field (right, red) between an ideal (black, dashed) and the disturbed field. The field deviation at the 5th minimum (red arrow) is caused by a pole, which is placed 500 μm closer to the beam axis.

The displacement of the pole causes the biggest disturbance at the 5th minimum and to a lower extend affects the field over a distance of 3.5 periods.

This field error changes the net electron trajectory (see left plot of figure 3.4). The net electron trajectory is averaged over the oscillatory motion of the electron.

Since the net electron trajectory changes its angle due to the field error the electrons experience a different effective period length before and after the misaligned pole. In addition the electron leaves the undulator under a different angle (dx/dz) and at a different x-position compared to the entrance of the undulator. I.e. the first and the second field integral of the undulator were changed by the displacement of the pole.

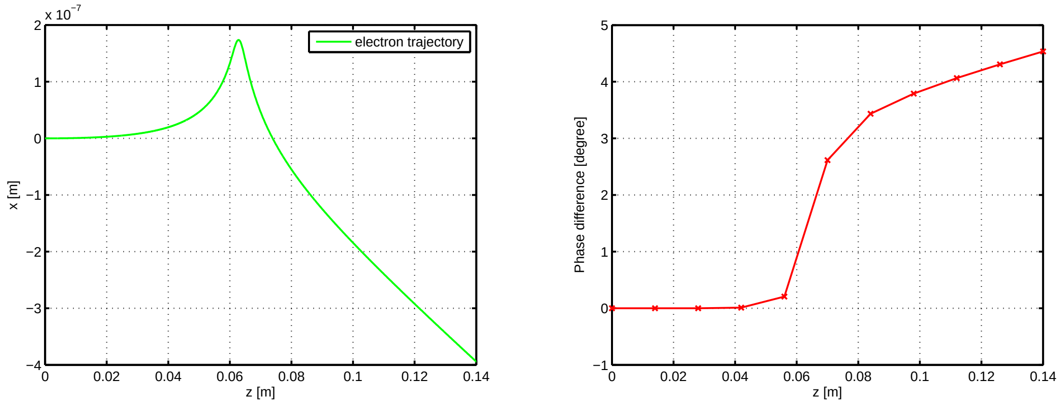

Fig. 3.4: Disturbance of the electron trajectory (left) and phase difference between electron and photon (right). Both are caused by the pole at the 5th minimum, which is moved 500 μm closer to the beam axis. The electron beam energy is 2.5 GeV.

The phase difference between electron and photon is shown in the right plot of figure 3.4. After passing the area with the disturbed field the phase difference increases linearly with z. Therefore, the undulator is divided into two parts and each part is radiating with a different wave-length.

3.1.2 Variation of the wire bundle position

The left plot in figure 3.5 shows the magnetic field along the beam axis (z) of an undulator with significantly increased absolute field values at the 5th minimum and 6th maximum (red arrows). These field deviations are caused by misplacing a wire bundle between the 5th minimum and the 6th maximum 500 μm closer to the beam axis. The plot on the right of figure 3.3 shows the difference field (red) between an ideal undulator field (black, dashed) and the disturbed field.

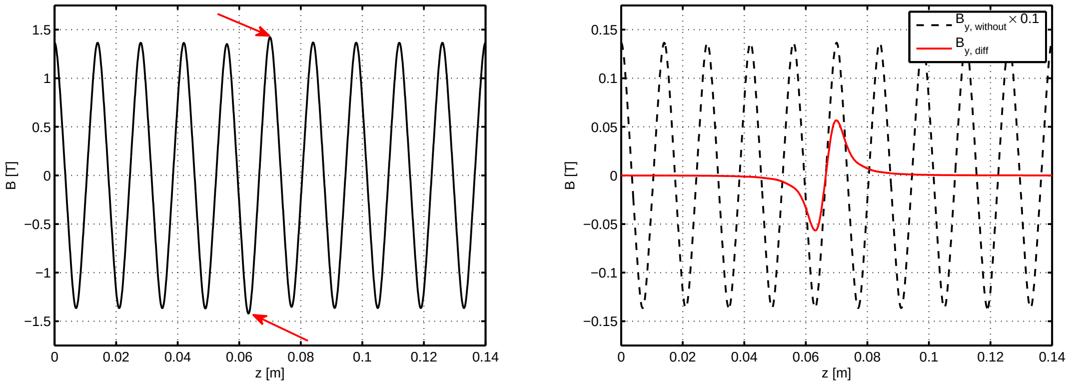

Fig. 3.5: Disturbed field (left) and difference field (right, red) between an ideal (black, dashed) and the disturbed field. The field deviations at the 5th minimum and the 6th maximum (red arrows) are caused by the wire bundle between these extrema, which is placed 500 μm closer the beam axis.

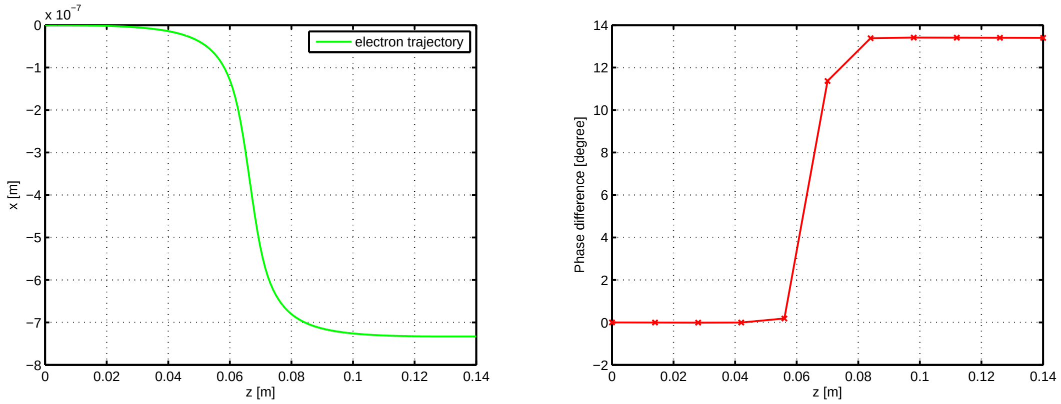

Fig. 3.6: Disturbed electron trajectory (left) and phase difference between electron and photon (right). The wire bundle between the 5th minimum and 6th maximum is misplaced 500 μm closer to the beam axis. The electron beam energy is 2.5 GeV.

The displacement of the wire bundle position causes an antisymmetric disturbance of the undulator field. The absolute value at the 5th minimum and the 6th maximum is equal. The zero crossing between the two extrema is not changed. The field disturbance covers about 3.5 undulator periods.
The disturbance of the net electron trajectory caused by the displacement of the wire bundle is shown in the left plot of figure 3.6 along the 10 periods of the undulator. The net electron trajectory is displaced in x direction but the angle of the trajectory remains the same. The period length experienced by the electron before and after the field disturbance is identical. The displacement of the wire bundle influences the second field integral only. The electron radiates with the same wavelength before and after the displaced wire bundle. The phase differences between electron and photon is shown in the right plot of figure 3.6. The undulator is divided into two parts by the displacement of the wire bundle and each part radiates with the same wave-length, but with a different phase.

3.1.3 Period length variation

Due to mechanical tolerances the period length of the superconductive coil can vary. The left plot of figure 3.7 shows the magnetic field of an undulator where the 9th half period (around the 5th maximum) is increased by 0.1 mm (red ellipse). The right plot of figure 3.7 shows the difference (red) between a disturbed and an ideal undulator field (black, dashed). The oscillation of the difference field is caused by the period length variation. The disturbance of the net electron trajectory is shown in the left plot of figure 3.8. The electron experiences the nominal period length before the period length variation and a longer period length afterwards. The electron leaves the undulator under a different angle (dx/dz) and at a different x-position. The first and the second field integral of the undulator are influenced.
The phase difference between electron and photon is shown in the right plot of figure 3.8. The undulator is divided by the period length variation into two parts and each part radiates with a different fundamental wave-length.

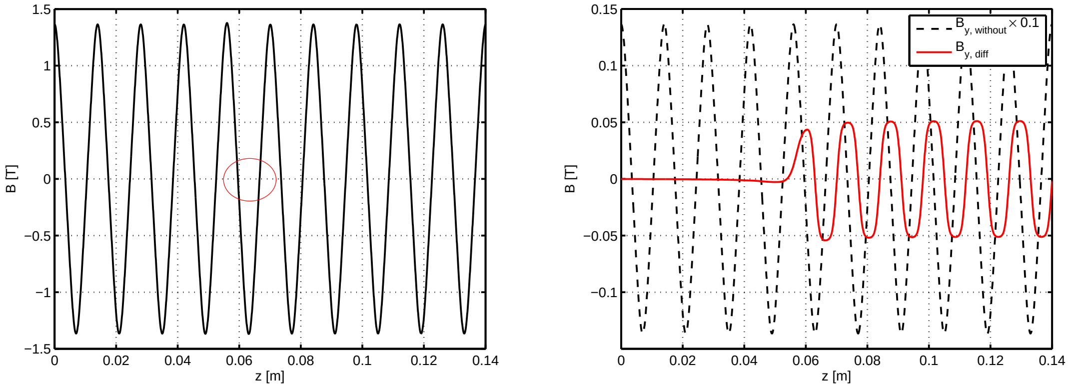

Fig. 3.7: Disturbed field (left) and difference field (right, red) between an ideal (black, dashed) and the disturbed field. The field deviation is caused by the increase of the distance between the 9th and the 10th zero crossing by 0.1 mm (red ellipse).

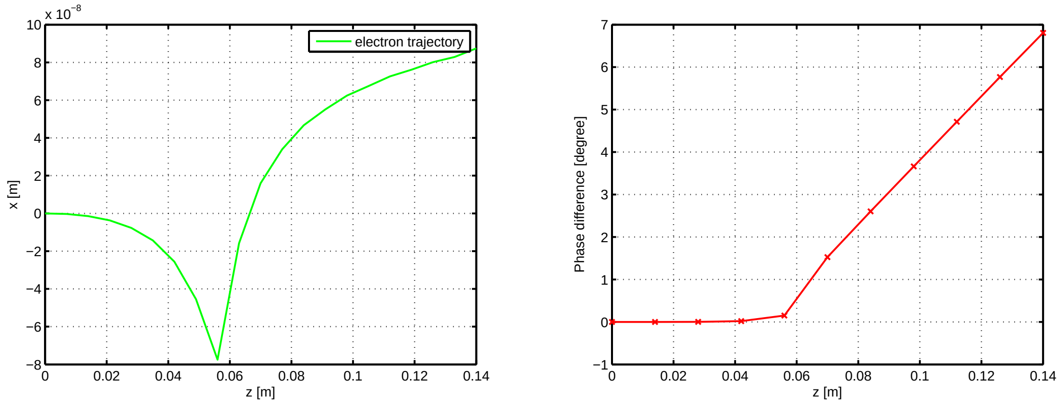

Fig. 3.8: Disturbed electron trajectory (left) and phase difference between electron and photon (right) caused by variation of the period length between the 5th minimum and 6th maximum by 100 μm. The electron beam energy is 2.5 GeV.

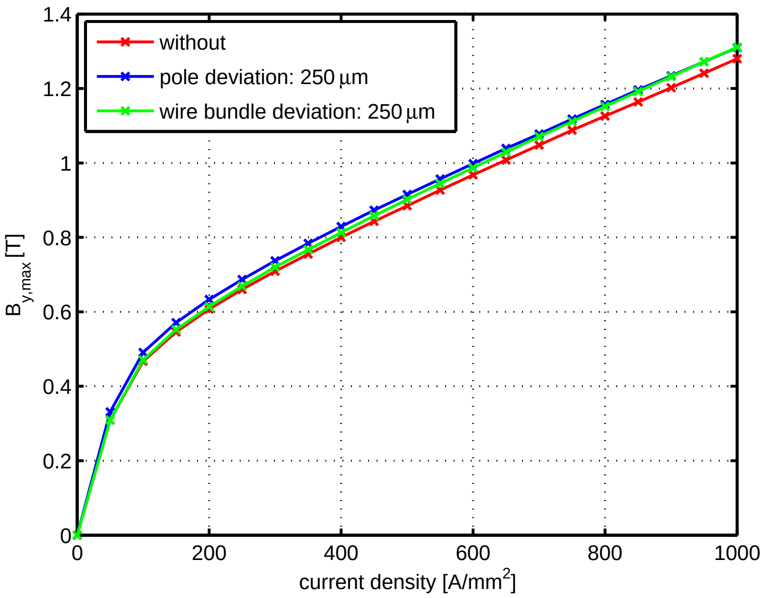

Fig. 3.9: Amplitude of the magnetic flux density versus current density for an ideal undulator (red), an undulator with a deviation of the pole position against the beam axis by 250 μm (blue) and an undulator with a deviation of the wire bundle position against the beam axis by 250 μm (green).

3.2 The influence of the undulator current on the different field errors

The different dependency of field errors on the current in the undulator coils caused by displacements of poles and wire bundles is presented in the following. This can be used to distinguish between the different mechanical deviations. The data were calculated with the finite element software OPERA-3D [VF]. The undulator model had a period length of $\lambda_u = 14$ mm and a gap width of $g = 5$ mm. The pole and the wire bundle positions were varied by 250 μm relative to the beam axis.
Figure 3.9 shows the field amplitudes of an ideal undulator (red), an undulator with a displacement of the pole (blue) and an undulator with a displacement of a wire bundle (green) plotted against the current density in the undulator coils. The strong change of the field amplitude at low current densities is caused by the magnetization of the iron poles scaling linearly with current. Above 350 A/mm^2 the iron is saturated and its contribution stays constant. Figure 3.10 shows the differences $\Delta B_{y,max}$ between the fields with mechanical deviations and the undisturbed field. The field deviations caused by displacement of a wire bundle (green) depend linearly on the current density. The difference field caused by the displacement of a pole (blue) can be divided into three parts: a linear dependency with a very steep slope between zero and 50 A/mm^2, a reduced slope between 50 A/mm^2 and 350 A/mm^2 and a constant field above 350 A/mm^2.

Due to the described behaviour a measured magnetic field of an undulator can be decomposed into pole components and wire bundle components if at least two field

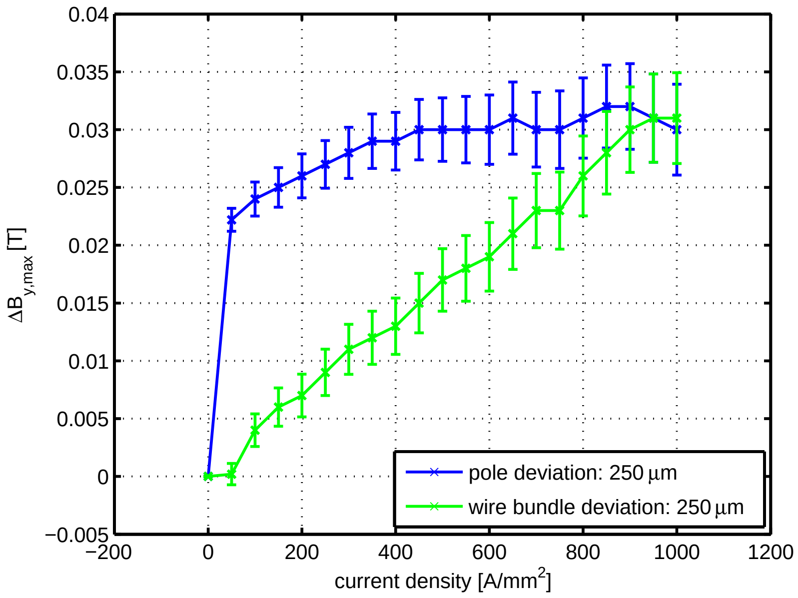

Fig. 3.10: Differences between ideal and disturbed fields for an undulator with a deviation of the pole position against the beam axis by 250 μm (blue) and an undulator with a deviation of the wire bundle position against the beam axis by 250 μm (green).

measurements with fully saturated iron poles, i.e. $j \geq 350\,\mathrm{A/mm^2}$, are available. With two measurements $B_{max}(I_1)$ and $B_{max}(I_2)$ at different currents I_1 and I_2 in the undulator main coils

$$B_{max}(I_1) = b_{wire} \cdot I_1 + B_{iron} \quad (3.1)$$

$$B_{max}(I_2) = b_{wire} \cdot I_2 + B_{iron} \quad (3.2)$$

the constant field part caused by the iron poles and the slope, which represents the wire bundle field, can be determinded as

$$b_{wire} = \frac{B_{max}(I_2) - B_{max}(I_1)}{I_2 - I_1}, \quad (3.3)$$

$$B_{iron} = B_{max}(I_2) - (b_{wire} \cdot I_2). \quad (3.4)$$

If more than two measurements are available for the decomposition, this can be done by linear regression.

Therefore the errors caused by a displacement of poles can be distinguished from the errors caused by a displacement of the wire bundles. This is essential for an effective local field error correction.

3.3 Decomposition of the measured SCU14 B-field

The previously described decomposition method has been applied to the B-field measurements of the superconductive undulator installed at ANKA (SCU14), which were performed by Accel Instruments GmbH, Bergisch Gladbach, Germany, before mounting the coils into the cryostat.

Figure 3.11 shows field amplitudes along the beam axis (z-axis) at a current density of 500 A/mm^2. The measurement shows that the field at the ends of the undulator is lower and that the field strength oscillates with a period length of 12.5 undulator periods.

From a previous detailed analyses it is know, that the first is caused by a bending of the coils - i.e. wire bundles and poles - while the vacuum vessel surrounding the coils was welded. The end of each coil is about 250 μm further away from the beam than the center. The second field deviation was caused by a mechanically uneven stamp with a length of 12.5 undulator periods which pressed the wire bundles into the grooves of the coil body [Wol05, WBC$^+$06, BKP$^+$].

Figure 3.12 shows the decomposition of the SCU14 field into its pole (left) and coil (right) components. It can be clearly seen, that both field components show the bending of the coils. This proves, that the coils are bent as a whole. The oscillation can be clearly identified in the wire bundle component, but cannot be found in the pole component of the field. Thus, the oscillations in the measured field are caused by mechanical displacements of the wire bundles but not by displacements of the poles.

Besides the bending the analysis shows two additional major mechanical deviations in the position of the poles against the beam axis.

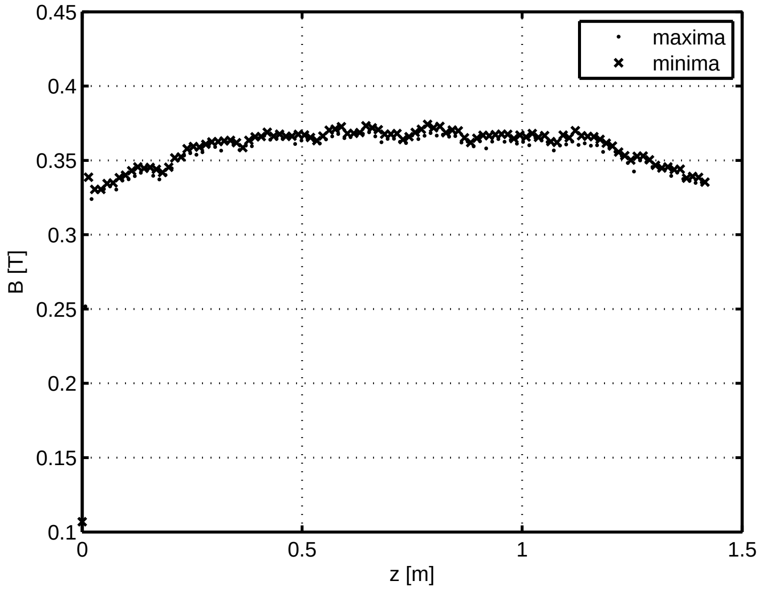

Fig. 3.11: Absolute values of the maxima and minima of the SCU14 field measured along the beam axis. [BKP$^+$]

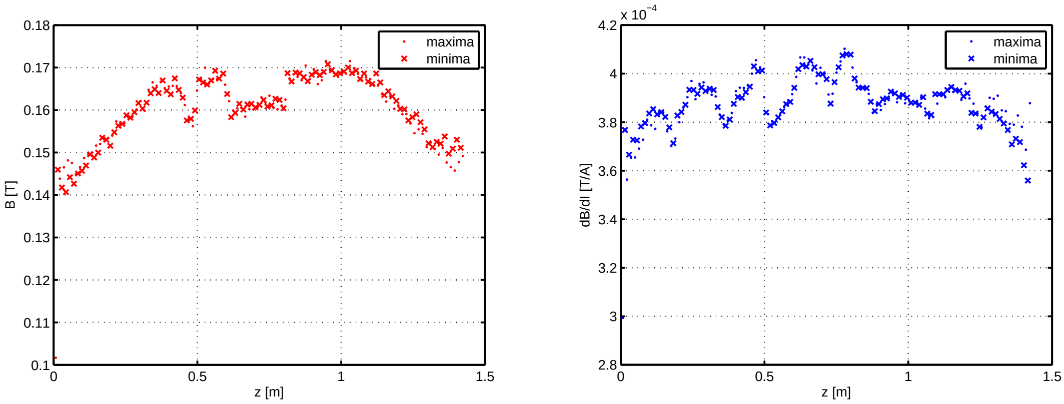

Fig. 3.12: Absolute values of the maxima and minima of the pole (left) and wire bundle (right) component of the SCU14 field. [BKP$^+$]

4. PHASE ERROR AND MECHANICAL TOLERANCES

The phase error is the most important measure for the quality of the magnetic field of an undulator.

In the previous chapter it was shown how mechanical deviations influence the field and the electron trajectory. In this chapter the relation between mechanical tolerances and the phase error is investigated.

4.1 Sine wave model

In the following the undulator field is modelled by sine half waves with individual amplitude and period length. The modelled field is continuous but other than at a real undulator the field is not differentiable at the zero crossing.

The field parameters, which are the design parameters of the SCU15 presently under construction, are given in table 4.1.

The relative variation of the amplitude caused by the displacement of a pole or a wire bundle were calculated with an Opera-3D [VF] model of the SCU15. The parameters used in this model are given in table 4.2.

Figure 4.1 shows the relative change of the field amplitude $\frac{\Delta B}{B}$ caused by an absolute variation of the pole Δ_{pole} position relative to the beam axis. The numerical uncertainty is in the range of 2.5 % with the used simulation model. The relative field error can be fitted by the linear function

$$\frac{\Delta B}{B} = \frac{77.3}{\mathrm{m}} \cdot \Delta_{pole} \tag{4.1}$$

(see figure 4.1).

Figure 4.2 shows the relative change of the field amplitudes $\frac{\Delta B}{B}$ at the neighbouring poles caused by an absolute variation of the wire bundle position against the beam axis. The relative field changes at the neighbouring poles behave both linearly, but with slightly different slopes. The numerical errors were again in the

period length	$\lambda_u = 15\,\mathrm{mm}$
gap width	$g = 8\,\mathrm{mm}$
field amplitude	$\tilde{B}_0 = 0.804\,\mathrm{T}$
number of periods	$N = 100$

Tab. 4.1: Design parameters for the magnetic field of the SCU15 presently under construction.

pole width	3.68 mm
groove width	3.82 mm
groove depth	4.43 mm
gap width	$g = 8\,\mathrm{mm}$
current density	$1000\,\mathrm{A/mm^2}$
field amplitude	$\tilde{B}_0 = 0.804T$
pole material (BH-curve)	Vacoflux50 [Vac01] (see appendix)

Tab. 4.2: Parameters used in the Opera-3D model for the SCU15.

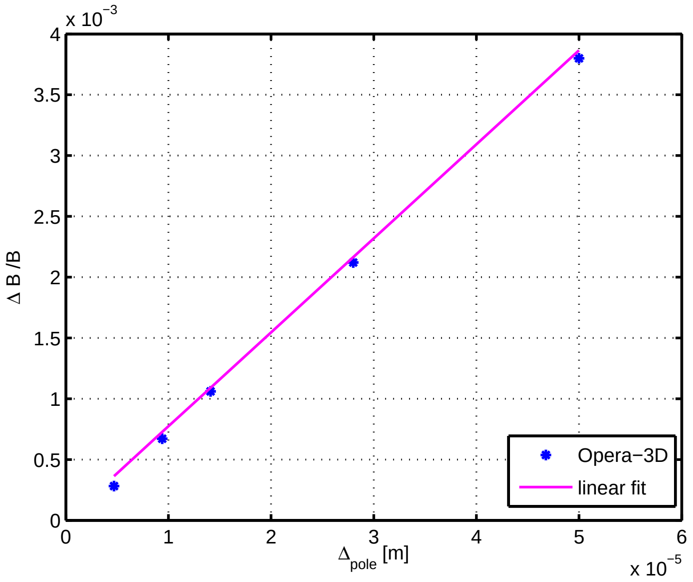

Fig. 4.1: Relative field change caused by a variation of the pole position against the beam axis. Blue dots: Opera-3D [VF] simulation; Magenta line: linear fit equation (4.1).

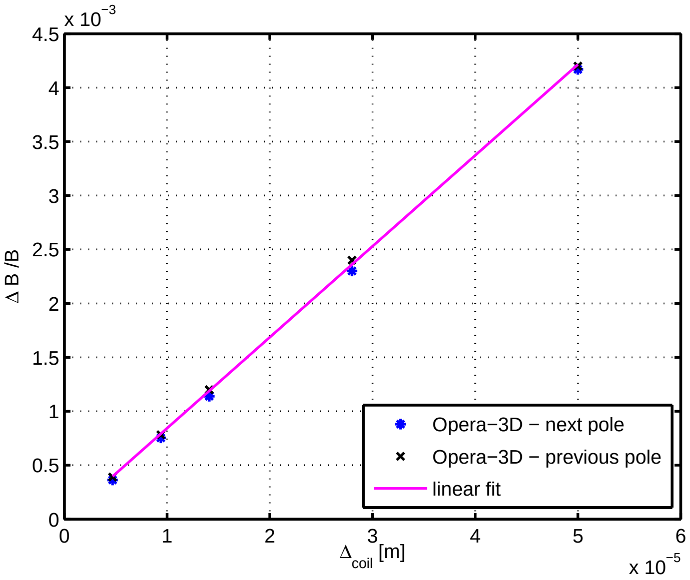

Fig. 4.2: Relative field change caused by a variation of the wire bundle position against the beam axis. Blue dots: Opera-3D [VF] simulation; Magenta line: linear fit equation (4.2).

range of 2.5 %. For the linear model the steeper slope was chosen:

$$\frac{\Delta B}{B} = \frac{84.3}{\mathrm{m}} \cdot \Delta_{coil}. \tag{4.2}$$

4.2 Statistically distributed deviations (Monte-Carlo)

To quantify the effects of the different mechanical deviations on the phase error Monte-Carlo simulations with statistically distributed mechanical errors have been performed. In the present ANKA undulator design the mechanical tolerances for the construction of the undulator coils are 10 μm. For the following simulations it was assumed that 10 μm correspond to 3σ in a Gaussian distribution. This means, that 99.7 % of all deviations are below 10 μm.
The standard deviations for the pole and the wire bundles therefore are

$$\sigma_{pole} = \sigma_{coil} = \sqrt{2 \cdot \left(\frac{10\,\mu\mathrm{m}}{3}\right)^2} = 4.71\,\mu\mathrm{m}, \tag{4.3}$$

assuming that the deviations occurring in both coils add up statistically. The standard deviation of the length variation of a half period was defined as

$$\sigma_{\lambda/2} = \sqrt{2 \cdot \left(\frac{10\,\mu\mathrm{m}}{3}\right)^2} = 4.71\,\mu\mathrm{m}, \tag{4.4}$$

since each half period consists of one pole and one groove both with $\sigma = \frac{10}{3}\,\mu$m.

Monte-Carlo simulations have been performed for each type of the mechanical deviations to quantify the influence on the phase error. In addition a Monte-Carlo simulation with all three mechanical deviations present has been performed. Each Monte-Carlo simulation consisted of 1000 undulators with 100 periods.

The phase error distribution for 1000 undulators with normally distributed variations of the pole positions is shown in the left plot of figure 4.3. The right plot of figure 4.3 shows the phase error distribution caused by normal variations of the wire bundle positions. The bins of the histograms have a width of 0.1°.

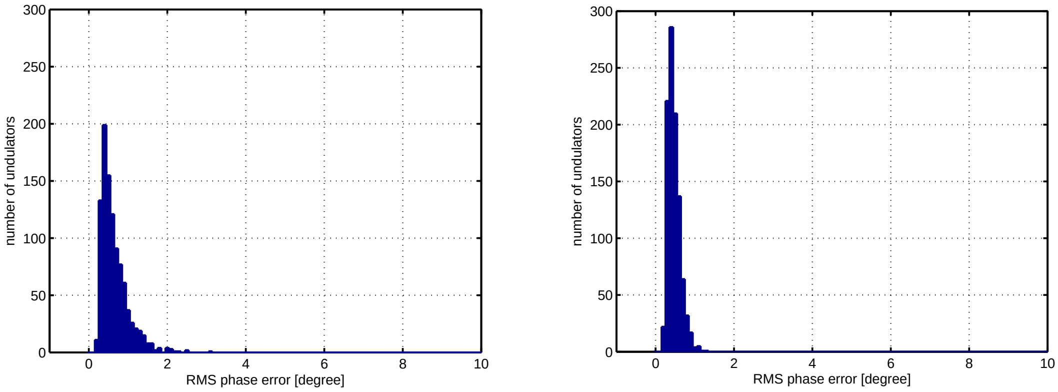

Fig. 4.3: Phase error distribution for 1000 undulators with normally distributed variations of the pole (left) or wire bundle (right) positions against the beam axis ($\sigma_{pole} = \sigma_{coil} = 4.71\,\mu$m).

The confidence levels of the different phase error distributions are compared in table 4.3. The peak of the phase error distribution caused by the variation of the wire bundle positions is sharper and the tail shorter compared to the distribution caused by the pole position variation. Therefore, the variation of the pole positions against the beam axis increases the phase error more than the variation of the wire bundle positions. This behaviour is due to the smaller phase difference caused by the antisymmetric field error generated by a variation of a wire bundle compared to the variation of the pole position (see chapter 3).

The left plot of figure 4.4 shows the phase error distribution for 1000 undulators with normally distributed variations of the half period lengths. The right plot of figure 4.4 shows the phase error distribution of 1000 undulators with variations in pole, wire bundle and period length. The standard deviations for each variation are the same as before. The bins of the histograms have a width of 0.1°.

The comparison of the confidence levels for the different cases is shown in table 4.3. It can clearly be seen, that the variation of the period length has the biggest impact on the phase error. This variation also dominates the phase error distribution caused by the combination of all three mechanical variations. As stated above the impact of the pole position variation influences the phase error more than the variation of the wire bundle position.

To reduce phase errors due to mechanical deviations it is therefore important to fabricate the coil body with high accuracy. The period length and pole position

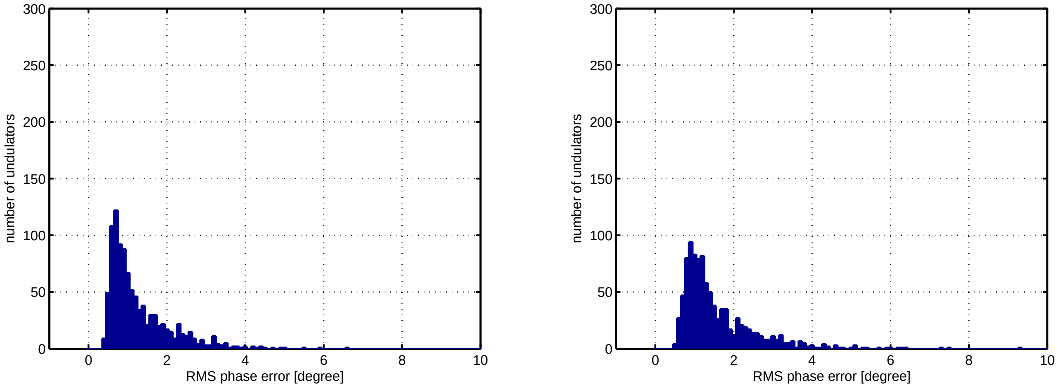

Fig. 4.4: Phase error distribution for 1000 undulators with normally distributed length variations of the half periods (left) and phase error distribution for 1000 undulators with normally distributed variations of the pole and wire bundle positions and the half period lengths (right) ($\sigma_{pole} = \sigma_{coil} = \sigma_{\lambda/2} = 4.71\,\mu$m).

confidence levels	pole position	wire bundle position	half period length	combination of all three variations
peak	0.4°	0.4°	0.7°	0.9°
50 %-level	0.55°	0.44°	1.0°	1.25°
99.7 %-level	2.3°	1.1°	5.0°	6.4°

Tab. 4.3: Confidence levels of the phase error distributions for 1000 undulators with normally distributed variations of the pole, wire bundle positions and length variations of the half periods ($\sigma_{pole} = \sigma_{coil} = \sigma_{\lambda/2} = 4.71\,\mu$m). The results for only one type of mechanical tolerances are compared with the combination of all three variations.

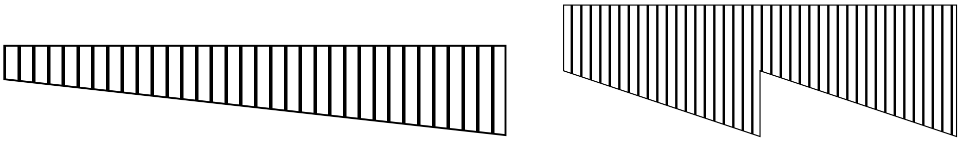

Fig. 4.5: Sketch of a linear (left) and a sawtooth deformation (right) of the poles. [PWBF08]

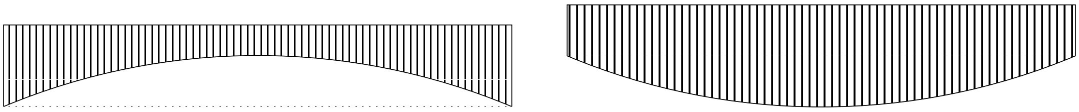

Fig. 4.6: Sketch of two possible parabolic deformations of the pole positions - concave (left) and convex (right). [PWBF08]

variations of the body have to be measured and corrected if necessary before winding.

4.3 Systematic variations

The magnetic field of the SCU14 installed at ANKA suffers from systematic errors (see figure 3.11). As discussed in chapter 3.3 these are caused by the bending of both coils and by a sinusoidal displacement of the wire bundles.

In the following the resulting phase error for linear, sawtooth, parabolic, sinusoidal and rectangular shaped deformations are discussed. The maximum deformations from the ideal form are in all cases $10\,\mu$m.

A linear deformation of the pole height is sketched in the left plot of figure 4.5. The deviation from the nominal pole position left ($\Delta_{pole} = -5\,\mu$m) to the right ($\Delta_{pole} = +5\,\mu$m) is $10\,\mu$m. In a similar way linear variations can be defined for the wire bundles and the period length.

A sawtooth shape deformation is shown in the right sketch of figure 4.5. The phase error was calculated for variations with two saw teeth.

Parabolic deformations of the pole positions are sketched in figure 4.6. The parabolic deformation of the wire bundle positions and the period lengths were also considered.

Sinusoidal deformations of the pole positions against the beam axis are sketched in figure 4.7. The amplitude of the deformation is $5\,\mu$m. The period length λ_{sin} was chosen in units of the undulator length l_{und}. The phase errors were calculated for $\lambda_{sin} = l_{und}$, $\lambda_{sin} = \frac{2}{3}l_{und}$ and $\lambda_{sin} = \frac{1}{2}l_{und}$. The sinusoidal deformations were also applied to the wire bundle positions and the period lengths.

Two possibilities of rectangular deformations of the pole positions are sketched in

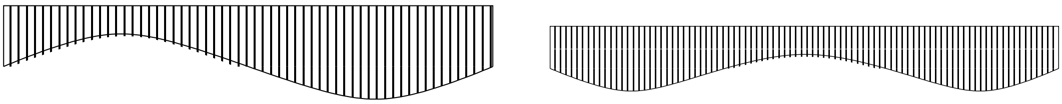

Fig. 4.7: Sketch of sinusoidal deformations of the pole positions - $\lambda_{sin} = l_{und}$ (left) and $\lambda_{sin} = \frac{2}{3}l_{und}$ (right). [PWBF08]

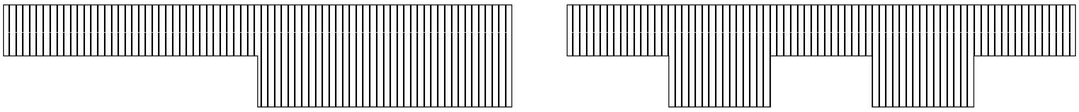

Fig. 4.8: Sketch of two rectangular shaped deformations of the pole positions: single step (left) and four steps (right). [PWBF08]

type of deformation	pole position	wire bundle position	half period length	pole and wire bundle
linear	2.6°	3.7°	4.2°	5.0°
sawtooth (2)	1.2°	1.8°	2.1°	2.5°
parabolic	1.8°	2.8°	3.2°	3.9°
sinusoidal ($\lambda_{sin} = l_{und}$)	3.1°	4.5°	5.1°	6.2°
sinusoidal ($\lambda_{sin} = \frac{2}{3} l_{und}$)	1.9°	2.8°	3.3°	4.0°
sinusoidal ($\lambda_{sin} = \frac{1}{2} l_{und}$)	1.5°	2.2°	2.6°	3.1°
rectangular (1 step)	4.1°	6.2°	7.1°	8.6°
rectangular (4 steps)	2.8°	4.0°	4.9°	6.0°

Tab. 4.4: Comparison of phase errors caused by systematic deformations of the pole and wire bundle positions and the period length. The maximal deviation from the nominal values was $10\,\mu$m. [PWBF08]

figure 4.8. The steps have a height of $10\,\mu$m. The phase errors were calculated for one and four steps. Rectangularly shaped deformations of the wire bundle position and the period length were also considered.
The results of the phase error calculations are summarized in table 4.4

The comparison of the phase errors caused by different systematic deformations shows that a single step in the center of the undulator causes the biggest phase errors. This error type divides the undulator into two undulators with different $K-$values. Each part emits light with a different fundamental wavelength. The second biggest phase error is caused by sinusoidal variations with a period-length close to the length of the undulator. Shorter or longer period-lengths lead to smaller phase errors.

From table 4.4 it can be concluded, that it is important to avoid step functions and periodic deformations with a period length in the range of the undulator length. The shorter the correlation length of the deformations the smaller is the phase error. For systematic errors the effects of neighbouring wire bundles on the extremum add up. For statistically distributed deviations there is a high probability that the effects of neighbouring wire bundles cancel. Therefore, systematic errors of the wire bundle positions dominate the phase error. This is an important difference to statistically distributed mechanical deviations where the period length variations dominate the phase error.

5. CLASSICAL SHIMMING METHODS FOR SUPERCONDUCTIVE UNDULATORS

The field quality is a major issue for using superconductive undulators in current 3rd and future 4th generation synchrotron light sources, like Free electron Lasers (FEL) or Energy Recovering Linacs (ERL). To obtain phase errors of $\approx 1^{\circ}$ the field errors have to be corrected or shimmed. The up to now known shimming methods for superconductive undulators are: mechanical shimming, shimming with integral correctors and active shimming with separately powered local correction coils. Correction coils in superconductive undulators have to be also superconductive. Otherwise they would warm up the cold mass of the undulator. Therefore in the following all active correction coils for superconductive undulators are considered to be superconductive wires or loops.

In the following the different classical shimming methods are presented. Their advantages, disadvantages and limitations are discussed.

5.1 Mechanical shimming methods

In general the magnetic field is optimized in permanent magnet undulators by attaching thin ferromagnetic slices - the so-called shims - to the beam-sided surface of the magnet arrays. This method is not applicable in superconductive undulators.

Mechanical shimming methods are also well known from permanent magnet undulators. The position of poles and permanent magnets are adjusted very accurately with screws to correct misalignment and reduce field errors. The concept for mechanical shimming of the undulator systems of the European XFEL at DESY, Hamburg, is shown in figure 5.1. The poles of these undulators can be adjusted with four screws in height and tilt angle [PLT99, Pfl05].

This mechanical shimming concept can only be used for the coil body before winding, but not for the complete superconductive undulators with the current design described in chapter 3.

From the mechanical measurements of the pole height, the groove depth and the period length the expected phase error can be calculated as described in chapter 4. If the expected phase error is too high the body of the undulator has to be modified mechanically.

The whole procedure has to be repeated until the calculated phase error caused by the mechanical deviations is well below the required phase error or the mechanical deviations are below the tolerances achievable with the mechanical methods. The advantage of mechanical shimming is that it is done at room temperature. The disadvantage is that it has to be done before winding, thus, field errors caused by

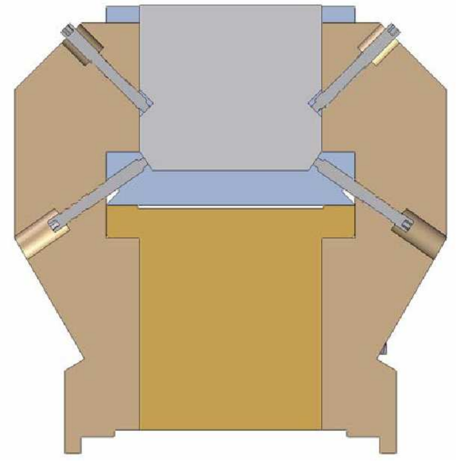

Fig. 5.1: The cross section of a permanent magnet undulator shows the mechanical shimming concept for the undulator systems of the European XFEL at DESY, Hamburg. The pole (grey-blue) of the undulator can be adjusted with four screws (dark-gray-blue) in height (±0.3 mm) and tilt angle (±0.1 mrad) [PLT99, Pfl05].

misplacements of wire bundles cannot be corrected with this method.

5.2 Shimming with integral correctors

Integral correctors are used primarily to compensate the first and the second field integrals in undulators. In general, these integral correctors are two dipoles, one at the beginning and one at the end of the undulator. Additional dipole magnets along the undulator can be used to optimize the trajectory of the electrons in the undulator with respect to the phase error.

The SCU14 is equipped with five corrector dipole magnets. Two dipole magnets are positioned before and after the main coils - the so-called steerers - and three integral correctors along the undulator, each covering one third of the undulator length. The positions of the these dipole magnets relative to the center of the SCU14 and their length are shown in table 5.1 and sketched in figure 5.2. First the two steerers are used to compensate the first and the second field integral. The three integral correctors give three additional degrees of freedom, which are used to optimize the trajectory. For optimization a multi-dimensional simplex algorithm was used [BKP$^+$].

The simulations were performed in three steps: 1.) correction of the first and second field integral using only the two steerer magnets, 2.) integral correction for the whole field and trajectory optimization for the inner 95 periods using all five dipole magnets, 3.) integral correction for the whole field and trajectory optimization for the inner 50 periods using all five dipole magnets.

Figure 5.3 shows the magnetic field of the SCU14 at 900 A undulator current. Steerer 1 and 2 were powered to correct the first and second field integrals to zero. As already reported in chapter 3 the field of the undulator is bent and shows a sinusoidal amplitude variation with a period length of 12.5 undulator periods. The

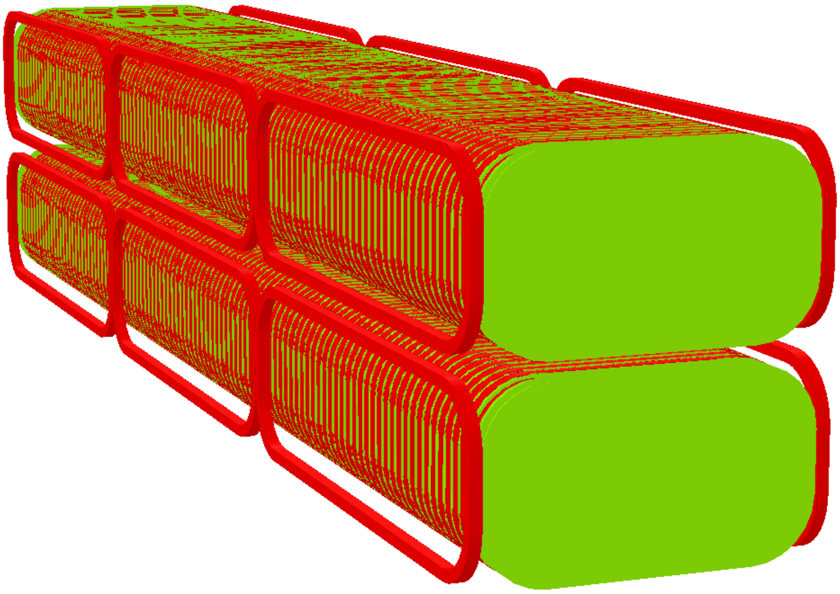

Fig. 5.2: Sketch of the integral correctors placed in the SCU14. The steerer magnets are not shown. [BKP+]

Corrector magnet	center of magnet [mm]	length of magnet [mm]
steerer 1	-826	78
steerer 2	+826	78
integr. corr 1	-488	442
integr. corr 2	0	442
integr. corr 3	+488	442

Tab. 5.1: Position (z-axis) of the centers of the corrector magnets relative to the center of the SCU14 and their length. [BKP+]

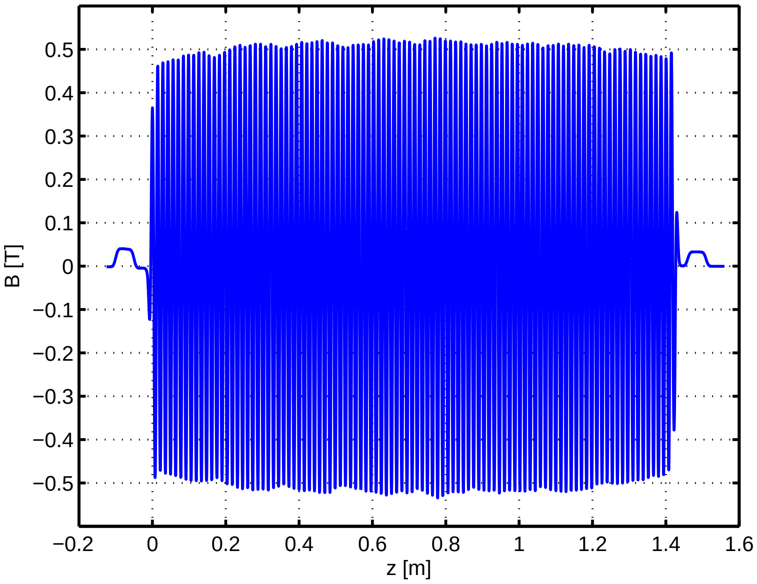

Fig. 5.3: Magnetic field of the SCU14 at 900 A in the main coils and steerer 1 and 2 powered to correct the first and second field integral to zero. [BKP+]

inner 95 periods have, without trajectory optimization, a phase error of 108.9° (see table 5.2).

The left plot of figure 5.4 shows a comparison of the first field integral before and after the optimization of the trajectory with respect to the phase error for the inner 95 periods. It can be seen, that the first field integral is significantly flattened by integral shimming.

The comparison of the second field integral, which is proportional to the trajectory of the electrons, for the inner 95 periods is shown in the right plot of figure 5.4. The maximum deflection of the electrons from an ideal straight path is reduced to 20 % of the uncorrected value before. Table 5.2 shows the comparison of the phase errors with and without trajectory optimization for the inner 95 and 50 periods. The fields of the correction dipoles are listed in table 5.3. The achievable reduction of the phase error is significant.

The efficiency in phase error reduction for integral shimming depends strongly on the distribution and the type of field errors. The results for the SCU14 cannot be generalized.

Nevertheless, shimming with integral correctors is very effective when systematic field deviations are present and is less effective with statistically distributed field errors.

5.3 Active shimming with local correction coils

Shimming with local correction coils was proposed some years ago [CRS+03] and successfully tested with a short mock-up coil at Lawrence Berkeley National Labo-

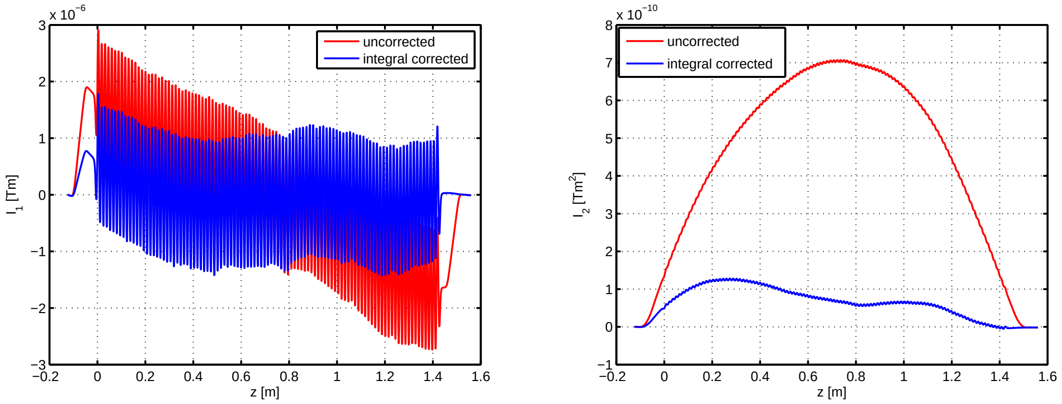

Fig. 5.4: Comparison of the first (left) and second field integral (right) of the SCU14 at 900 A before and after the optimization of the trajectory in respect to the phase error for the inner 95 periods with the three additional integral corrector dipoles. [BKP+]

number of included inner periods	phase error uncorrected	phase error corrected
95	108.9°	11.96°
50	109.7°	4.8°

Tab. 5.2: Comparison of phase errors before and after correction with the three integral correctors. The phase errors have been calculated for the inner 95, 75 and 50 periods. [BKP+]

Corrector magnet	95 inner periods	50 inner periods
steerer 1	1.08 mT	13.5 mT
steerer 2	−10.1 mT	2.34 mT
integr. corr 1	1.58 mT	0.01 mT
integr. corr 2	0.97 mT	1.46 mT
integr. corr 3	2.48 mT	0.97 mT

Tab. 5.3: Fields in the corrector magnets for different phase error optimizations (including the inner 95 and 50 periods). [BKP+]

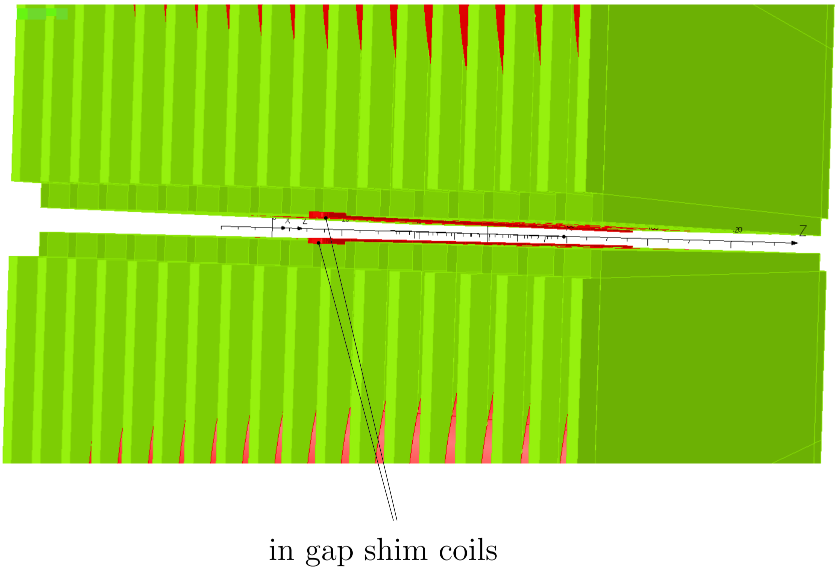

Fig. 5.5: Opera-3D [VF] model of a superconductive undulator with additional in gap shim coils.

ratory in California, US [PDB+05].
However, distributed local shimming requires additional current feed-throughs and power supplies. These feed-throughs, depending on their number and size, can be a major source for heat transfer into the cold mass. To avoid a massive increase of the cost for the cryostat and cooling, the number of feed-throughs has to be limited. For instance the SCU15, now under construction, has four independently powered correction coils with a maximal correction current of $5 - 10\,\mathrm{A}$. The maximum field error to be corrected is not bigger than $1\,\%$ of the maximum field amplitude of $\tilde{B} \approx 1.3\,\mathrm{T}$ at a nominal gap of $g = 5\,\mathrm{mm}$.
In the following, the different possible positions of the correction coils will be discussed.

5.3.1 Active in gap shim coils

The most obvious position for correction coils is in the gap of the undulator. The correction coils are placed on top of the superconductive wire bundles of the main coil (see figures 5.5 and 5.6). The current direction in the opposing shim coils is identical.

Simulations have been performed with the finite element code Opera-3D from Vectorfields, UK [VF]. The shim coils are assumed to have a cross-section of $1\,\mathrm{mm}^2$ and to be powered with a current of $I_{corr} = 1000\,\mathrm{A}$. The nominal gap width is $g = 5\,\mathrm{mm}$. In a first step it is assumed that the shimming coils are treated as air-core coils. This is true when the iron poles at the shim coils are fully saturated. In a second step the action of the shim coils was simulated without current in the main coil, i.e. the iron body of the undulator is fully unsaturated.

The results are plotted in figure 5.7. It can be seen clearly, that the air-core shimming coils produce a localized correction field. The main peak has an ampli-

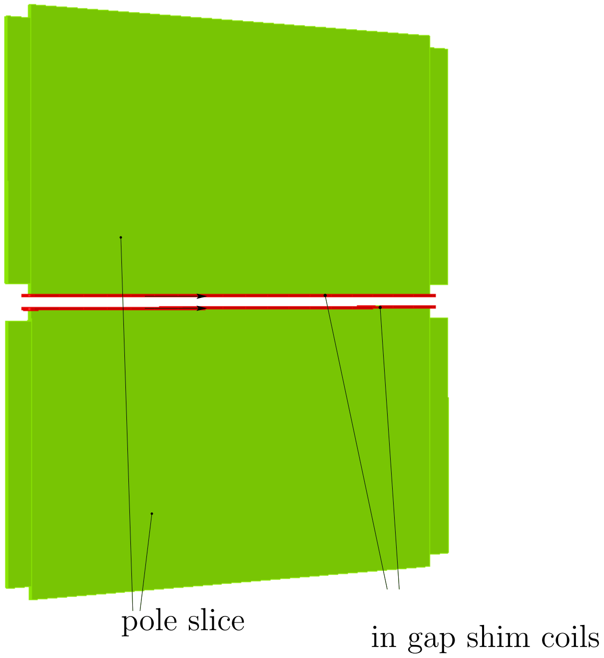

Fig. 5.6: Pole slice of a superconductive undulator with in gap shim coils. The current in the opposing shim coils has the same direction (see arrows).

tude of 0.1 T, i.e. 0.1 mT per ampere turn. The side peaks have an amplitude of about 14 % of the main peak.

The correction field in case of a completely unsaturated coil body shows a higher and broader main peak. The shimming coils magnetize mainly the local and the neighbouring poles. In addition they also magnetize the rest of the undulator slightly. The field amplitude caused at the other poles is approximatly 4 % of the main correction peak. The broader correction peak has to be considered, for corrections at low fields. The field changes along the rest of the undulator can be neglected. In order to reduce the number of feed-throughs and independent power supplies, the shim coils have to be connected in series. The correction field is then determined by the number of windings around each pole. Due to different current dependencies of pole and wire bundle deviations, two different correction circuits are needed.

A slightly different idea was discussed in the author's master thesis using four different wires and four power supplies [Wol05].

In-gap shimming coils are a very effective way to correct field deviations. The correction currents are relatively small and the unwanted magnetization of the whole coil body caused by the shim currents is negligable even in case of completely unsaturated poles. The position in the gap has also one major disadvantage: due to the finite dimensions of the correction coils, the magnetic gap has to be either increased, which leads to a reduction of the on axis field, or the beam stay clear is reduced, which reduces the life time of the electron beam in the storage ring. Both negative effects have to be minimized by using thin wires and high current densities.

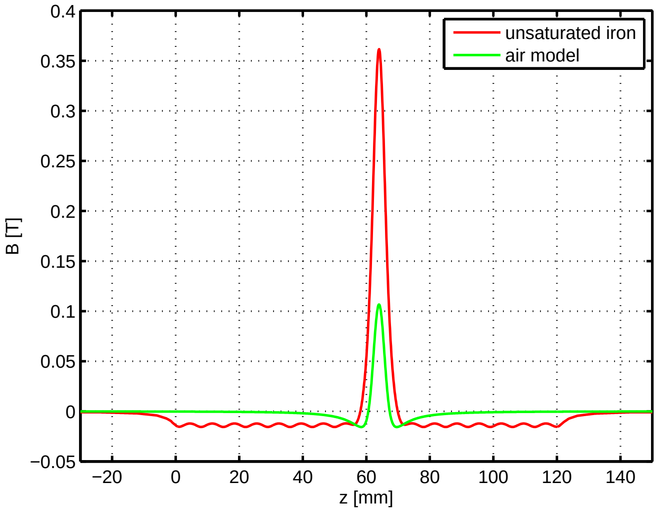

Fig. 5.7: Correction fields caused by air-core in gap shimming coils and in gap shimming coils mounted on completely unsaturated coil bodies (no current in the main coils).The cross-section of the shimming coils is 1 mm^2 and the correction current is $I_{corr} = 1000$ A.

5.3.2 Active in iron shim coils

In order to keep the gap untouched an attempt was made to place the correction coils inside the iron body of the coil. Figure 5.8 shows an x-y-cut of the undulator body. The shim coils have a cross-section of 1.5 mm^2 and are powered with a current of $I_{corr} = 1000$ A. The nominal gap width is $g = 5$ mm.

As before, the simulations have been performed in two steps: firstly with air-core shimming coils and secondly with a fully unsaturated iron body. The results are shown in figure 5.9. The air-core shimming coils produce a localized correction field with an amplitude of 5.5 mT. With a fully unsaturated coil body the shimming coil magnetizes all poles of the undulator. The field increase at the position of the correction coil is small.

It needs to be stated that the biggest part of the coil body stays unmagnetized for all currents in the undulator main coils due to the bifilar winding technique. This system can only work efficiently when the correction coils are close to the undulator surface. However, the mechanical stability of the undulator body against the large magnetic forces acting on the poles might suffer from this. Therefore, shimming with in iron coils is problematic.

5.3.3 Active lateral shim coils

Lateral shim coils positioned at the sides of the pole discs also avoid an increase of the magnetic gap. Each lateral shim-coil consists of four individual coils. Figure 5.10 shows the position and the current direction of the lateral coils. Two are shown in the figure, the other two are placed on the other side of the coil body. They have opposite current directions.

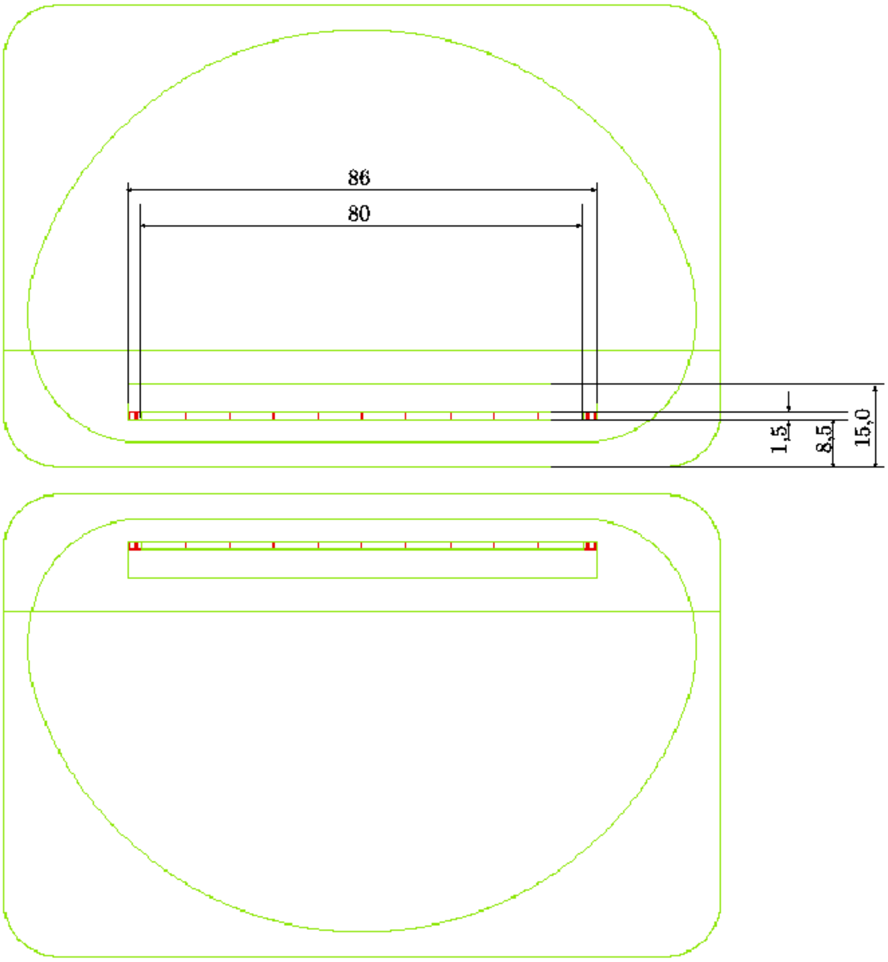

Fig. 5.8: X-Y-Cut of an undulator with possible dimensions and positions of in iron shimming coils [BPW08].

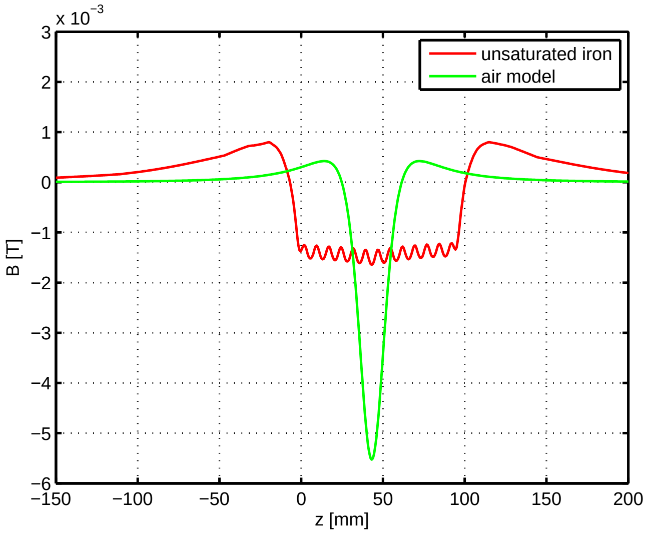

Fig. 5.9: Correction fields caused by air-core in iron shimming coils and in iron shimming coils mounted in completely unsaturated coil bodies (no current in the main coils).The cross-section of the shimming coils is 1.5 mm^2 and the correction current is $I_{corr} = 1000$ A [BPW08].

The cross-section of the lateral shim coils was 1 mm^2. They were powered with a current of $I_{corr} = 1000$ A. The nominal gap width was $g = 5$ mm.

As in the previous sections, the first simulation was performed with air-core coils and the second simulation with completely unsaturated coil bodies, i.e. without current in the main coils. The results are presented in figure 5.11. The air core coils produce a correction field distributed along the whole undulator with a peak at the z-position of the lateral shimming coils. The peak field is 0.165 mT. The problem is that the shimming coils magnetize all poles of the undulator and generate a dipole field along the whole undulator. The dipole field is modulated by a sinusiodal oszillation with a period of half the undulator period length.

5.3.4 Active lateral shim coils on a laminated undulator

To overcome the problem with the lateral shim coils a novel design of the undulator body was proposed [Ber08]. The idea is to inhibit the magnetic flux along the coil body (z-axis). The concept is explained in the following with the help of figure 5.12. The poles are made of disks with magnetic material. In between two poles is a disk made of a non magnetic material. The non magnetic material forms the grooves for the superconductive wire bundles.

In a finite element simulation with Opera-3D [VF] the pole disks were made from Vacoflux50 [Vac01] and the groove discs from copper. The lateral shimming coils were placed and powered as before. In figure 5.13 the correction field is shown. Due to the lamination the magnetic flux is concentrated at the pole equipped with the correction coil. The amplitude of the correction field is 10 mT. The two neighbouring poles are also magnetized.

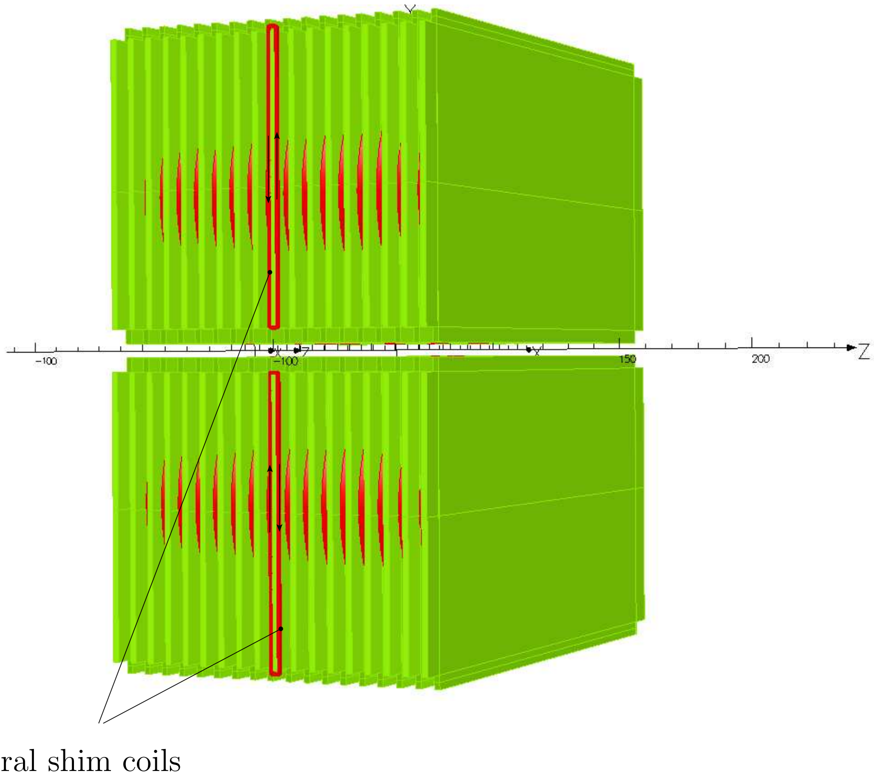

Fig. 5.10: Opera-3D [VF] model of a superconductive undulator with additional lateral shim coils.

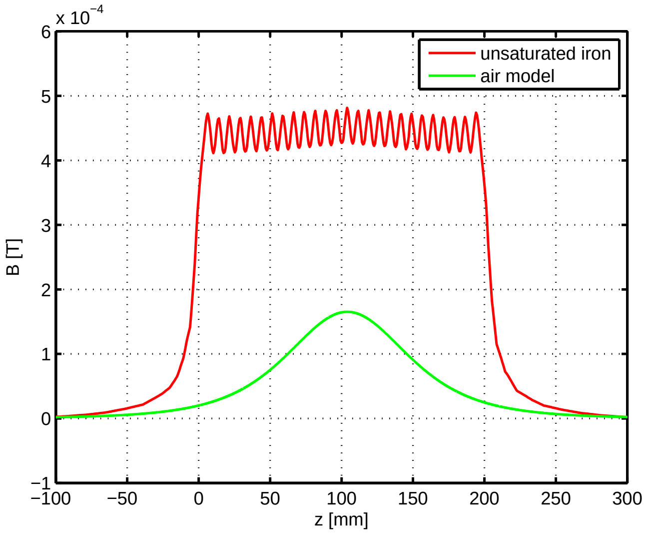

Fig. 5.11: Correction fields caused by air-core lateral shimming coils and lateral coils mounted on completely unsaturated coil bodies (no current in the main coils). The cross-section of the shimming coils is 1 mm^2 and the correction current is $I_{corr} = 1000\,\mathrm{A}$ [BPW08].

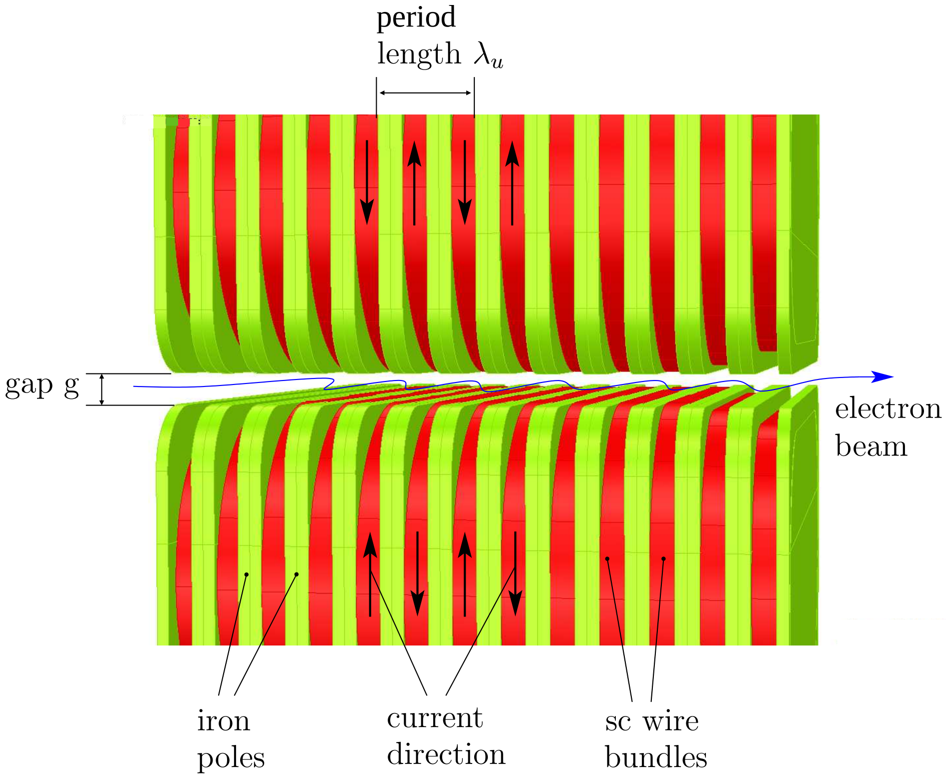

Fig. 5.12: Principle layout of a superconductive undulator, with iron poles and body (green) and superconductive wire bundles (red)

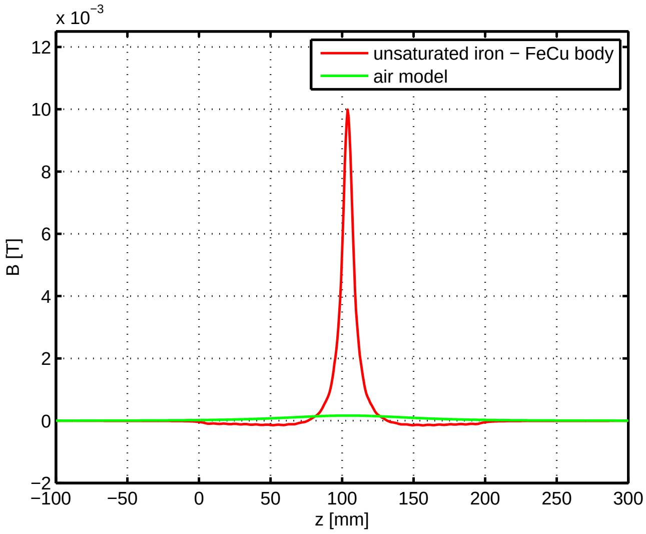

Fig. 5.13: Correction fields caused by air-core lateral shimming coils and lateral coils mounted on a laminated undulator with unsaturated pole disks (no current in the main coils). The cross-section of the shimming coils is 1 mm^2 and the correction current is $I_{corr} = 1000\,\mathrm{A}$. [Ber08]

For a laminated undulator lateral shimming coils are an effective way to correct field deviations since the shimming coils are outside the gap at the side of the undulator. The position outside the gap has the disadvantage, that the required correction currents or the number of windings in the lateral coils are higher. The unwanted magnetization of the whole coil body is inhibited by the laminated design.

6. SUPERCONDUCTORS IN MAGNETIC FIELDS

A novel shimming concept for superconductive undulators based on high temperature superconductors is described in chapters 7 and 8. Therefore, the history and basic principles of superconductivity are discussed in the following briefly.

Superconductivity was discovered by H. Kamerlingh-Onnes at the University of Leiden in the Netherlands in 1911. He and his co-workers investigated the resistivity of mercury at low temperatures. For temperatures below 4.2 K the resistance of mercury became immeasurable small. Figure 6.1 shows the resistance of mercury versus the temperature. This experiment had uncovered a new state of matter [BK04a].

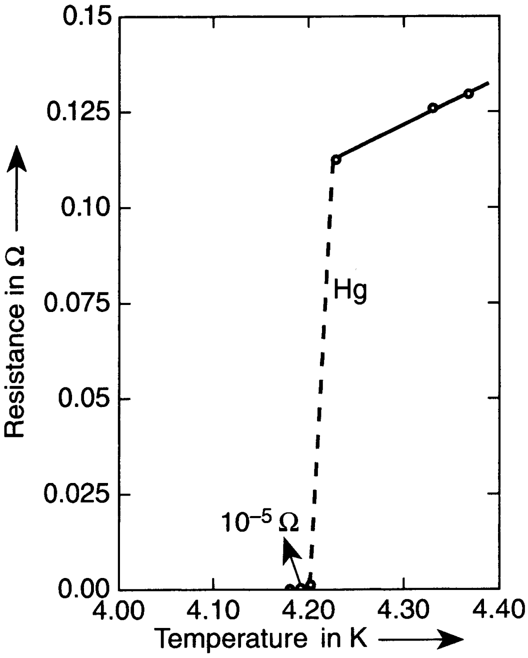

Fig. 6.1: Superconductivity of mercury [BK04a, KO11].

Since its discovery superconductivity has been found in many metals, metallic alloys and compounds. Besides the effect of a vanishing resistance it was discovered by Walther Meissner and Robert Ochsenfeld in 1933, that an external magnetic field can be expelled from the interior of superconductors except for a thin surface layer [MO33].

The theoretical understanding of superconductivity was achieved by a theory of J. Bardeen, L. N. Cooper and J. R. Schrieffer in 1957 [BCS57]. At the transition to the superconducting state the electrons condense pairwise into a new bosonic state

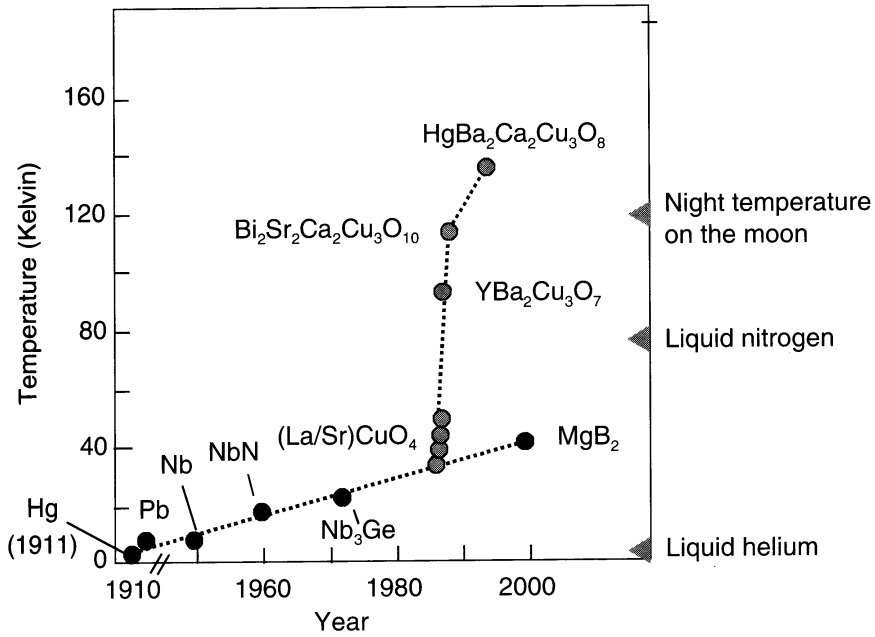

Fig. 6.2: Evolution of the superconducting transition temperatures since the discovery of superconductivity [BK04a, KT96].

(Cooper pairs), where they form a coherent matter wave with a well-defined phase. This behaviour follows the rules of quantum mechanics [BK04a].
In the late 1980s superconductivity with high transition temperatures (T_c) was discovered in a Ba-La-Cu-O system by J. G. Bednorz and K. A. Mueller [BM86]. Nowadays a large number of high temperature superconductors based on copper oxide are known. One of the most studied compounds is $YBa_2Cu_3O_7$, called YBCO, with a transition temperature around 90 K [BK04a].
The evolution of the superconducting transition temperatures since the discovery of superconductivity is shown in figure 6.2.

In the following properties and differences between type-I (mainly metal elements) and type-II (most alloys and compounds) superconductors relevant for the application in superconductive undulators are discussed.

6.1 Type-I superconductors

If an external magnetic field is applied to a type-I superconductor the field is expelled from its interior up to the critical field B_c. A thin surface layer carries the shielding currents, which expel the external field. This behaviour is called the Meissner-Ochsenfeld-Effect. Therefore, the superconducting state of a type-I superconductor is called Meissner phase. The thickness of the surface layer, the so-called penetration depth depends on the material. If the external field is increased above B_c the superconductivity breaks down and the superconductor changes from the Meissner phase into the normal conducting state. Figure 6.3 shows a simplified sketch of the expulsion of an external magnetic field by a superconducting sphere in the Meissner

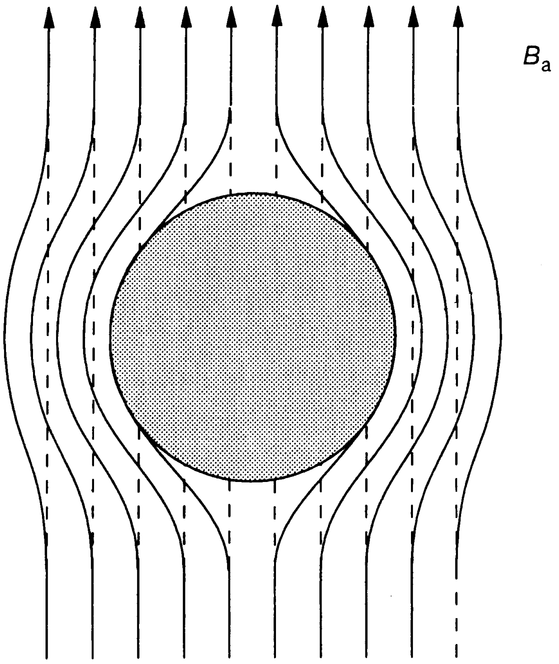

Fig. 6.3: Simplified sketch of the expulsion of an external magnetic field ($B_a < B_c$) by a superconducting sphere in the Meissner phase (solid lines). The surface layer with the shielding currents is not shown. In absence of the sphere, the field is homogeneous (dashed lines) [BK04b].

phase.
The critical field B_c depends on the temperature and reaches zero, at the transition temperature T_c. This behaviour is shown for different type-I superconductors in figure 6.4.

The current flow in a type-I superconductor in the Meissner phase is restricted to the shielding layer. Otherwise the interior of the superconductor would not be free of a magnetic field. At the critical current the magnetic field produced by the current reaches the critical field strength B_c at the surface of the superconductor. Therefore, the critical current and the critical field strength are strongly correlated [BK04c]. Table 6.1 shows the critical temperatures and the critical magnetic field at $T = 0$ for some superconducting elements. A more complete list can be found in [BK04d].

6.2 Type-II superconductors

Type-II superconductors are characterized by two critical fields: a lower B_{c1} and a higher B_{c2}. Below B_{c1} the superconductor is in the Meissner phase and behaves like a type-I superconductor. The magnetic field is expelled from the superconductor except for a thin layer at the surface. When the external field is increased above B_{c1} the magnetic field partly penetrates into the superconductor. This is called the Shubnikov phase. Above B_{c2} superconductivity vanishes and the sample is in the normal conducting phase. B_{c1} and B_{c2} are temperature dependent and zero at the

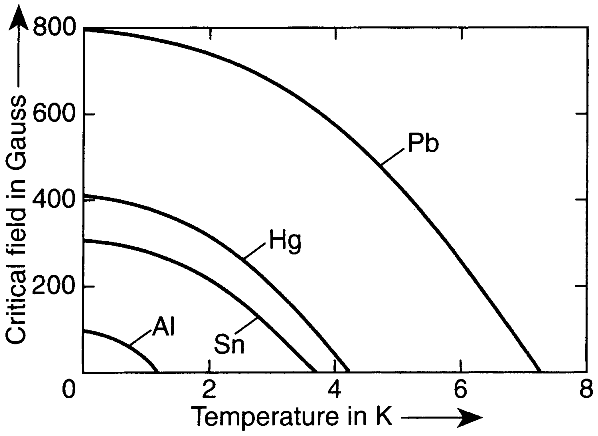

Fig. 6.4: Critical magnetic field plotted versus the temperature for different type-I superconductors. The lines mark the phase transition between the Meissner phase and the normal state [BK04b].

Element	T_c [K]	B_c at $T = 0$ [mT]
Al	1.19	10
Hg	4.15	40
Nb	9.2	195
Pb	7.2	80
Sn	3.72	30.5
Ti	0.39	17

Tab. 6.1: Overview of the transition temperatures T_c and the critical magnetic field strengths B_c at $T = 0$ for some superconducting elements. [BK04d]

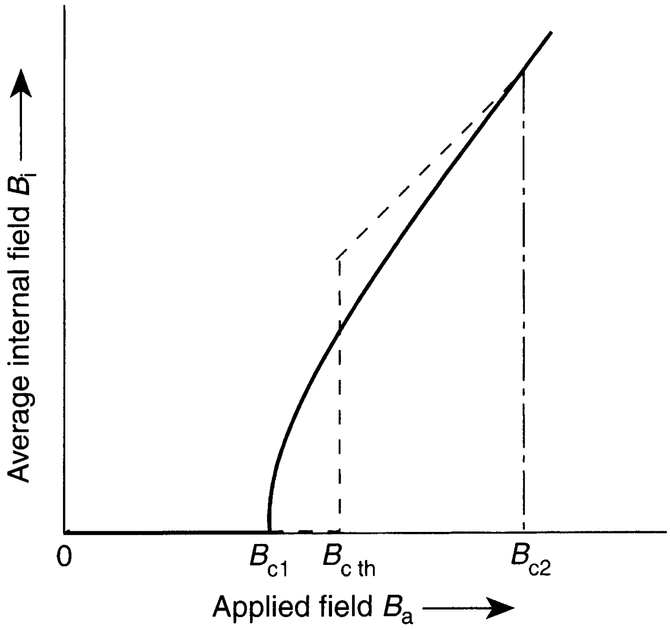

Fig. 6.5: The average magnetic field in the interior of a rod shaped type-II superconductor sample is plotted against the external magnetic field. For comparison the behaviour of a comparable type-I superconductor is shown (dashed line). B_{c1} is the lower and B_{c2} the upper critical field. B_{cth} is the critical field of the type-I superconductor [BK04b].

critical temperature T_c. B_{c2} is in general much larger than B_{c1} [BK04e].
The average magnetic field in the interior of a type-II superconductor is plotted versus the external magnetic field in figure 6.5. For comparison the behaviour of a comparable type-I superconductor is shown (dashed line) with the critical field B_{cth}. The phase diagram of a type-II superconductor is shown in figure 6.6.

If an external current is applied to a type-II superconductor at an external field below B_{c1} it acts in the same way as a type-I superconductor.
Table 6.1 shows the critical temperatures and the upper critical magnetic field B_{c2} at $T = 0$ for some type-II superconductors. For MgB_2 and $YBa_2Cu_3O_7$ B_{c2} depends on the direction of the magnetic field to the crystallographic c axis (see figure 6.7).

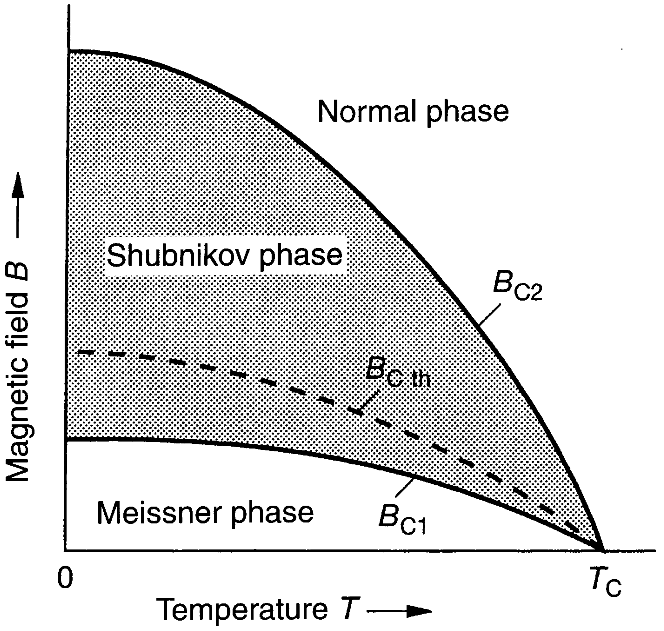

Fig. 6.6: Schematical phase diagram of a type-II superconductor, with the lower B_{c1} and upper critical field B_{c2} and the critical temperature T_c [BK04b].

type-II superconductor	T_c [K]	B_{c2} at $T = 0$ [T]	Reference
NbTi	9.6	16	[BK04d]
$NbSn_3$	18.0	24	[BK04d]
MgB_2	≈ 40	$\parallel$ to c : 2 - 5 $\perp$ to c: 15-20	[NNMZ01, BK04d]
$YBa_2Cu_3O_{7-X}$	≈ 93	$\parallel$ to c : 110 $\perp$ to c: 240	[BK04d, IOR$^+$98, NTME98]

Tab. 6.2: Overview of the transition temperatures T_c and the critical magnetic field strengths B_c at $T = 0$ for some type-II superconductors. For MgB_2 and $YBa_2Cu_3O_7$ B_{c2} depends on the direction of the magnetic field to the crystallographic c axis (see figure 6.7).

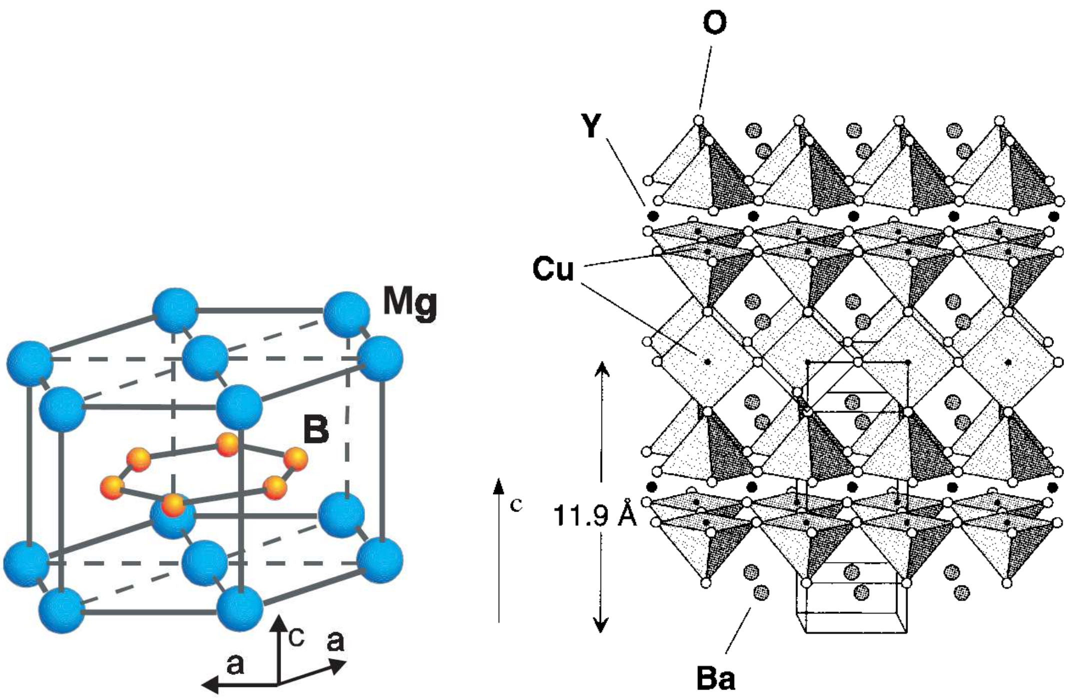

Fig. 6.7: Crystal structure of MgB_2 [BY01] (left) and $YBa_2Cu_3O_7$ [BK04d] (right).

6.2.1 Shubnikov phase

In the Shubnikov phase the magnetic field partly penetrates into the superconductor. Shielding currents flow within the superconductor and concentrate the magnetic field lines. The magnetic flux is quantized in units of

$$\Phi_0 = \frac{\pi\hbar c}{e} = 2.07 \cdot 10^{-15}\,\mathrm{Tm}^2 \text{ [Sak67]}.$$

A system of flux lines, the so called Abrikosov vortices, is generated. In case of an ideal homogeneous superconductor, the vortices arrange themselves in the form of a triangular lattice. Figure 6.8 shows a schematic drawing of a superconductor in the Shubnikov phase with magentic flux lines and shielding currents. Each flux line carries one magnetic flux quantum and is located at the corners of equilateral triangles. With increasing external field B_a, the distance between the vortices becomes smaller [BK04e].

If in an ideal type-II superconductor in the Shubnikov phase an external current I flows perpendicular to the external field B_a the current I is distributed over the whole cross-section of the superconductor. Due to the penetration of the magnetic flux into the superconductor, the current is not anymore restricted to a thin surface layer. The current also passes through the vortices. Therefore, the vortices experience a Lorentz force perpendicular to the external field and the current direction. In an ideal type-II superconductor free movement of the vortices is possible. The vortex motion through the superconductor causes dissipation, which results in the appearance of an electrical resistance [BK04c].

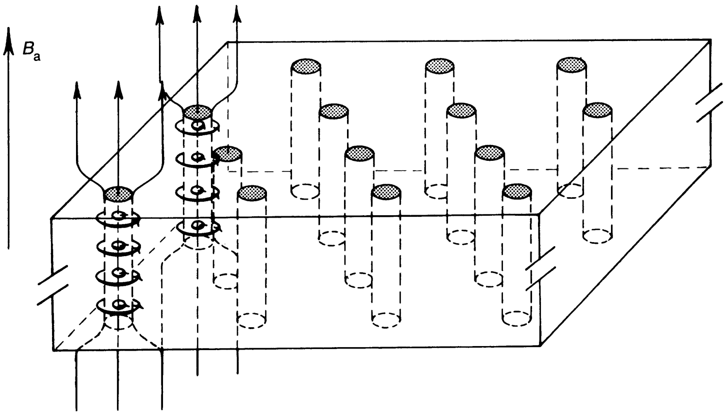

Fig. 6.8: Schematic drawing of a superconductor in the Shubnikov phase with magentic flux lines and shielding currents. The magnetic field and the supercurrents are only shown for two vortices [BK04e].

In real type-II superconductors the vortices are energetically strongly bound to favorable locations, so-called pinning centers. All kinds of inhomogeneities can act as pinning centers e.g. lattice defects, etc. As long as the Lorentz force F_L is smaller than the pinning force F_H, the vortices cannot move. Therefore current transport without any dissipation is possible in real type-II superconductors. The critical current density is reached when $F_L = F_H$, the vortices start to move and a resistance is observed. The critical current depends strongly on the pinning force.

6.2.2 YBCO

$YBa_2Cu_3O_{7-X}$ belongs to the group of cuprates and is one of the best examined high temperature superconductors. Cuprates have a layered structure (see right sketch of figure 6.7), where copper oxide layers alternate with intermediate layers of other elements. Therefore, the direction of the external field, i.e. parallel or perpendicular to the layer structure, is important for the upper critical field. Normally transport currents are applied parallel to the layer structure (perpendicular to the c-axis).
YBCO is generally produced as thin film, grown on monocrystalline substrates. The first wired conductors based on YBCO on flexible substrates are availabe now.
As presented in table 6.2 YBCO has a transition temperature of about 93 K and the upper critical field is well above 100 T. Figure 6.9 shows the critical current densities of thin YBCO layers versus the external magnetic field at different temperatures. Maximum current densities of $500\,\frac{\mathrm{kA}}{\mathrm{mm}^2}$ can be reached at 4.2 K[RSSI90].

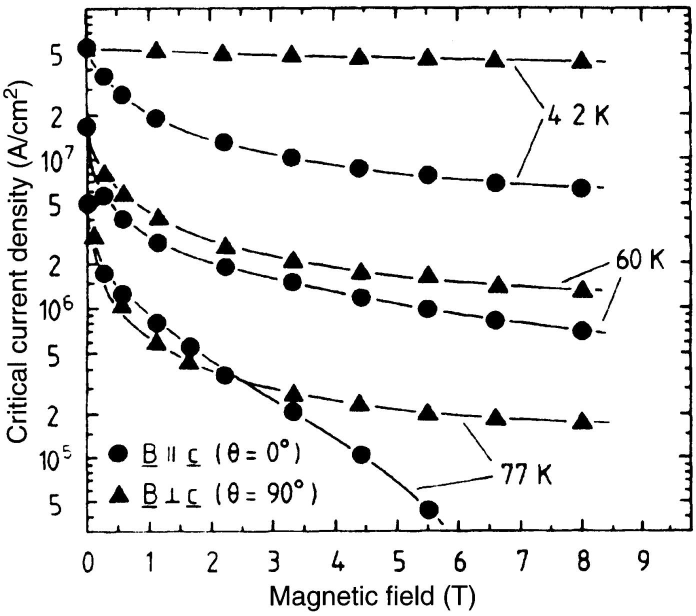

Fig. 6.9: Critical current density of a $YBa_2Cu_3O_7$ thin film for three temperature plotted versus the external magnetic field. The magnetic field is either parallel or perpendicular to the crystallographic c-axis [RSSI90, BK04c].

7. INDUCTION SHIMMING: CONCEPT

Shimming of undulators is a time consuming procedure for permanent magnet, cryogenic or superconductive undulators. It has to be performed iteratively: field measurement, field correction and verification. This procedure means for superconductive undulators that the coils have to be cooled down and warmed up several times. Active shimming concepts always require additional current feed-throughs, which complicate the design of the cryostat and increase the heat transfer to the cold mass. Therefore only a small number of individually powered correction coils can be used for active shimming.
Active shimming becomes even more complex, due to the different current dependencies of the field errors caused by the different types of mechanical deviations. Moreover, the errors caused by the iron are subject to hysteresis and require complex correction algorithms.

Therefore, in the following a passive shimming concept is presented, which can correct field errors automatically [WBR08, WBP^{+}08c].

7.1 Induction-shimming: Theory

The induction shimming concept is based on Faraday's law of induction

$$\oint\limits_C \tilde{\mathbf{E}} d\vec{l} = -\frac{d}{dt}\int\limits_S \tilde{\mathbf{B}} d\vec{A}, \tag{7.1}$$

where $\tilde{\mathbf{B}}$ is the magnetic flux density over the area S enclosed by the contour C. $\tilde{\mathbf{E}}$ is the electrical field strength. Using an ideal conductor along the contour, i.e. a superconductive closed loop, equation (7.1) is reduced to

$$0 = \frac{d}{dt}\int\limits_S \tilde{\mathbf{B}} d\vec{A}. \tag{7.2}$$

This means that the change in magnetic flux through the closed loop is inhibited by the induced current [KSW00].
To demonstrate the basic principle a uniform magnetic field is considered in a first step.

7.1.1 One period with closed-loop

Assume a superconductive loop positioned on the beam-sided surface of an undulator coil. The width of the superconductive closed loop in the beam direction is one period so that the enclosed total flux in case of an ideal undulator is zero. If the magnetic flux density in each half period is different (see figure 7.1) the magnetic flux inclosed by the superconductive loop is not zero. When the field is switched on at t_0 a current is induced into the closed loop according to equation (7.2). Therefore, the magnetic flux in each half period is brought to the same absolute level with opposite sign. The magnetic flux in the first and second half period u_1 and u_2 and the correction flux y_1 produced by the loop superpose to zero

$$y_1 + u_1 + u_2 = 0. \tag{7.3}$$

The flux w_1 and w_2 in each half-period is changed to

$$\begin{aligned} w_1 &= u_1 + \frac{1}{2} y_1 && (7.4) \\ w_2 &= u_2 + \frac{1}{2} y_1. && (7.5) \end{aligned}$$

Equations (7.4) and (7.5) and (7.3) yield

$$\begin{aligned} w_1 + w_2 &= 0 && (7.6) \\ \rightarrow w_2 = -w_1 &= w. \end{aligned}$$

Equation (7.4) and (7.5) can be rewritten as follows

$$\begin{aligned} w &= -u_1 - \frac{1}{2} y_1 \\ w &= u_2 + \frac{1}{2} y_1 \end{aligned}$$

and solved for w

$$w = \frac{-u_1 + u_2}{2}. \tag{7.7}$$

The current in the loop equalizes the field strength according to equation 7.2. This is shown in figure 7.1 c.

In general the closed-loops must be arranged in a way that the magnetic flux surrounded by one loop is equal to zero in the case of an undisturbed undulator magnetic field. This is the case for integer multiples of the undulator period-length. In the following only closed-loops over one period-length will be considered.

7.1.2 Two overlapping closed-loops

Induction shimming is supposed to be used for field error correction of complete undulators with 100 or more periods. Thus, the above shown principle has to be expanded and coupling between the single loops is needed. This can be done by an overlap between neighbouring loops.

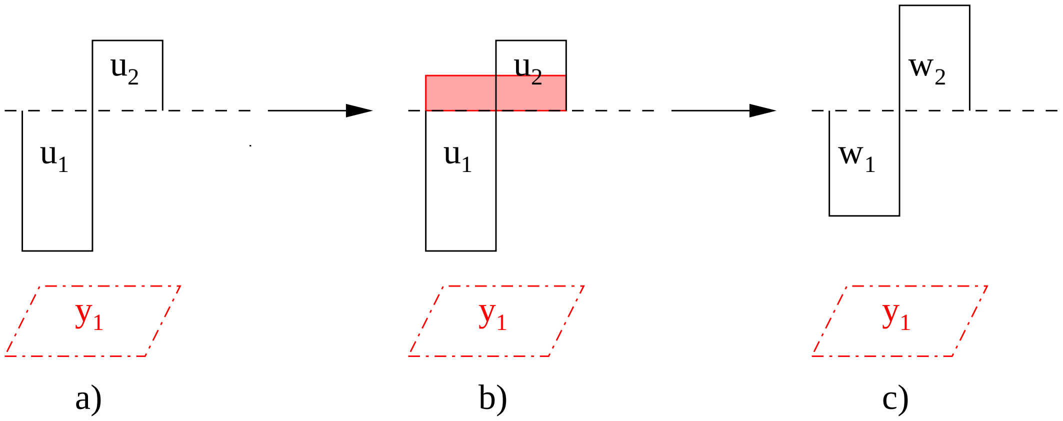

Fig. 7.1: Influence of a closed loop on a one period rectangular magnetic field with different magnetic flux densities in each half period.

In the following the calculation is extended to 1.5 periods covered by two overlapping closed loops (see figure 7.2). For the closed-loops Faraday's law results in

$$y_1 + u_1 + u_2 + \frac{1}{2}y_2 = 0 \tag{7.8}$$

$$y_2 + u_2 + u_3 + \frac{1}{2}y_1 = 0. \tag{7.9}$$

With the resulting fluxes in each half period

$$w_1 = u_1 + \frac{1}{2}y_1 \tag{7.10}$$

$$w_2 = u_2 + \frac{1}{2}y_1 + \frac{1}{2}y_2 \tag{7.11}$$

$$w_3 = u_3 + \frac{1}{2}y_2 \tag{7.12}$$

equations (7.8) and (7.9) yield

$$\begin{aligned} w_1 + w_2 &= 0 \\ w_2 + w_3 &= 0 \end{aligned}$$

or

$$w_2 = -w_1 = -w_3 = w. \tag{7.13}$$

Substituting w into equations (7.10),(7.11) and (7.12) gives

$$\begin{aligned} w &= -u_1 - \frac{1}{2}y_1 \\ w &= u_2 + \frac{1}{2}y_1 + \frac{1}{2}y_2 \\ w &= -u_3 - \frac{1}{2}y_2 \end{aligned}$$

or

$$w = \frac{-u_1 + u_2 - u_3}{3}. \tag{7.14}$$

Figure 7.2 depicts the above discussed results.

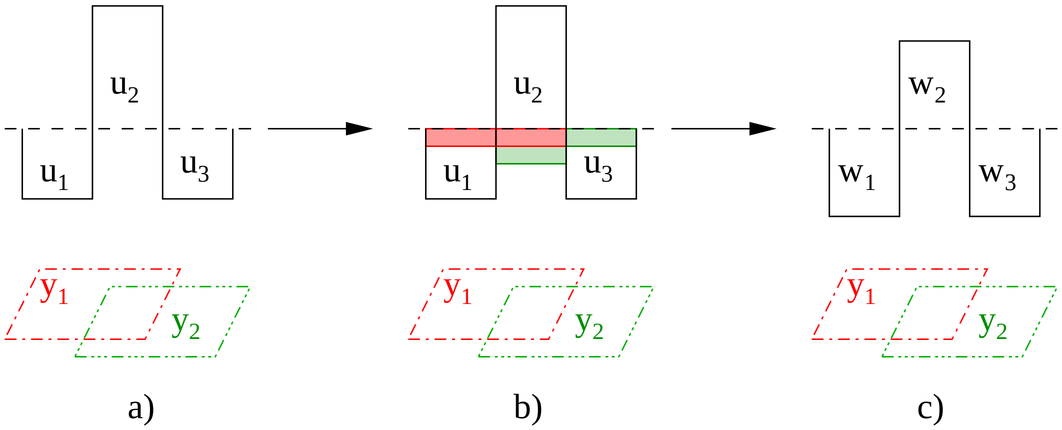

Fig. 7.2: Behaviour of two overlapping closed-loops in a rectangular magnetic field with different field amplitudes.

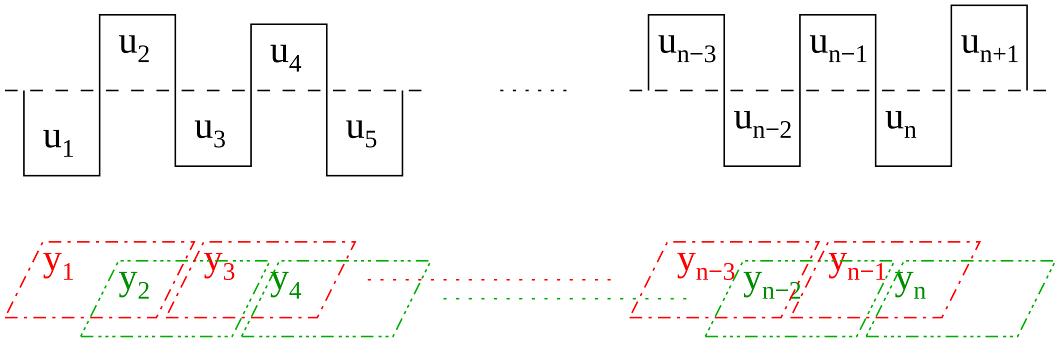

Fig. 7.3: Rectangular field with $n+1$ half periods and n overlapping closed loops

7.1.3 Generalization for n closed-loops

In the following the induction-shimming concept with superconductive closed-loops is extended to n closed-loops
The system is shown in figure 7.3, with the magnetic flux u_n in the n-th half-period ($n = 1, 2, 3, ...$), the correction flux y_m produced by the closed-loop m ($m = 1, 2, 3, ..., n-1$) and the resulting fluxes w_n.

The set of equations for Faraday's law can than be written as

$$\begin{aligned}
y_1 + u_1 + u_2 + \frac{1}{2}y_2 &= 0 \\
y_2 + u_2 + u_3 + \frac{1}{2}y_1 + \frac{1}{2}y_3 &= 0 \\
&\vdots \\
y_{n-1} + u_{n-1} + u_n + \frac{1}{2}y_{n-2} + \frac{1}{2}y_n &= 0 \\
y_n + u_n + u_{n+1} + \frac{1}{2}y_{n-1} &= 0. \qquad (7.15)
\end{aligned}$$

The magnetic flux in each half period is

$$\begin{aligned} w_1 &= u_1 + \frac{1}{2}y_1 \\ w_2 &= u_2 + \frac{1}{2}y_1 + \frac{1}{2}y_2 \\ &\vdots \\ w_n &= u_n + \frac{1}{2}y_{n-1} + \frac{1}{2}y_n \\ w_{n+1} &= u_{n+1} + \frac{1}{2}y_n. \end{aligned} \tag{7.16}$$

Substituting these equations into the closed-loop equations (7.15) gives

$$\begin{aligned} w_1 + w_2 &= 0 \\ w_2 + w_3 &= 0 \\ &\vdots \\ w_{n-1} + w_n &= 0 \\ w_n + w_{n+1} &= 0, \end{aligned}$$

which is equal to

$$w = \pm w_1 = \mp w_2 = ... = \pm w_n = \mp w_{n+1}. \tag{7.17}$$

The magnetic flux in each half period becomes

$$\begin{aligned} w &= \pm u_1 \pm \frac{1}{2}y_1 \\ w &= \mp u_2 \mp \frac{1}{2}y_1 \mp \frac{1}{2}y_2 \\ &\vdots \\ w &= \pm u_n \pm \frac{1}{2}y_{n-1} \pm \frac{1}{2}y_n \\ w &= \mp u_{n+1} \mp \frac{1}{2}y_n, \end{aligned}$$

which can be solved for w:

$$w = \frac{\pm u_1 \mp u_2 \pm \ldots \pm u_n \mp u_{n+1}}{n+1}. \tag{7.18}$$

As with the one and two loop systems described before, the system of n overlapping closed-loops adjusts the absolute values of the magnetic flux in each half period to the same level.

7.2 Generalization for Biot-Savart closed-loops

In the following the concept is extended to sinusoidal fields and the field produced by the current in the loops is described by the law of Biot-Savart.

For the sake of simplicity the closed-loops are considered to consist of ideally superconducting long straight wires perpendicular to the beam direction (z-axis). The loop parts parallel to the e-beam direction can be neglected due to their large distance from the e-beam.

7.2.1 Faraday's law for overlapping closed-loops in a long undulator

Faraday's law of induction (see equation (7.1)) for one closed-loop can be written as

$$\dot{I} = -\frac{1}{L}\dot{\Phi}. \tag{7.19}$$

Where $\dot{\Phi}$ is the time derivative of the magnetic flux through the closed-loop, L is the self-inductance of the loop and $\dot{I}$ the time derivative of the induced current. For an induction-shimming scheme with overlapping closed loops the coupling between the loops also has to be considered. The coupling between loop i and loop j with a mutual inductance M_{ij} is defined by

$$\dot{I}_i = M_{ij}\dot{I}_j. \tag{7.20}$$

Combining equation (7.19) and (7.20) and solving for $\dot{\Phi}$ gives

$$\dot{\Phi}_i = L\left(\sum_{j\neq i} M_{ij}\dot{I}_j - \dot{I}_i\right). \tag{7.21}$$

When the current in the undulator main coil is turned on at the time t_0 the flux through the closed-loops is changed from zero to a certain value and a current I is induced. Integration of equation (7.21) yields

$$\Phi_i = L\left(\sum_{j\neq i} M_{ij}I_j - I_i\right). \tag{7.22}$$

The self-inductance L and the mutual inductances M_{ij} are defined by the geometrical arrangement and the design of the closed-loops.

7.2.2 Biot-Savart's law for overlapping closed-loops in a long undulator

In a real superconductive undulator a set of overlapping closed-loops will be mounted in the way shown in figure 7.4. The undulator consists of N periods and the shimming system of $2N-1$ closed-loops. The loops are numbered from the entrance of the undulator (1,2,...,2N-1). Errors of the undulator magnetic field induce correction currents in the closed-loops. The main field and the correction fields superpose in the beam plane. For this arrangement of superconductive closed-loops the self-inductance and the mutual inductances will be determined in the following with the help of Biot-Savart's law.

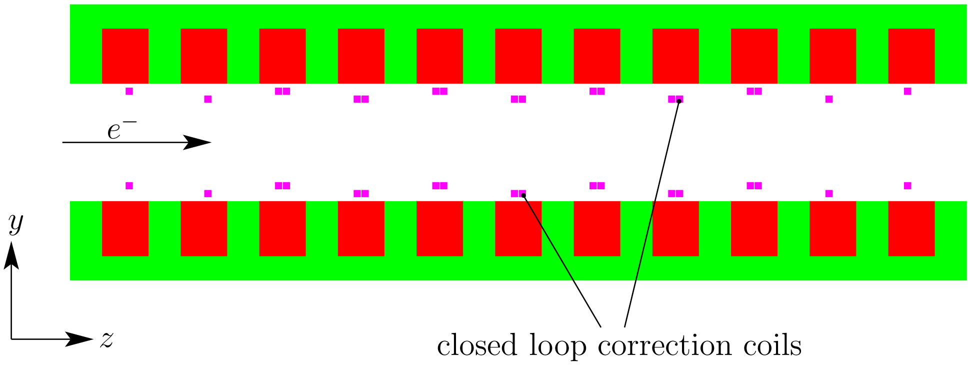

Fig. 7.4: Cross section of an undulator with the main coils (green: iron; red: superconductive wire-bundles) and overlapping closed-loops for correction (magenta) placed close to the main coils.

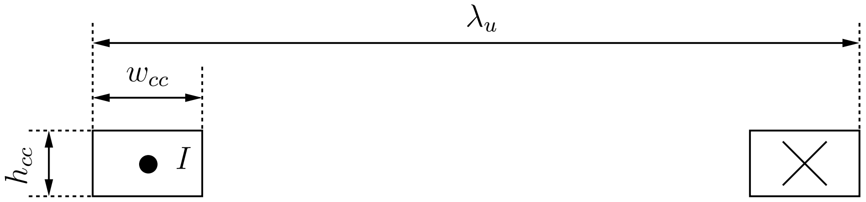

Fig. 7.5: One closed-loop made out of two long straight wires .

The magnitude of the magnetic flux density $\tilde{\mathbf{B}}$ at a point P at the distance $R = \sqrt{z^2 + y^2}$ caused by a current I in a long straight wire, running parallel to the x-axis, is given by [Jac99b]

$$|\tilde{\mathbf{B}}| = \frac{\mu_0}{4\pi} IR \int_{-\infty}^{\infty} \frac{dl}{(R^2 + l^2)^{3/2}} = \frac{\mu_0}{2\pi}\frac{I}{R}. \tag{7.23}$$

$\mu_0 = 4\pi \cdot 10^{-7} \, \frac{\text{Vs}}{\text{Am}}$ is the magnetic permeability in vacuum. The coordinate system is defined in figure 7.4.
With $\cos\alpha = \frac{z}{R}$ and the above definition of R the y-component of the magnetic flux density at a point P can be calculated as

$$B_y(y,z) = |\tilde{\mathbf{B}}| \cos\alpha = \frac{\mu_0 I}{2\pi} \frac{z}{z^2 + y^2}. \tag{7.24}$$

Where z and y are the distances from the center of the conductor to point P. The conductor has the dimensions $w_{cc} \times h_{cc}$.

Treating this as a two dimensional problem the magnetic flux produced by the loop shown in figure 7.5 is

$$\begin{aligned} \Phi &= 2 \cdot \int_{w_{cc}/2}^{\lambda_u - \frac{3}{2}w_{cc}} B_y(z')dz' = 2 \cdot \frac{\mu_0 I}{2\pi} \int_{w_{cc}/2}^{\lambda_u - \frac{3}{2}w_{cc}} \frac{1}{z'} dz' \\ &= 2 \cdot \frac{\mu_0}{4\pi} \cdot I \left(\ln \frac{(\lambda_u - \frac{3}{2}w_{cc})^2}{(\frac{w_{cc}}{2})^2} \right) = -L \cdot I. \end{aligned} \tag{7.25}$$

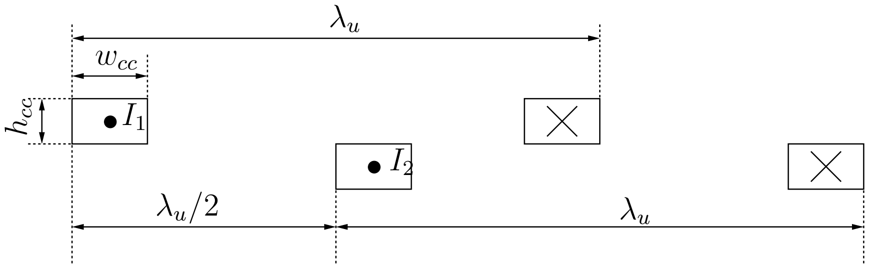

Fig. 7.6: Two overlapping closed-loops with induced currents I_1 and I_2.

The mutual inductances M_{ij} for $i \neq j$ and $i, j = 1...(2N-1)$ can be calculated with the help of figure 7.6. Defining

$$a_k = L \cdot M_{i,j} \tag{7.26}$$

with $k = |j - i|$ and

$$\xi_k = \begin{cases} 1 & \text{if } k \text{ is odd} \\ 0 & \text{if } k \text{ is even} \end{cases},$$

a_k is given by

$$\begin{aligned} a_k &= \frac{\mu_0}{2\pi} \int_{\frac{k}{2}\lambda_u + \frac{1}{2}w_{cc}}^{(\frac{k}{2}+1)\lambda_u - \frac{3}{2}w_{cc}} \frac{z'}{z'^2 + (\xi_k h_{cc})^2} dz' \\ &- \frac{\mu_0}{2\pi} \int_{(\frac{k}{2}-1)\lambda_u + \frac{3}{2}w_{cc}}^{\frac{k}{2}\lambda_u - \frac{1}{2}w_{cc}} \frac{z'}{z'^2 + (\xi_k h_{cc})^2} dz', \end{aligned} \tag{7.27}$$

or

$$\begin{aligned} a_k = \frac{\mu_0}{4\pi} &\left(\ln \left[\frac{((\frac{k}{2}+1)\lambda_u - \frac{3}{2}w_{cc})^2 + (\xi_k h_{cc})^2}{(\frac{k}{2}\lambda_u + \frac{1}{2}w_{cc})^2 + (\xi_k h_{cc})^2} \right] \right) \\ -\frac{\mu_0}{4\pi} &\left(\ln \left[\frac{(\frac{k}{2}\lambda_u - \frac{1}{2}w_{cc})^2 + (\xi_k h_{cc})^2}{((\frac{k}{2}-1)\lambda_u + \frac{3}{2}w_{cc})^2 + (\xi_k h_{cc})^2} \right] \right). \end{aligned} \tag{7.28}$$

The integrals were solved analytically[BSMM01].

Equation (7.22) becomes

$$\begin{pmatrix} \Phi_1 \\ \Phi_2 \\ \\ \vdots \\ \Phi_{2N-1} \end{pmatrix} = -M_{cc} \cdot \begin{pmatrix} I_1 \\ I_2 \\ \\ \vdots \\ I_{2N-1} \end{pmatrix}, \tag{7.29}$$

with the symmetrical matrix

$$M_{cc} = \begin{pmatrix} L & a_1 & a_2 & \cdots & a_{2N-1} \\ a_1 & & & \ddots & \vdots \\ a_2 & & \ddots & & a_2 \\ \vdots & \ddots & & & a_1 \\ a_{2N-1} & \cdots & a_2 & a_1 & L \end{pmatrix}, \tag{7.30}$$

The resulting magnetic field along the beam axis can be written in the form

$$B_y(z) = B_{y,main}(z) + \sum_{l=1}^{2N-1} B_{y,l}(z), \tag{7.31}$$

where $B_{y,main}(z)$ is the magnetic field along the beam axis generated by the undulator main coils and $B_{y,l}(z)$ is the field generated by the closed-loop l (see equation (7.24)).

7.3 Simulations

In the following it is assumed that the magnetic field is sinusoidal. Amplitude and period-length can be varied in each half period. The mid-plane of the superconductive closed-loops is considered to be 1 mm away from the source (main coil) and 2.5 mm from the beam plane. The undisturbed field amplitude on axis is 1 T.

7.3.1 Correction of a single field-error

For a first simulation a three period undulator has been modelled with a 10% too high second maximum. A single pole, which is closer to the beam than the others would cause this error. The field plot along the beam axis with and without induction-shimming is shown in figure 7.7. The second maximum was reduced by about 7% from 1.1 T to 1.03 T. The absolute values of the neighbouring minima were increased to 1.025 T and the first maximum was increased to 1.015 T. The changes in the third maximum and minimum were negligible. The error previously localized in one half period was reduced and distributed over two periods.

The comparisons of the first and the second field integrals with and without induction-shimming are shown in figure 7.8. The final value of the first field integral was reduced by a factor of two and the sign changed. The final value of the second field integral was reduced by 15%.

Considering an additional region of ten periods, i.e. 140 mm, at each side of the undulator, the final values of the first field integral converge. This is shown in figure 7.9. The correction of the first field integral is only locally.

7.3.2 Monte-Carlo simulations

As discussed in chapter 3 mechanical deviations are the main reasons for phase errors in superconductive undulators. Therefore it is important to examine the influence of

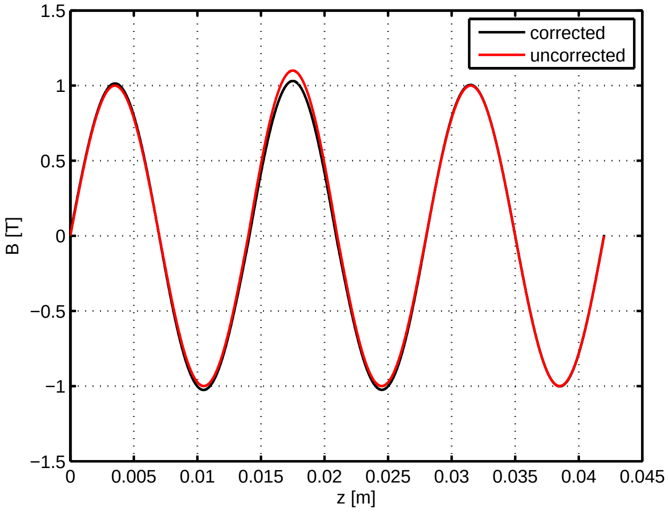

Fig. 7.7: Comparison of the magnetic field along the beam axis with (black) and without (red) induction shimming.

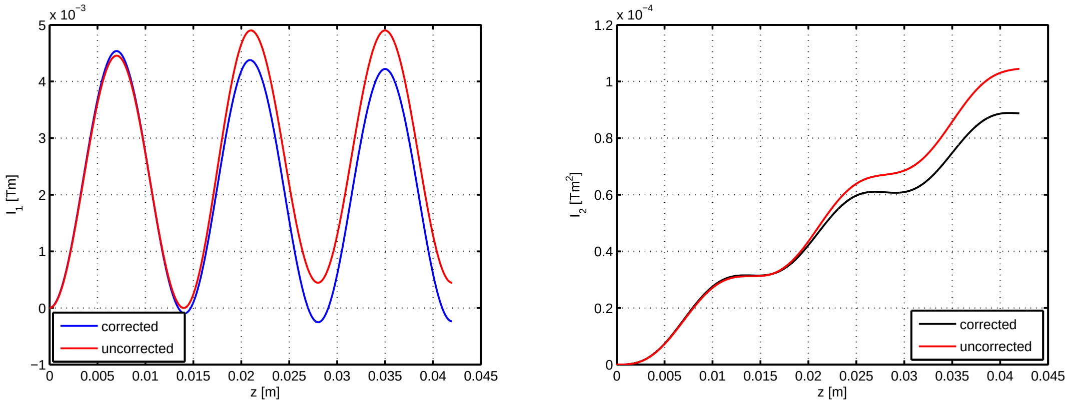

Fig. 7.8: Comparison of the first/second field integral along the beam axis with (blue/black) and without (red/red) induction shimming.

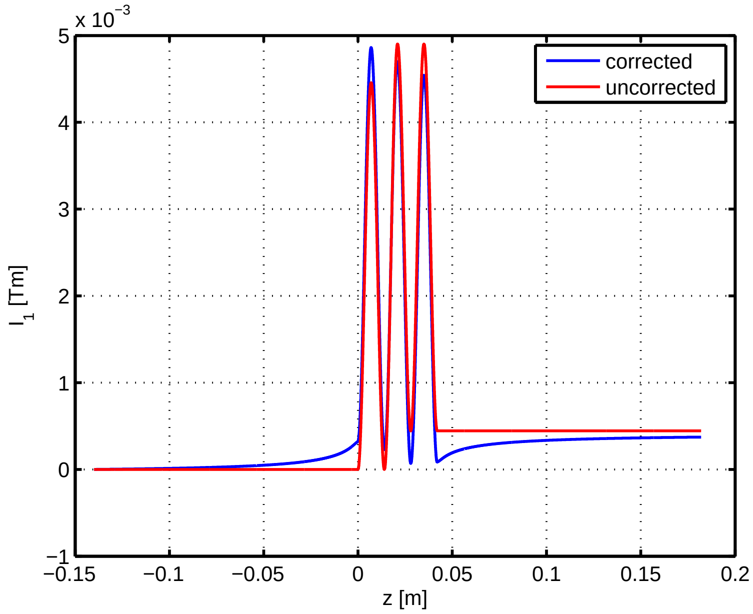

Fig. 7.9: Comparison of the first field integral along the beam axis with (blue) and without (red) induction shimming. The considered region was extended by 10 periods on each side.

the proposed induction-shimming scheme onto the phase error distributions caused by statistically distributed mechanical variations.

Figure 7.10 shows the phase error distribution calculated for 1000 undulators with and without induction-shimming. The undulators consist of 50 periods. Normally distributed variations of the wire-bundle positions (anti-symmetric field deviation) and pole positions (single field distortion at one extremum) both with $\sigma_{\frac{\Delta B}{B}} = 3 \cdot 10^{-3}$ were assumed.

In a second step the influence of a misaligned induction-shimming system on the efficiency of the correction was examined. Therefore the whole induction-shimming loop arrangement was moved 0.5 mm against the zero crossings of the undulator field. Figure 7.11 shows the phase error distribution calculated for 1000 undulators with the misaligned induction-shimming system. The width of the phase-error distribution with induction-shimming is significantly lower and the tail of the distribution is shorter. In case of a misaligned induction-shimming system, the correction efficiency is reduced. The results are shown in table 7.1.

In addition angular misalignments of the shimming system have to be considered. A lateral cant (roll) of the shim substrate will 1) reduce the flux enclosed by the loop and therefore reduce the correction current and 2) generate additional horizontal field components.

A short estimation shows, that these effects are small and therefore can be neglected in relation to the longitudinal misalignment: Assume a width of the substrate of 50 mm (x-axis). The shim substrate is mounted at $x = -25$ mm directly on the coil surface and at $x = +25$ mm it is misplaced by 1 mm from the coil surface. The substrate has an angle (dy/dx) relative to the coil surface of arctan(1/50). The

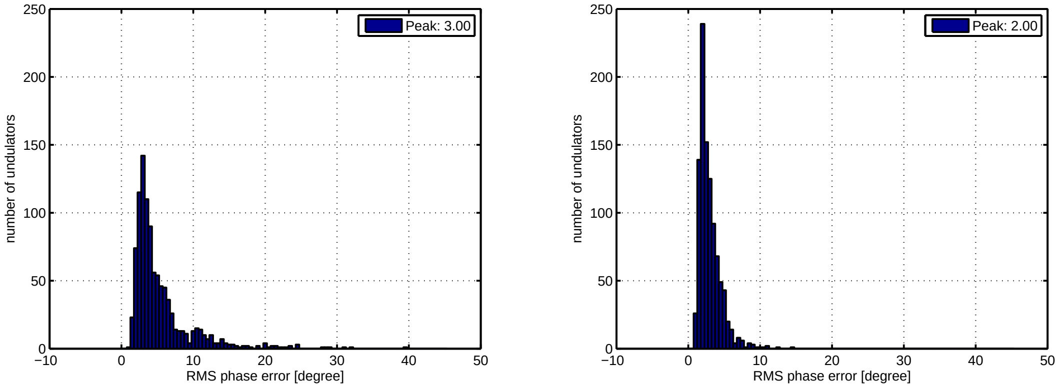

Fig. 7.10: Phase-error distribution for 1000 50-period undulators without (left) and with (right) induction-shimming; $\sigma_{\frac{\Delta B}{B},coil} = \sigma_{\frac{\Delta B}{B},pole} = 3 \cdot 10^{-3}$

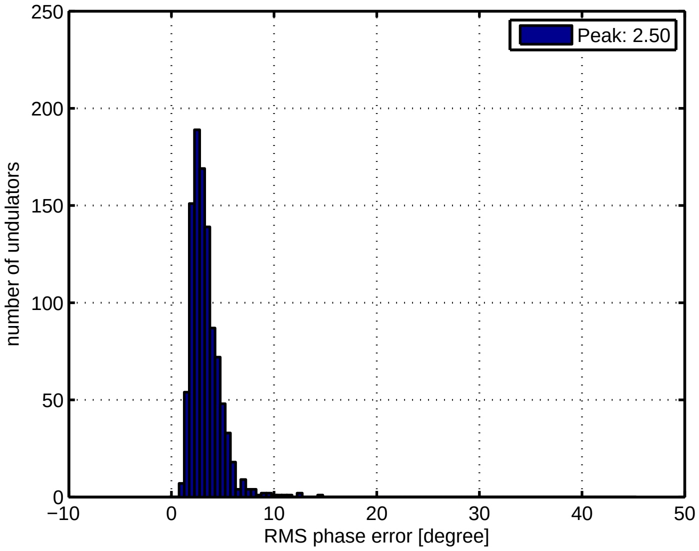

Fig. 7.11: Phase-error distribution for 1000 50-period undulators with a induction-shimming system misaligned by 0.5 mm against the zero crossings of the undulator main field; $\sigma_{\frac{\Delta B}{B},coil} = \sigma_{\frac{\Delta B}{B},pole} = 3 \cdot 10^{-3}$

	without ind.-shim.	with ind.-shim.	misaligned ind.-shim.
peak of the distribution	3.0°	2.0°	2.5°
50%-level	3.9°	2.5°	3.0°
99.7%-level	29°	11°	11.5°

Tab. 7.1: Comparison of the confidence-levels in the phase-error distributions with and without induction-shimming (ind.-shim.).

projected loop area and therefore the enclosed flux is reduced to $\cos(\arctan(1/50)) = 99.98\%$ of the flux enclosed by a perfectly positioned loop. The induced current and the total correction field are reduced by about the same amount. The correction field has in first order an angle of $\arctan(1/50)$ to the y-axis. The vertical correction field has then a value of $(\cos(\arctan(1/50)))^2 = 99.96\%$ and the additionally produced horizontal field component a value of $\sin(\arctan(1/50)) \cdot \cos(\arctan(1/50)) = 1.99\%$ of the perfect vertical correction field.
Assuming that the shimming system can correct field errors not larger than 1 % of the main coil field the horizontal field component is negligible small. In addition a misplacement by 1 mm seems to be a dramatic value: 0.1 mm is more likely the worst case. In this case the effects are reduced by a factor of ten compared to the example given above.
Since the shim substrate is in general much longer than wide a rotation around the vertical axis (y-axis) within the mechanical limits has an even smaller effect on the shimming efficiency than the one caused by a lateral cant.

Also, the positioning of the induction-shimming system can be done iteratively. Therefore, the misalignment can be reduced to an acceptable limit [WBP$^+$08b].

8. INDUCTION SHIMMING: EXPERIMENT

To prove the induction-shimming concept an experiment has been performed. This experiment was carried out with a short test device mounted on a undulator mock-up coil in the bath cryostat CASPER [MGS+08] at Forschungszentrum Karlsruhe, Germany.
In the following the experimental setup is described and the measurement results are presented and discussed.

8.1 Experimental Setup

The test system of seven overlapping closed-loops was manufactured by the company THEVA, Ismaning, Germany. It consists of a four and a three closed-loop structure. The superconductive material of the closed-loops is a 330 nm thick YBCO layer on a 500 μm thick sapphire substrate. The loops are rectangular with thin bars parallel to the main coil wire bundles and big bars parallel to the beam axis. The thin bars have a width of 1 mm and the big bars a width of 10 mm. In the x-z-plane each closed-loop has the dimensions $14 \times 44\,\text{mm}^2$. The big bars were introduced to keep the critical current at the field extrema as high as in the thin bars at the zero crossings of the field. Due to a mask error during structuring, one thin bar of the first loop has a reduced width. The critical current will first be reached in this loop. The YBCO layers are covered by a 200 nm thick gold layer for protection (see figure 8.1). Neglecting the structuring error in the first loop, the smallest cross-section of the closed-loops is $3.3 \cdot 10^{-4}\text{mm}^2$. The whole system covers four full undulator periods. A photograph of the seven loops test device is shown in figure 8.1.

The induction shimming device was tested with a 8.5 period superconductive mock-up coil produced by Babcock Noell GmbH, Wuerzburg, Germany. The mock-up coil has a period length of 14 mm. Each groove is filled with 28 round NbTi wires with a diameter of 0.8 mm. The cross-section of the wire is about $0.5\,\text{mm}^2$.
The mock-up coil starts and ends with a block made from magnetic iron. The magnetization of these blocks reduces the quality of the undulator field.
The stacked induction shimming device was mounted into a thin frame made of glass-reinforced plastic (GRP). For electrical insulation a 25 μm thick Kapton foil was placed between the two closed-loop structures. This arrangement is shown schematically in figure 8.2.
The frame with the induction-shimming device was then mounted on the surface of the mock-up coil. The mid-plane of the induction-shimming system was 1 mm away from the mock-up coil surface. The described arrangement is depicted in figure 8.3.

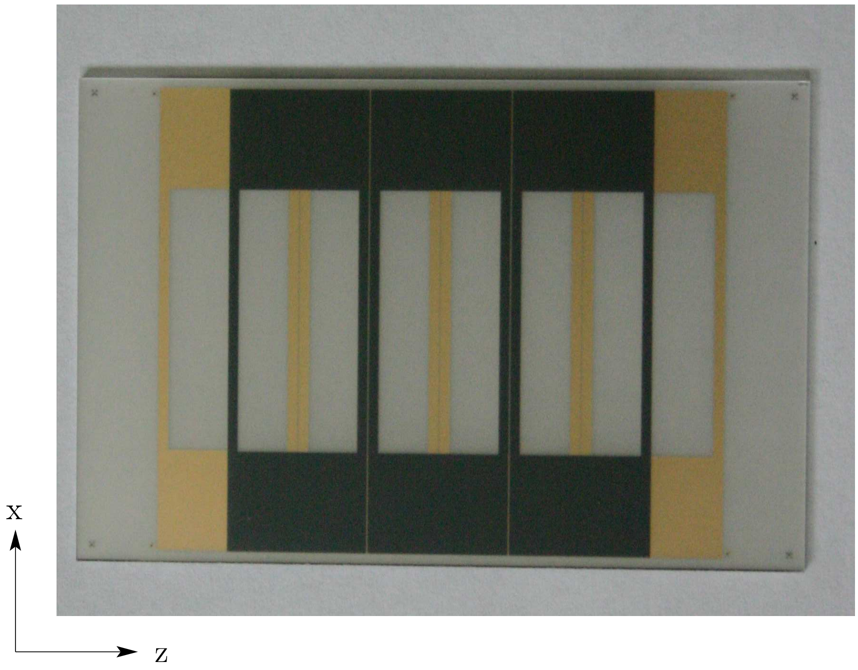

Fig. 8.1: Photograph of the induction-shimming test device with seven overlapping closed loops used for the experiment. It consists of a four and a three closed-loop YBCO structure on sapphire substrates. The substrate size is about 78 × 50mm^2. The closed loops are lying nearly in one plane.

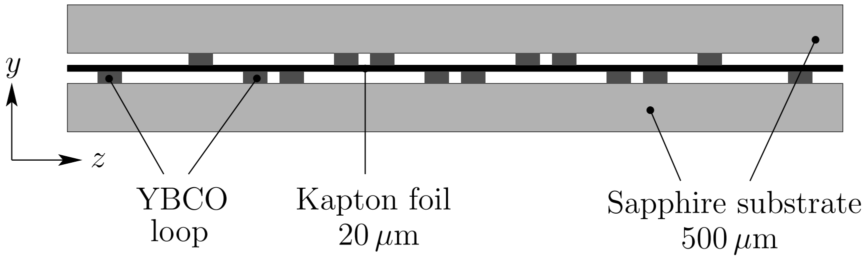

Fig. 8.2: Cut through the stacked induction-shimming structure with the substrate. The YBCO loops are arranged on a 500 μm thick sapphire substrate. The thickness of the YBCO layer is 330 nm. The period of the mock-up is 14 mm

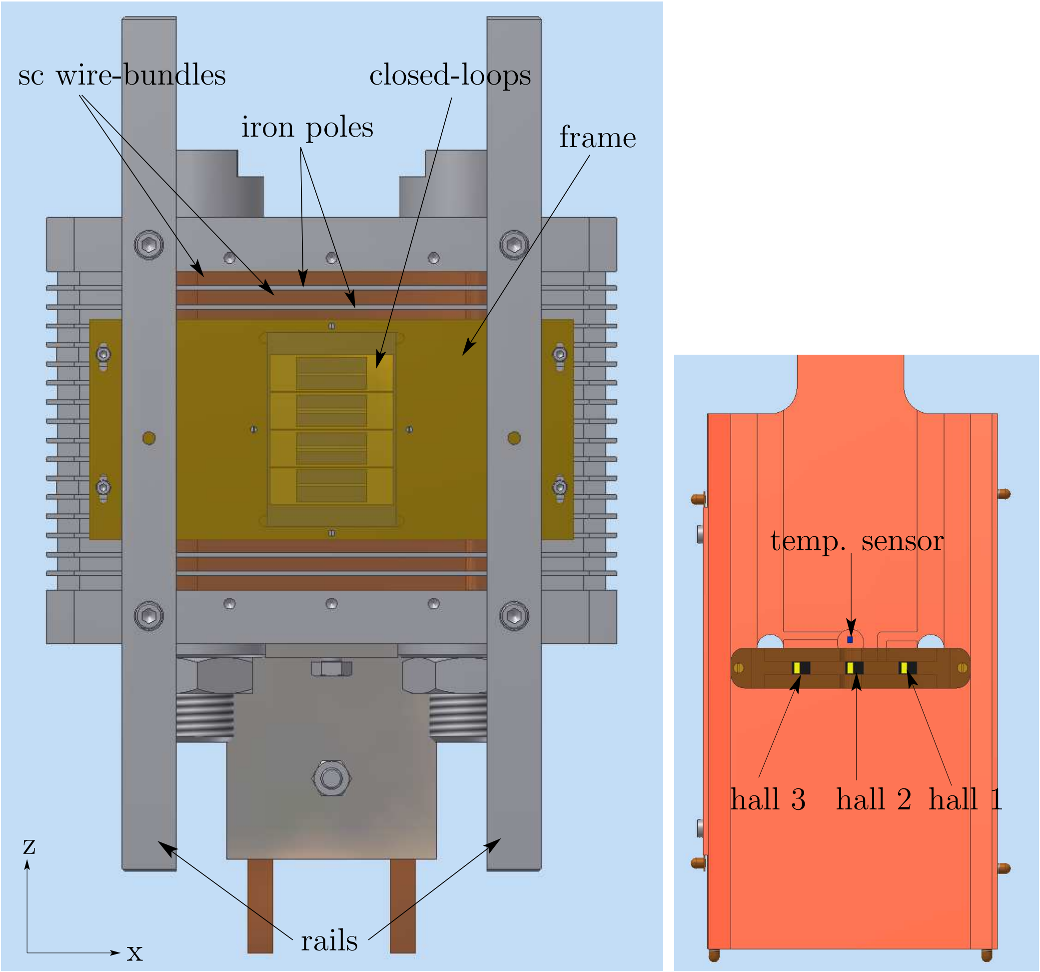

Fig. 8.3: Measurement setup with mock-up coil, frame, close-loop system, rails and hall probe slide.

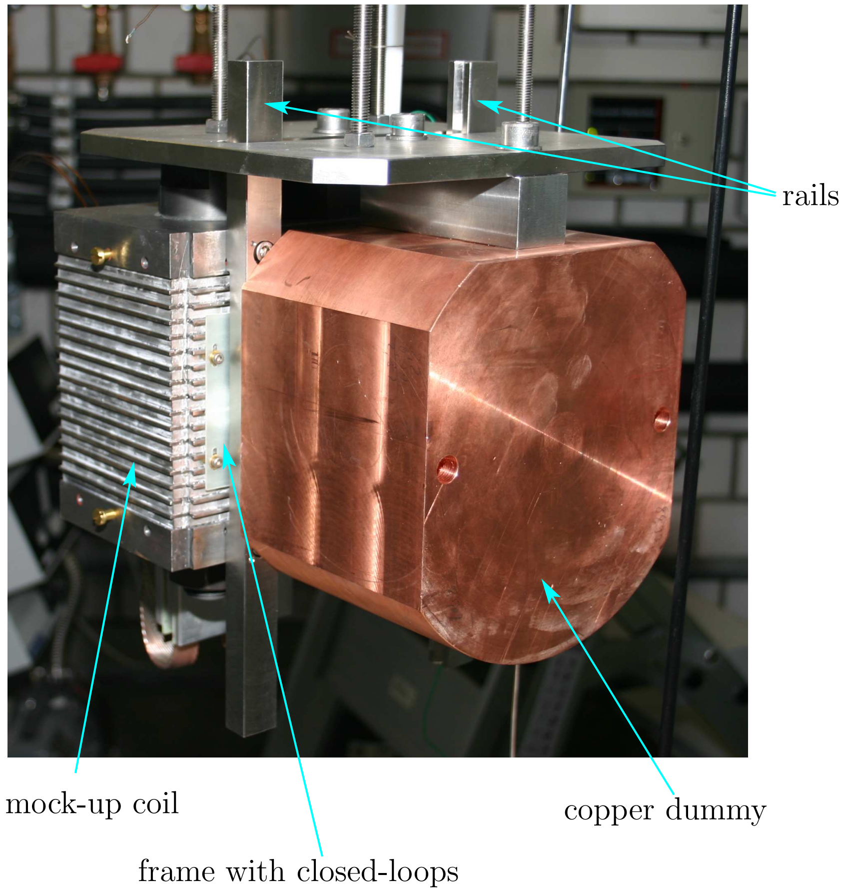

Fig. 8.4: Photograph of the experimental setup before installation in the cryostat with the mock-up coil (left), the frame with the induction-shimming system, the rails and the copper dummy (right).

The measurements were performed in the bath cryostat CASPER [MGS$^+$08] in liquid Helium at 4.2 K. To balance the weight of the mock-up, a copper dummy was attached (see figure 8.4). The magnetic field was measured with three hall probes mounted on a brass-slide (see figure 8.3). The distances in x-direction between the hall probe mounted in the center of the slide (hall 2) and the outer hall probes are 20 mm. The design distance between the mock-up coil surface and the hall probes was 7.5 mm (y-direction). A comparison of the fourth maximum and minimum of the measured field amplitude at 250 A and 350 A in the mock-up coil with a simulated coil in RADIA [ECC97, CEC97] gave an effective distance of 8.15 ± 0.1 mm. The mid-plane of the induction-shimming system was 7.15 ± 0.1 mm away from the plane of the hall probes (y-direction).
The slide with the hall probes is guided by two stainless steel rails. The slide was fixed with a rod to a stepper motor outside the cryostat and moved along the z-axis (beam direction). The z-position of the slide was measured with a linear-encoder at room temperature. The maximal coverable distance for the movement of the slide along the beam direction (z-axis) was 169 mm. A photograph of the setup is shown in figure 8.4.

measurement campaign	offset hall 1	offset hall 2	offset hall 3
1	1.9 mT	2.3 mT	6.6 mT
2	1.9 mT	2.3 mT	6.6 mT

Tab. 8.1: Field offsets caused by the hall probes.

Using only one undulator coil and measuring the field in a distance of about 8.15 ± 0.1 mm leads to small field values at the hall probes and therefore increases the errors induced by the measurement equipment.

The measurements were performed in two steps: the mock-up coil together with the induction-shimming system and the mock-up coil alone. During each measurement campaign the current in the mock-up coil was increased from zero to 250 A. An additional measurement at 350 A without induction-shimming system was performed. In each measurement the Hall probes were moved with a step width of 0.1 mm.

With the present measuring system the following parameters cannot be controlled:

- The distance between the mock-up coil and the Hall probes might vary by a small amount along z due to a backlash between the rails and the slide.
- The offsets of the hall probes might change during the measurement campaigns (three days each).
- Due to longitudinal field components (only one undulator coil is used) a planar Hall effect might contribute to the measurements.
- The position of the Hall probes is changed by a rod, which is partly in liquid Helium, partly outside. Moving the rod changes the length of the *cold* and the *warm* part of the rod and adds a small systematic error to the measurement.

The error was assumed to be about 10 mT.

8.2 Results and Interpretation

Figure 8.5 shows a field plot of the raw measurement data obtained at 350 A in the mock-up coil without the induction shimming system. The first and the last extremum of the undulator (red arrows) are significantly higher. This is caused by the magnetization of the iron blocks at the beginning and end of the undulator. In the following plots the first and the last extremum, i.e. the first and the last 25 mm of the magnetic field are not shown.

In figure 8.6 the raw data of the field measurements at zero current in the mock-up coil with and without the YBCO loops are shown. Both measurements between 0 and 119 mm show offsets of the hall probes. The offsets are listed in table 8.1. All field measurements are corrected for these offsets.

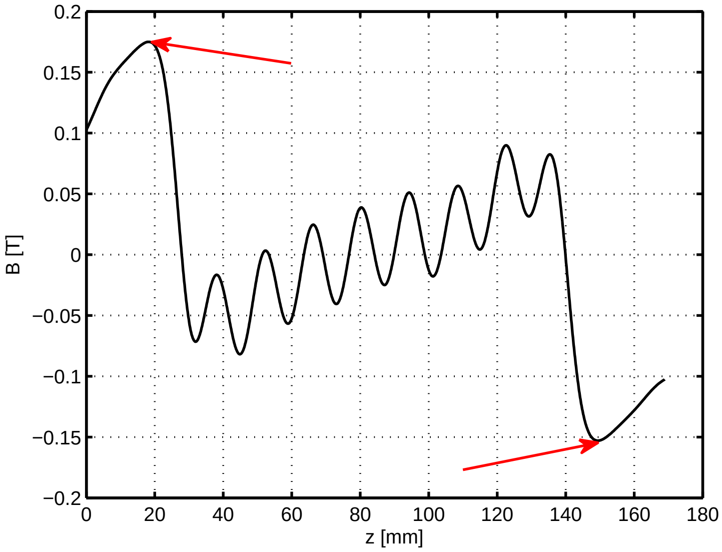

Fig. 8.5: Magnetic field from raw data at 350 A in the mock-up coil. The read arrows mark the first and the last extremum of the field, which are significantly higher. This is due to the magnetization of the iron blocks at the beginning and the end of the undulator.

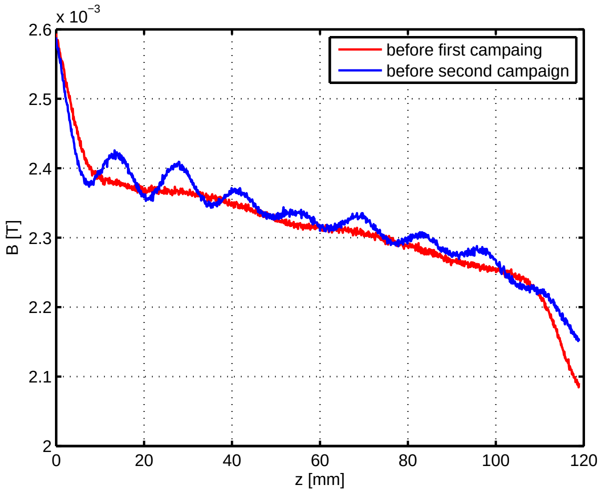

Fig. 8.6: Raw data of the field measurements at zero current (Hall probe 2) in the mock-up coil before the measurement with the shimming equipment (red) and without (blue).

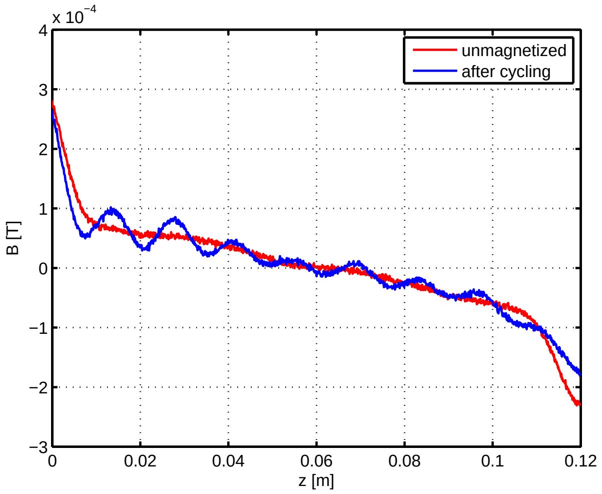

Fig. 8.7: Magnetization of the mock-up coil at the beginning of the measurement with the shimming equipment (red) and without (blue).

Figure 8.7 shows the magnetization of the mock-up coil without current at the beginning of the two measurement campaigns (with and without shimming). In both the remanent field is smaller than 0.1 μT. After measuring with the shimming device this was achieved by reversing the polarity of the mock-up coil twice with currents up to 25 A.

In the following, the results of the measurement are discussed for a current of 70 A, i.e. a current density of 140 A/mm^2, in the mock-up coil. With this current the induction-shimming system still operates below the critical current density j_c in the YBCO structures even in the first loop, where the thin bar has a reduced width.

8.2.1 Field correction at 70A

The left part of figure 8.8 shows a comparison of the field measurements with (black) and without (red) the induction-shimming system. The closed-loop system starts at the zero crossing between second maximum and third minimum ($z \approx 30$ mm) and ends at the zero crossing between the 6th maximum and the 7th minimum ($z \approx 86$ mm).

The field without the closed-loops shows a partly antisymmetric behaviour, i.e. the field maxima increase and the minima decrease linearly with z. This is due to finite length field effects and missing matching sections at the beginning and end of the mock-up coil. The 6th maximum and the 6th minimum do not follow the described behaviour, but are reduced by about 5 mT compared to the above mentioned linear description. The seventh minimum shows a deviation of about 3 mT. These field deviations are caused by pole errors.

With induction-shimming, the inner part of the field is flattened. The relative variation of the inner maxima (3th - 5th) is reduced from $\sim 23.6\,\%$ to $\sim 4.8\,\%$. The variation of the inner minima (4th - 6th) is reduced from $\sim 19.2\,\%$ to $\sim 9.81\,\%$. The 6th maximum and the third minimum were excluded in these comparisons, because

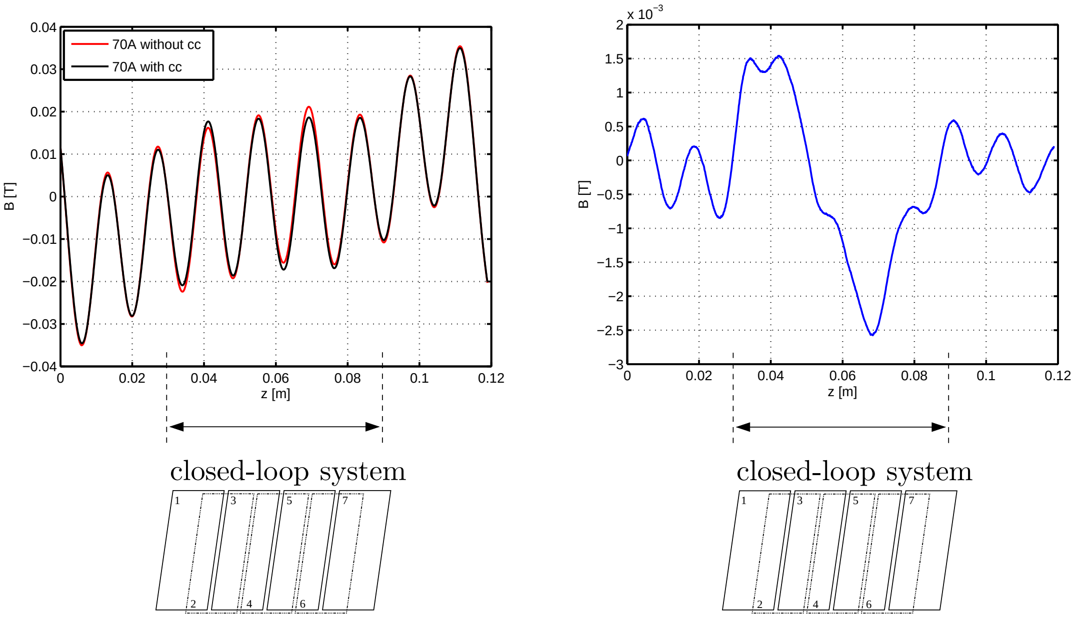

Fig. 8.8: Comparison of corrected and uncorrected field (left) and correction field created by the closed-loop system (right) - current in main coil: 70 A. The closed-loop system is installed between $z = 30\,\mathrm{mm}$ and $z = 86\,\mathrm{mm}$.

they are covered by only one closed-loop. Therefore, the correction efficiency is reduced compared to the extrema covered by two overlapping closed-loops. However, the correction field produced by the closed-loops at the third extremum is about 1.7 mT, i.e. about 8 % of the undulator field.

The whole correction field is shown in the right plot of figure 8.8. As expected from the antisymmetric field behaviour of the mock-up field, the correction is highest at the begin and end of the induction-shimming system. The sinusoidal behaviour for $z < 30\,\mathrm{mm}$ and $z > 86\,\mathrm{mm}$ is most probably caused by different magnetizations in the iron blocks for the two measurements [MD04]. The maximum of the correction field is $B_{cc} = 2.35\,\mathrm{mT}$ at $z = 68.5\,\mathrm{mm}$. This reduces the 5th maximum by 11 %.
The induced currents were estimated by a fit of a Biot-Savart model with seven overlapping closed-loops with the same dimensions as the test-device shown in figure 8.1. The comparison of fit and measurement is shown in figure 8.9.

Current in mock-up coil	Induced currents in closed-loop [A]						
	1	2	3	4	5	6	7
70 A	56	-2.0	61	-51.5	13.5	-86	-23

Tab. 8.2: Induced currents in the closed-loops of the induction shimming system for 70 A in the main coil, received from a correction field fit with a Biot-Savart model. The uncertainty is approximately ±10 %.

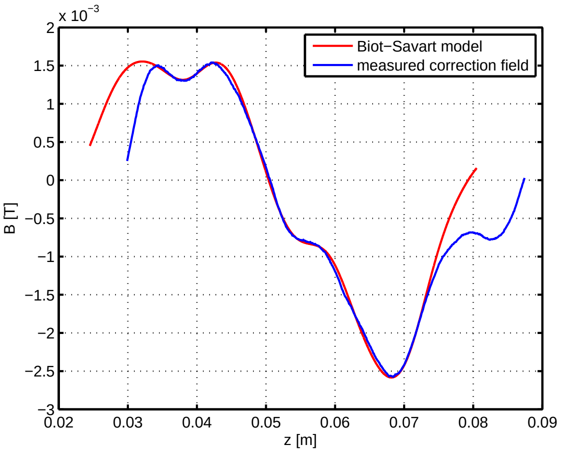

Fig. 8.9: Fit of 7 closed-loop Biot-Savart model to correction field - current in main coil: 70A

The values of the induced-currents at 70 A in the mock-up coil are given in table 8.2. An overview of the induced currents for different main coil currents is given in table 8.5. The modelled and the measured field are in good agreement for 35 mm $< z <$ 73 mm. The differences outside this area ($z <$ 35 mm and $z >$ 73 mm) are presumably caused by the fact that the Biot-Savart model does not take the magnetization of the iron into account. Therefore the uncertainty in the current is about ±10 %. The distance between the mid plane of the closed-loops and the hall probes was determined by comparing the measured field values with a RADIA [ECC97, CEC97] simulation to 7.15 ± 0.1 mm. This results in an additional uncertainty for the induced currents of ±1.5 %.

The phase differences between electron and photon for the corrected and uncorrected fields are compared in figure 8.10. The phase differences are calculated over the four periods covered by the closed-loop system.

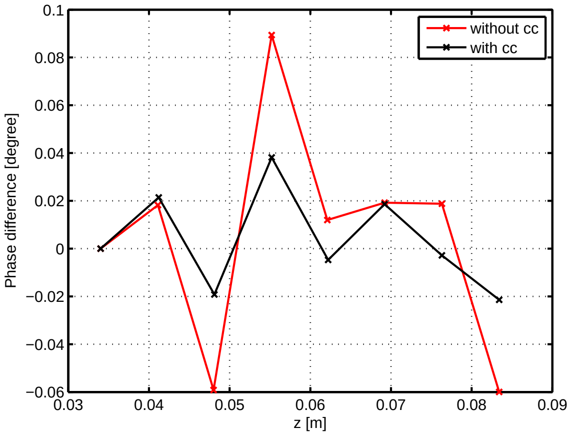

Fig. 8.10: Phase differences between electron and photon at 70 A with and without correction coils (cc)

It can be seen that the changes of the phase differences for each half-period follow in both cases the same pattern. The absolute values for the corrected case are smaller than for the uncorrected case, except for the first half period.

As presented in the theory of induction-shimming, the field correction is directly connected to a correction of the field integrals. Figure 8.11 shows a comparison of the first and the second field integrals with and without induction-shimming. The integrals were calculated for the four periods covered by the closed loops.
The first field integrals are oscillating in the corrected and uncorrected case with an amplitude of $\approx 8 \cdot 10^{-5}$ Tm and show a parabolically shaped offset depending on z. The closed-loops reduce this offset significantly. The final value of the first field integral at the end of the four periods is reduced by one order of magnitude from $1.95 \cdot 10^{-5}$ Tm to $-1.5 \cdot 10^{-6}$ Tm.

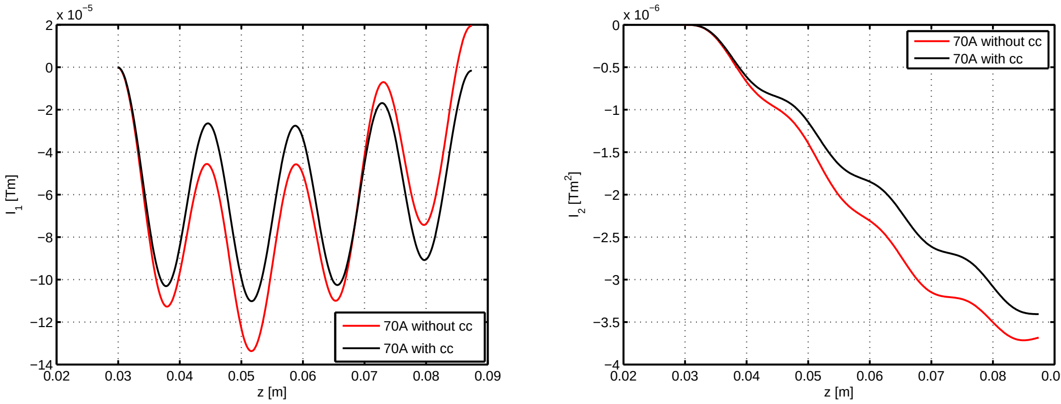

Fig. 8.11: Comparison of first (left) and second field integral (right) with and without closed-loops at 70 A in the mock-up coil.

The absolute second field integrals increase linearly with z. In the corrected case the slope is slightly flatter than in the uncorrected case. This leads to a change of

Current in mock-up coil	Variation of minima without	Variation of minima with	Variation of maxima without	Variation of maxima with
30 A	17.0 %	7.8 %	19.0 %	3.2 %
50 A	16.7 %	8.7 %	21.0 %	3.4 %
70 A	19.2 %	9.1 %	23.6 %	4.8 %
100 A	22.3 %	11.3 %	28.1 %	7.8 %
150 A	29.0 %	15.5 %	35.0 %	11.4 %
200 A	36.5 %	19.0 %	41.0 %	15.0 %
250 A	42.8 %	23.0 %	46.4 %	18.6 %

Tab. 8.3: Relative variation of minima (4th - 6th) and maxima (3th - 5th) without and with closed-loops.

the final value of the second field integral from $-3.7 \cdot 10^{-6}\,\mathrm{Tm}^2$ to $-3.4 \cdot 10^{-6}\,\mathrm{Tm}^2$, which is an reduction of about 9 %.

The strong reduction of the first field integral combined with a slight reduction of the second field integral are in good agreement with the results of the simulations of the three period induction-shimming system presented earlier.

8.2.2 Reduction of the correction efficiency at the critical current

In the following the behaviour of the induction-shimming system for currents above $I_{main} = 70\,\mathrm{A}$ in the mock-up coil is discussed.

Figure 8.12 shows the measured corrected fields for different currents in the main coil, and the uncorrected field at $I_{main} = 250\,\mathrm{A}$. With increasing current I_{main}, the field pattern for $30\,\mathrm{mm} < z < 86\,\mathrm{mm}$ converges more and more to the uncorrected field. As shown in tables 8.3 and 8.4, the variation of the minima and maxima increases. Up to $I_{main} = 250\,\mathrm{A}$ the corrected fields are still flatter than the uncorrected fields but the increasing antisymmetric behaviour of the corrected fields is obvious.

This is caused by the first closed-loop reaching the critical current density. Due to the coupling between the loops the magnetic flux and, therefore, the correction currents in the loop system are redistributed. Figure 8.13 shows a comparison of the correction fields created by the closed-loop system at different operation currents in the mock-up coil. In the upper plot of figure 8.13 the absolute correction fields are compared. In the lower plot the fields are normalized in respect to the minimum of the correction fields at $z \approx 70\,\mathrm{mm}$. For currents above $I_{main} = 70\,\mathrm{A}$ the double peak between $z = 30\,\mathrm{mm}$ and $z = 50\,\mathrm{mm}$ changes to a broad single peak with a maximum at $z = 40\,\mathrm{mm}$ by reaching the critical current in the first loop at $I_{main} \approx 70\,\mathrm{A}$. This is caused by a redistribution of the correcting magnetic flux between the first three closed-loops (see table 8.5). The current in the first loop stays around 60 A for currents higher than $I_{main} = 70\,\mathrm{A}$ in the main coil. The current in the second loop increases from $-2.0\,\mathrm{A}$ at $I_{main} = 70\,\mathrm{A}$ rapidly to 34 A at $I_{main} = 100\,\mathrm{A}$ and further to 150 A at $I_{main} = 250\,\mathrm{A}$. Between $I_{main} = 70\,\mathrm{A}$ and $I_{main} = 100\,\mathrm{A}$ the induced current in the third loop decreases from 61 A to 49.5 A. Above $I_{main} = 100\,\mathrm{A}$ the correction current in this loop increases again. The coupling between the loops even

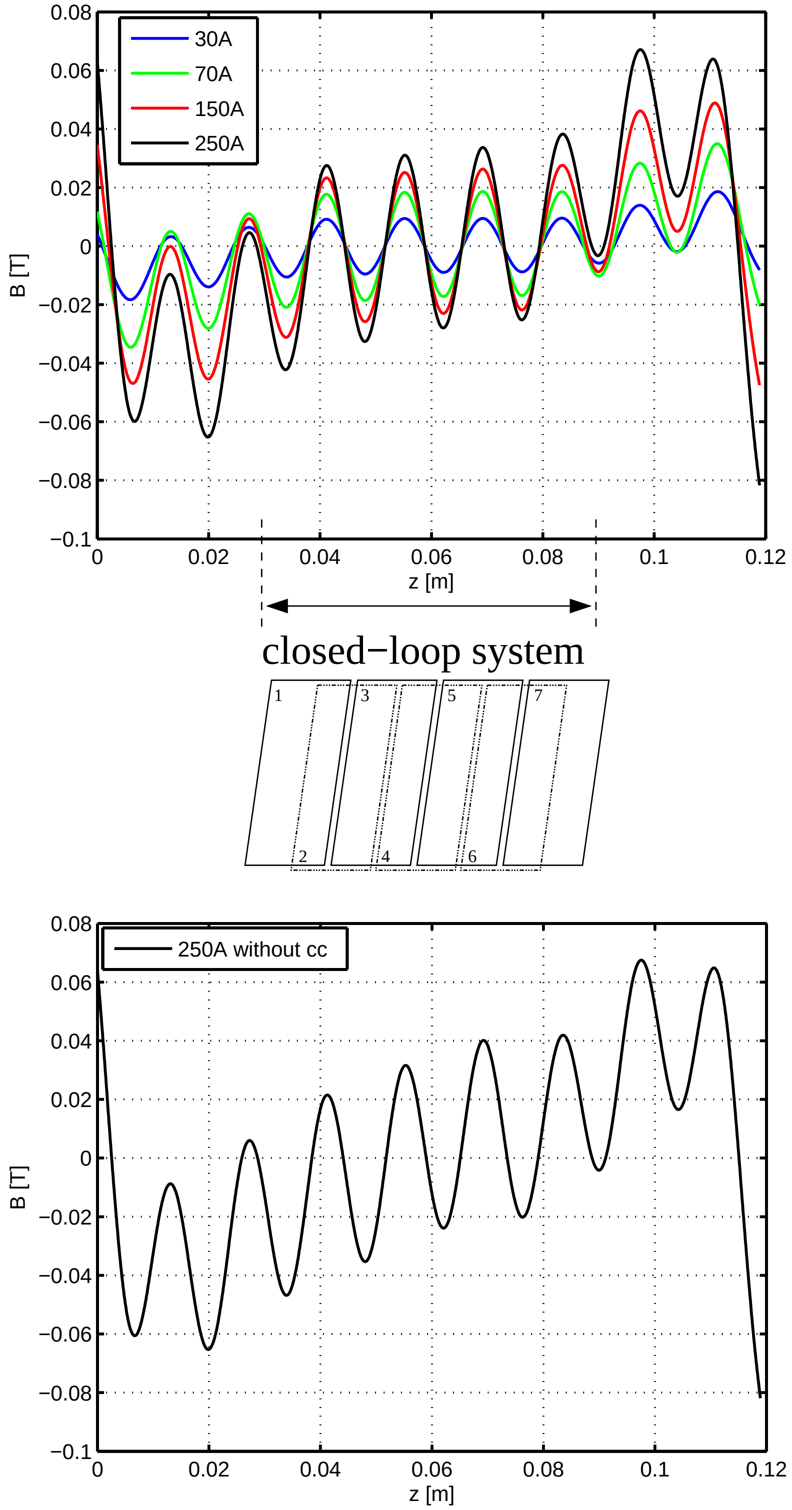

Fig. 8.12: Comparison of corrected fields for different currents in the mock-up coil (top) and uncorrected field at 250 A (bottom).

Current in mock-up coil	Variation 4th/5th minimum	Variation 4th/5th maximum
30 A without	1.39 mT → 14.0 %	0.81 mT → 7.6 %
30 A with	0.55 mT → 6.1 %	0.03 mT → 0.3 %
50 A without	2.5 mT → 16.0 %	1.4 mT → 8.3 %
50 A with	1 mT → 6.7 %	0.1 mT → 0.7 %
70 A without	3.7 mT → 19.2 %	2.05 mT → 9.7 %
70 A with	1.4 mT → 7.5 %	0.23 mT → 1.2 %
100 A without	5.03 mT → 22.3 %	3.05 mT → 12.1 %
100 A with	1.95 mT → 8.9 %	0.55 mT → 2.5 %
150 A without	7.3 mT → 27.0 %	4.8 mT → 15.6 %
150 A with	2.8 mT → 10.8 %	1.15 mT → 4.4 %
200 A without	9.35 mT → 29.8 %	6.7 mT → 18.8 %
200 A with	3.7 mT → 12.7 %	1.9 mT → 6.3 %
250 A without	11.4 mT → 32.3 %	8.5 mT → 21.2 %
250 A with	4.7 mT → 14.4 %	2.75 mT → 8.1 %

Tab. 8.4: Relative variation between 4th and 5th minimum and 4th and 5th maximum without and with closed-loops.

causes a change in the behaviour of loop four and five, where the induced currents drop between $I_{main} = 70\,\mathrm{A}$ and $I_{main} = 100\,\mathrm{A}$.
Above $I_{main} = 150\,\mathrm{A}$ the shoulder at $z = 86\,\mathrm{mm}$ of the correction field increases compared to the minimum. This is probably caused by loop six, which reaches the critical current density and alters the correction current in loop seven. This behaviour is not completely understood, because there are no measurements between $I_{main} = 150\,\mathrm{A}$ and $I_{main} = 200\,\mathrm{A}$ and $I_{main} = 200\,\mathrm{A}$ and $I_{main} = 250\,\mathrm{A}$, which could confirm this interpretation. If this interpretation is correct, the critical current of the closed-loops is about 160 A±10 %. This can be converted to a critical current density of about $485\,\mathrm{kA/mm^2} \pm 10\,\%$. Comparable current densities have been published for thin layers of YBCO, measured at 4.2 k already in the beginning 1990's by [RSSI90]. Unfortunately the reduction of the first loop's cross-section, due to the mask error, is not exactly known and, therefore, its critical current cannot be used to verify the previous estimation. This should be subject of future experiments.

The correction efficiency is also shown in figure 8.14 for the different currents through the undulator. The ratio of adjacent extrema covered by the loop j are compared:

$$\Delta_j = \left| 1 - \left| \frac{A_{j,max}}{A_{j,min}} \right| \right| . \tag{8.1}$$

The efficiency is lowest at the first loop, which suffers from a fabrication error in the YBCO layer. The dashed curves show the ratio before compensation, the solid lines after compensation. The values of the solid lines increase towards both ends of the area covered with YBCO loops especially for currents above $I_{main} = 150\,\mathrm{A}$. This is caused by two effects:

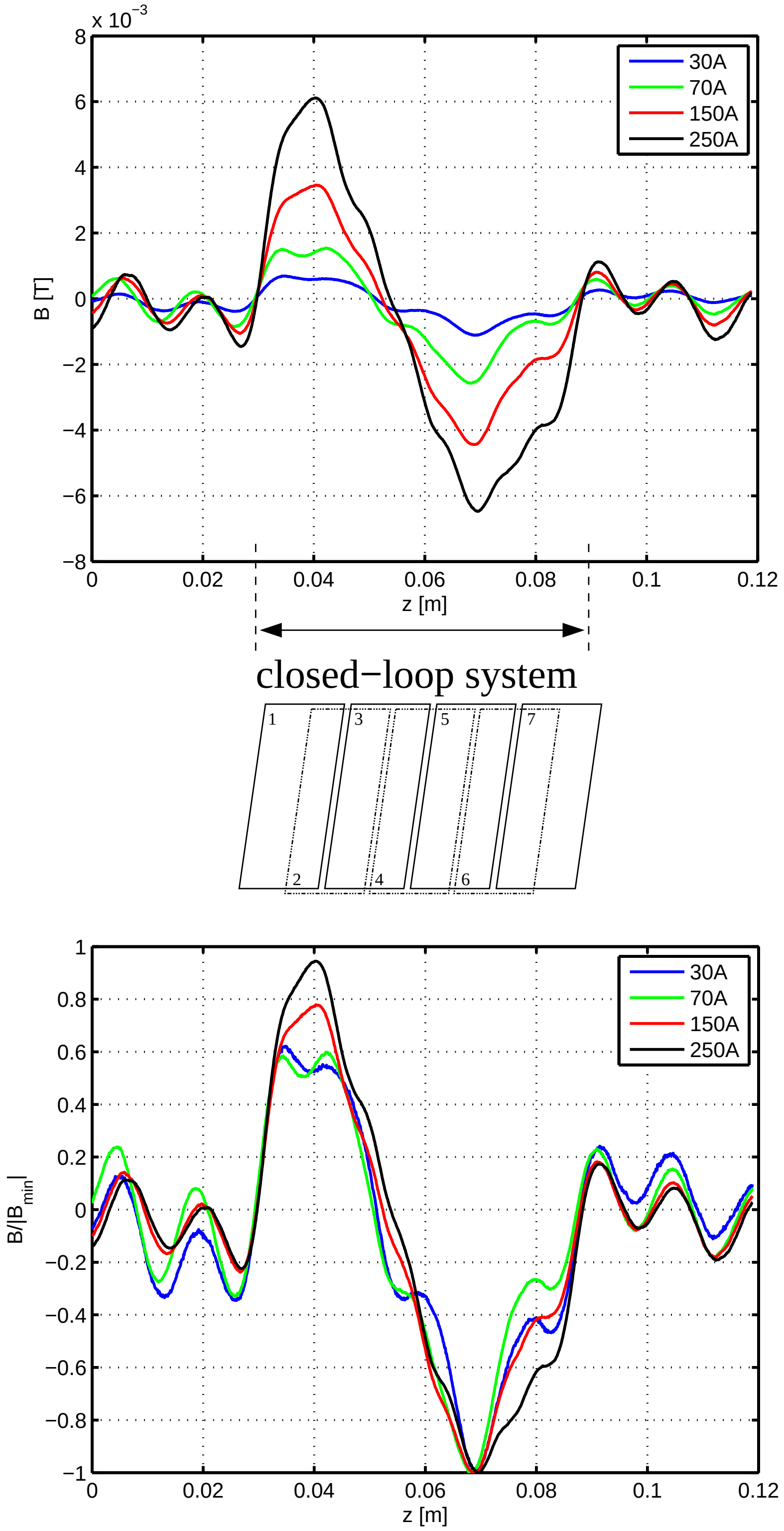

Fig. 8.13: Comparison of the correction fields for different currents in the mock-up coil. The absolute fields (top) and the correction fields, each normalized with respect to its minimum (bottom) are shown.

Current in mock-up coil	Induced currents in closed-loop [A] 1	2	3	4	5	6	7
30 A	22.8	1.3	21.5	-25.8	8.4	-39.5	-7
50 A	43	-1.0	47	-39	15.7	-63.2	-13
70 A	56	-2.0	61	-51.5	13.5	-86	-23
100 A	45	34	49.5	-29	-10	-92.5	-46
150 A	54	67	66.5	-20.5	-23	-111	-76
200 A	62	102	81	-20.7	-40	-119.5	-110.5
250 A	60	150	75	-25.8	-50	-160	-110
0 A after 250 A	-3	-4.5	-6.7	6.3	-3.5	14.3	4.5

Tab. 8.5: Induced currents in the closed-loops of the induction shimming system, received from a correction field fit with a Biot-Savart model. The error is approximately ±10 %.

1) The induced currents reach the saturation current, in the right loops for $150\,\mathrm{A} \leq I_{main} \leq 250\,\mathrm{A}$ (see table 8.5) and in the first loop at the left-hand side at $I_{main} \gtrsim 70\,\mathrm{A}$ due to a fabrication error. This is the cause for the higher values at point 1 at the left hand side of figure 8.14.
2) At both ends of the loop system the values in figure 8.14 are higher since the outmost loops have no partner due to the finite length of the induction-shimming system (see figure 8.2 and 8.1).
The third loop covers the center of the uncorrected antisymmetric mock-up field. Therefore, all curves in figure 8.14 have their minimum at $j = 3$.

Figure 8.15 shows the comparison of the phase differences between electron and photon for different currents above $I_{main} = 70\,\mathrm{A}$ in the mock-up coil with and without induction-shimming. It can be stated, that for all currents the phase differences with induction-shimming are reduced significantly.

8.2.3 Hysteretic behaviour of the closed loop system at high fields

Figure 8.16 shows the remaining field at zero current in the mock-up coil after operating the mock-up at $I_{main} = 250\,\mathrm{A}$ with the induction-shimming system. The field for $z < 30\,\mathrm{mm}$ and $z > 86\,\mathrm{mm}$ is the remanent field of the magnetized iron of the mock-up. Using the Biot-Savart model of seven closed-loops, the remaining loop currents were estimated. The comparison of the modelled and measured fields are shown in figure 8.17. The induced currents are summarized in table 8.5. In figure 8.18 the remaining field was inverted and normalized to its minimum and added to the curve with the normalized correction fields 8.13. The remaining field has the same shape as the correction fields. This means, that the induction-shimming system shows hysteretic behaviour, if a certain correction flux is exceeded. Due to the small remaining currents in the loops, it can be estimated that this level was reached between $I_{main} = 200\,\mathrm{A}$ and $I_{main} = 250\,\mathrm{A}$.
This result supports the previous interpretation of the change in the shape of the correction field: the current reached its critical value in loop six around 160 A, i.e.

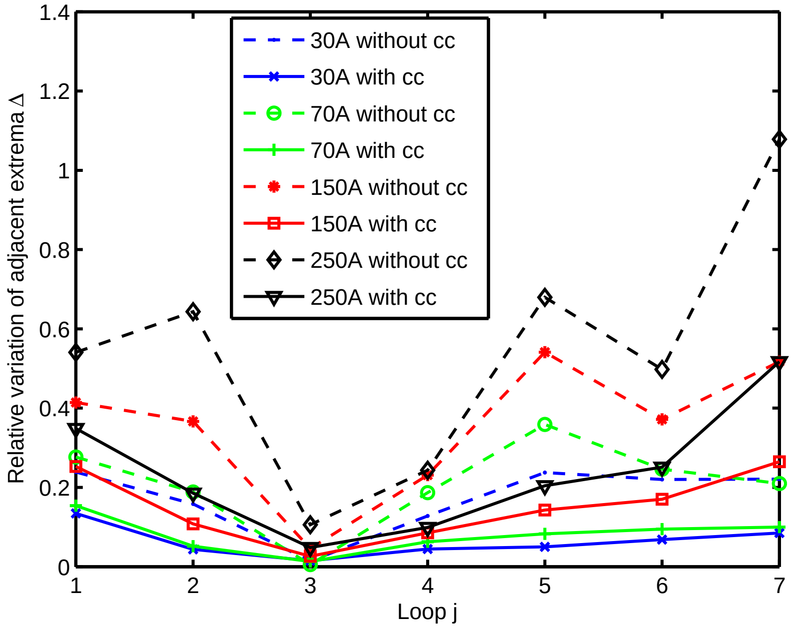

Fig. 8.14: Ratio of the absolute values of adjacent extrema with and without the YBCO loop system for the different currents I_{main} of table 8.5. The values at the beginning and the end are higher due to the finite length of the induction-shimming system.

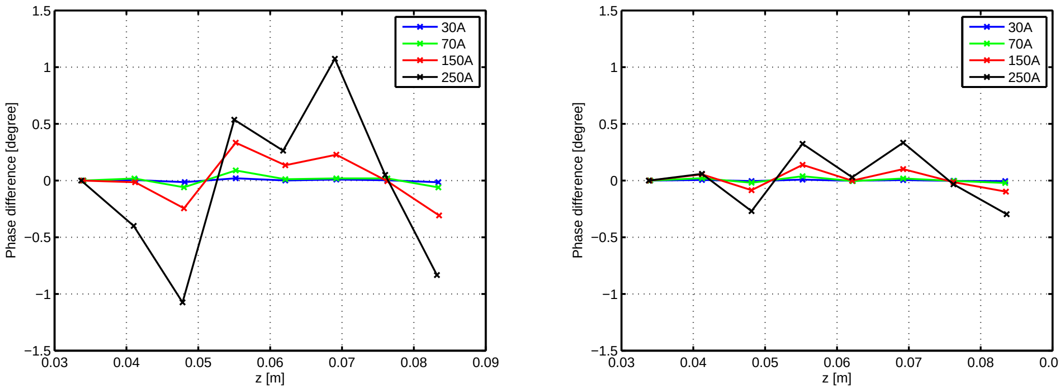

Fig. 8.15: Comparison the phase differences between electron and photon at different mock-up coil currents: without closed-loops (left) and with closed-loops (right).

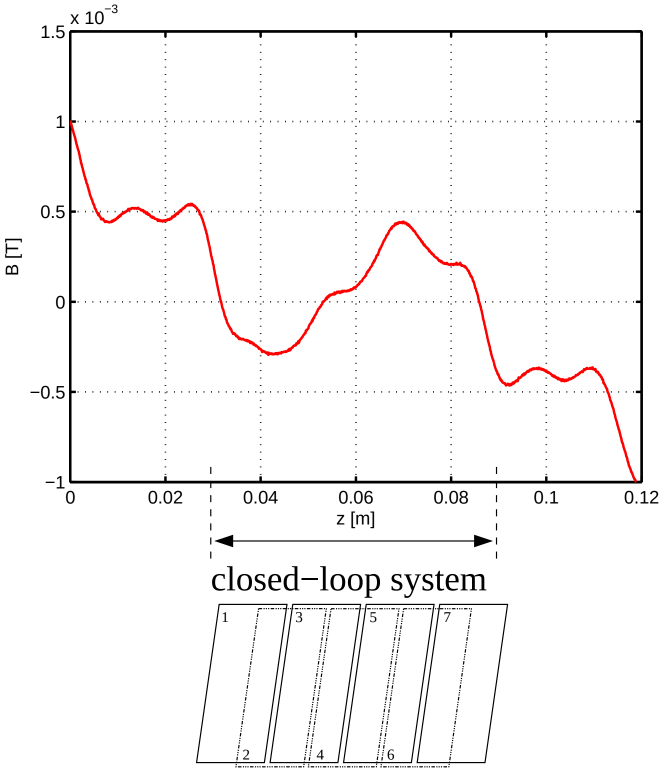

Fig. 8.16: Remaining field in the closed-loop after 250A.

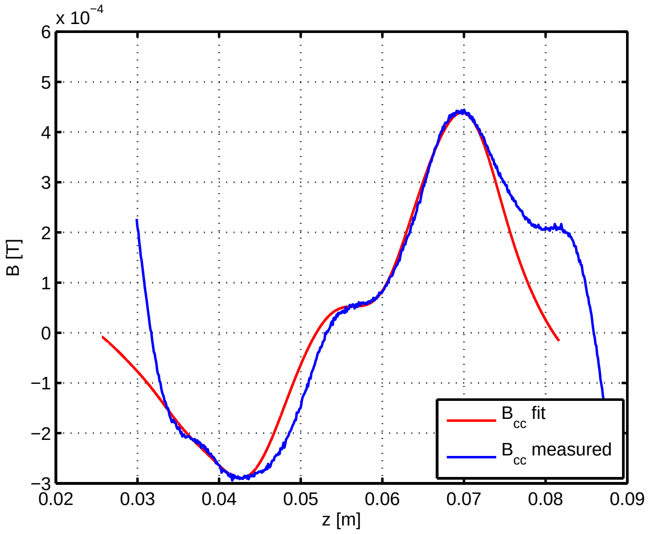

Fig. 8.17: Comparison of the measured remaining field in the closed-loop after 250A with the field from the fitted Biots-Savart model.

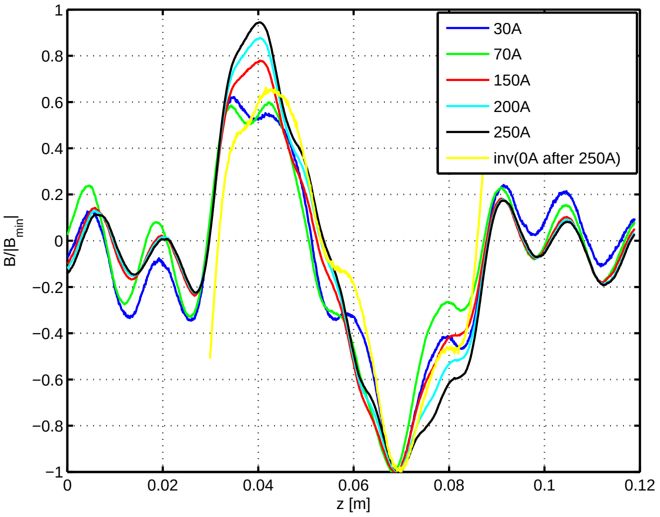

Fig. 8.18: Comparison correction fields with the inverted remaining correction field after 250A - each normalized with respect to its minimum (center Hall probe)

at $I_{main} \approx 250\,\mathrm{A}$.

Although the relative reduction of the variation of the field extrema is not reduced significantly when single loops of an induction-shimming system reach their critical current, this leads to an hysteretic behaviour of the complete system. For the applicability of induction-shimming in superconductive undulators, the high temperature superconductor and the smallest cross-sections of the loops must be chosen such, that the currents in all closed-loops stay well below the critical current for any available current in the undulator main coils.

8.3 Induction-shimming: Outlook

Induction-shimming is a novel passive correction scheme for field errors in superconductive undulators. In this thesis both the theoretical explanation and an experiment with a system of seven overlapping closed-loops are described. This first experiment showed that this correction scheme has a high potential for field error correction and has proven to be robust. Although the critical current was limited in one closed-loop due to a manufacturing error, the correction fields reached about 10 % of the mock-up field. Classical shimming techniques for superconductive undulators are designed to correct field errors not bigger than 1 % of the main field.
The maximum induced current in the closed-loops was about 160 A ± 10 % with an estimated maximum current density of $485\,\mathrm{kA/mm^2} \pm 10\,\%$. This is close to the critical current density of $500\,\mathrm{kA/mm^2}$ given in [RSSI90] for YBCO thin layer structures at 4.2 K. However, the estimated critical current density should be proven in a future experiment and identified with higher precision.
The maximum measured correction field of the loop system was about $B_{cc} \approx 6\,\mathrm{mT}$ at a distance of $7.15 \pm 0.1\,\mathrm{mm}$. Future undulators will have a gap width of $g = 5\,\mathrm{mm}$

and roughly a field amplitude of $\tilde{B} \approx 1.5\,\mathrm{T}$. Correction schemes are designed to correct at maximum field errors of 1 % of the main field, i.e. about $\approx 15\,\mathrm{mT}$. The distance between the beam axis and the midplane of the induction-shimming system will be about $g/2 = 2.5\,\mathrm{mm}$. Due to Biot-Savart's law the field behaves inversely proportional to the distance: $B \sim \frac{1}{r}$. Therefore, the correction field at a distance of 2.5 mm is $B_{cc,1} \approx 17\,\mathrm{mT}$. One induction-shimming system will be installed at each undulator coil, the maximum correction field on the beam axis becomes then $B_{cc,2} \approx 34\,\mathrm{mT}$. This is already more than 2 % of the amplitude of the undulator field. Therefore, the induction-shimming test device fulfills the requirement.

A major issue for the applicability of induction-shimming is the reduction of the thickness of the substrate on which the YBCO layer is coated. The substrate used for this experiment had a thickness of $500\,\mu$m. Thus, the complete device had a thickness of 1 mm. Mounting such a system on both coils would either reduce the beam stay clear by about 2 mm or require an increase of the magnetic gap, which would reduce the magnetic field on axis. Therefore, the thickness of the structure has to be reduced to an acceptable level. This can be achieved by using thinner substrates and by structuring both sides of the substrate. With a substrate thickness of $250\,\mu$m the gap would be increased only by 0.5 mm comparable with active in-gap shimming concepts.

Another possibility would be to create HTSC structures on the stainless steel liner, which will separate the superconductive coils from the beam in the future SCU15 for ANKA, which is now under construction. This would totally avoid an additional increase of the magnetic gap.

In the near future it is planned to integrate the loops in a 15 period SCU15 mock-up and to discuss afterwards the integration of an induction shimming concept in a full length 100 period undulator. There is no fundamental obstacle against scaling to full undulator dimensions. If the system has to be assembled from shorter overlapping closed-loop systems, their alignment is an important issue.

9. CONCLUSION

In this thesis a novel concept for reducing phase errors in superconductive undulators is described. Undulators in synchrotron light sources emit a line spectrum in the X-ray regime. The line width is determined mainly by the beam quality (emittance and energy spread of the electron beam) and the quality of the magnetic field. Small mechanical deviations from the design values and field distortions from period to period can reduce the brilliance of the radiation and therefore have to be corrected.

A measure for the global effect of distributed local field errors in the undulator is the so-called phase error. A negligible small phase error means that the oscillating electron and the emitted light are always in phase along the trajectory in the undulator. Phase errors are caused by variations of the field strength and the period length from period to period.

These variations in superconductive undulators are basically due to mechanical deviations in the undulator coils. The effect of the different possible types of mechanical inaccuracies - pole and wire bundle displacement with respect to the beam axis and variation of the period length - was analyzed. It was shown that the different field error contributions depend differently on the operation current of the undulator, due to the saturation behaviour of the iron poles. By an analyses of the measured field of the SCU14 installed at ANKA it was shown that it is possible to distinguish field errors caused by a displacement of poles and wire bundles.

The phase error of an undulator is determined not only by the amplitude of local field errors but also strongly depends on their distribution over the length of the device. In this work, the effect of statistically and systematically distributed mechanical errors on the phase error of superconductive undulators was examined using a sine wave model. For statistical error distributions the variation of the period length was identified as the dominating contribution while the wire bundle variations have the smallest effect on the phase error. In contrast, for systematic error distributions the phase error is dominated by displacements of the wire bundles. For systematic errors the effects of neighbouring wire bundle on the extremum add up. In contrast to that for statistically distributed deviations there is a high probability that the effects of neighbouring wire bundles cancel. It was shown that the phase error due to systematic deviations is the smaller the shorter the correlation lengths of the deformations are.

For the correction of field errors in superconductive undulators several schemes exist: mechanical shimming, shimming with integral correctors and active shimming with local correction coils. These classical concepts were discussed with respect to their advantages, disadvantages and limitations. A procedure for mechanical shimming of superconductive undulators was described. Shimming with integral

correctors gives promissing results for the SCU14 installed at ANKA.
The field of a single pole can in general only be changed by a current through superconducting wires which are placed close to the pole. As the distance between wire and beam axis increase the field changes distribute over several poles when the material between the poles is magnetic. Using non-magnetic material between the poles (the so-called laminated undulator), for instance copper, the correcting wires can be further away, for instance at the side of the undulator (lateral shim coils).
Nevertheless, shimming with actively powered coils is time consuming since the undulator has to be cooled down several times for measurements. In addition, the shim currents might be different for different undulator currents.

These complications stimulated the idea to think about a passive self-adaptive shimming system which only depends on the field error and not on its source. Such a novel passive shimming concept based on superconductive closed-loops - induction shimming - was proposed in this thesis. In this method HTSC closed loops are positioned on the surface of the undulator. The width of these loops is one or several period lengths long in beam direction. In case of an ideal undulator the integral flux is zero. With deviations from the ideal undulator (one pole has a different field than the other) currents are induced in the loop which compensate automatically the error.
The theory of induction shimming was derived from Faraday's law of induction and simulations with a Biot-Savart model showed that phase errors can be reduced significantly by this method. It was also shown, that the correction efficiency is quite robust against lateral and angular misalignment of the closed-loop system.
The theoretical concept of induction-shimming was published in Physical Review Special Topics - Accelerators and Beams [WBP$^+$08b] and a manuscript with the experimental results was just submitted to the same journal [WBP$^+$08a]. A patent for this novel shimming method is pending [WBR08].
In recently performed proof of principle experiments with a system of seven closed loops made from 330 nm thick YBCO layers the concept of induction shimming was successfully demonstrated. The system reduced the variation of the field extrema, the first field integral, the second field integral and the phase difference between electron and photon for the four periods covered by the closed-loops significantly. The critical current density reached in the test device was in good agreement with the critical current densities published in literature for thin YBCO films at 4.2 K. The measured currents in the loops are high enough to shim a real undulator with a field error of up to 1 %. The next step is install a complete induction shimming system in a SCU15 mock-up undulator with a length of 15 periods, now under construction.

Acknowledgements

The author thanks Prof. Dr.rer.nat. T. Baumbach from the Laboratory for Applications of Synchrotron Radiation (LAS) and Prof. Dr.rer.nat G. Quast from the Institute of Experimental Nuclear Physics at the University of Karlsruhe (TH) for support and advice.

The author also wants to thank PD Dr. R. Rossmanith from the Institute for Synchrotron Radiation (ISS) at Forschungszentrum Karlsruhe and Dr. A. Bernhard (LAS) for the close collaboration, fruitful discussions, critical comments, openness for new ideas, scientific supervision and their friendship.

The research work for this thesis was performed at LAS in close collaboration with the Institute for Synchrotron Radiation (ISS), also headed by Prof. Dr.rer.nat. T. Baumbach, at the Forschungszentrum Karlsruhe. Therefore, the author wants to thank all colleagues from ISS for their hospitality and support.

The author wants to thank especially the members of the three groups at LAS, ISS and the University of Erlangen-Nürnberg which closely collaborate i on the development of superconductive undulators: Dr. S. Casalbuoni (ISS), Dr. A. W. Grau (ISS), Dr. B. Kostka (University of Erlangen-Nürnberg), Dr. E. Mashkina (University of Erlangen-Nürnberg), Dr. D. Saez de Jauregui (ISS), Dr. P. Peiffer (LAS) and N. Vassiljev (University of Erlangen-Nürnberg) for their support.

The author also wants to thank the ANKA/ISS machine group for good collaboration and support, especially Dr. I. Birkel, Dr. E. Huttel and Dr. P. Wesolowski.

Special thanks goes to Dr. A.-S. Müller (ISS/LAS) for advice, support, scientific discussions and especially her friendship.

Over the past three years several students have contributed to the research work presented in this thesis. Therefore, the author wants to thank the students F. Burkart, S. Ehlers, G. Fuchert, D. Schörling and M.J. Wolf for their participation in data analyses and experiments and the excellent team work.

The author also wants to thank the colleagues from LAS: Dr. K. Eichhorn, M. Fischer, Dr. D. Grygoryev, Dr. I. Huber, M. Riotte, Dr. K. Sonnad, T. Ulyanenkova and Prof. emerit. Dr. H. Wondratschek for their support.

Special thanks goes to D. Erbe (ISS) and the workshop of the Institute for Physics II at the University of Erlangen (Prof. Dr.rer.nat. E. Steffens) for designing, fabricating and mounting the essential parts of the equipment for the performed proof of principal experiment on induction shimming.

The mock-up coil used in the experiment was built by Babcock Noell GmbH (BNG), Würzburg, Germany. The author wants to thank the colleagues Dr. C. Boffo, M. Borlein and Dr. W. Walter from BNG for their collaboration.

The induction shimming test device was produced by the company THEVA, Ismaning, Germany. The author wants to thank Dr. R. Semerad and Dr. W. Prusseit from THEVA for their openess, flexibility and the excellent collaboration.

Finally the author wants to thank his family, the friends from the SMD Karlsruhe and the Jesus-Bruderschaft Gnadenthal, the members of the music-team of the Laurentiuspfarrei Karlsruhe-Hagsfeld and of the Waldstadt Kammerorchester Karlsruhe, S. Rauh and M. Swoboda for their sustaining friendship, support, tolerance and patience over the past years.

BIBLIOGRAPHY

[ABB+80] A. S. Artamonov, L. M. Barkov, V. B. Baryshev, N. S. Bashtonoy, N. A. Vinokurov, E. S. Gluskin, G. A. Korniukhin, V. A. Kochubei, G. N. Kulipanov, N. A. Mezentsev, V. F. Pindiurin, A. N. Skrinsky, and V. M. Khorev. First results of the work with a superconducting “snake” at the VEPP-3 storage ring. *Nuclear Instruments and Methods*, 177:239–246, 1980.

[BCS57] J. Bardeen, L. N. Cooper, and J. R. Schrieffer. Theory of superconductivity. *Physical Review*, 108(5):1175, December 1957.

[Ber] A. Bernhard. private communication.

[Ber08] Axel Bernhard. Laminierter supraleitender Undulator. Erfindungsmeldung, August 2008.

[BHK+06] A. Bernhard, M. Hagelstein, B. Kostka, R. Rossmanith, T. Schneider, M. Weisser, D. Wollmann, T. Baumbach, E. Steffens, and G. Gerlach. Superconductive in-vacuum undulators. *IEEE Transactions on Applied Superconductivity*, 16(2):1228–1231, 2006.

[BK04a] Werner Buckel and Reinhold Kleiner. *Superconductivity*, chapter Introduction, pages 1–9. Wiley-VCH, 2004.

[BK04b] Werner Buckel and Reinhold Kleiner. *Superconductivity*, chapter Thermodynamics and Thermal Properties of the Superconducting State, pages 189–267. Wiley-VCH, 2004.

[BK04c] Werner Buckel and Reinhold Kleiner. *Superconductivity*, chapter Critical Currents in Type-I and Type-II Superconductors, pages 269–304. Wiley-VCH, 2004.

[BK04d] Werner Buckel and Reinhold Kleiner. *Superconductivity*, chapter Superconducting Elements, Alloys, and Compounds, pages 73–109. Wiley-VCH, 2004.

[BK04e] Werner Buckel and Reinhold Kleiner. *Superconductivity*, chapter Fundamental Properties of Superconductors, pages 11–71. Wiley-VCH, 2004.

[BKP+] A. Bernhard, B. Kostka, P. Peiffer, R. Rossmanith, D. Schoerling, M.J. Wolf, D. Wollmann, and T. Baumbach. Magnetic Field Analysis for the

ANKA Superconductive Undulator. *Nuclear Instruments and Methods in Physics Research A.* to be published.

[BM86] J. G. Bednorz and K. A. Mueller. Possible high T_c superconductivity in the Ba-La-Cu-O system. *Zeitschrift fuer Physik B*, 64:189, 1986.

[BPW08] Axel Bernhard, Peter Peiffer, and Daniel Wollmann. Shimming-Konzeptionen fuer die Projekte SCUW/SCU2. internal report, June 2008.

[BSMM01] I.N. Bronstein, K.A. Semendjajew, G. Musiol, and H. Muehlig. *Taschenbuch der Mathematik*, chapter Unbestimmte Integrale, page 1053. Verlag Harri Deutsch, 5th edition, 2001.

[BY01] C. Buzea and T. Yamashita. Review of the superconducting properties of MgB_2. *Superconductor Science and Technology*, 14:R115, 2001.

[BZJIW90] I. Ben-Zvi, Z.Y. Jiang, G. Ingold, and L.H. Wu. The performance of a superconductive micro-undulator prototype. *Nuclear Instruments and Methods in Physics Research A*, 297:301, 1990.

[CEC97] O. Chubar, P. Elleaume, and J. Chavanne. A 3D Magnetostatics Computer Code for Insertion Devices. *Proceedings of the SRI97 Conference, SPring8, Japan*, 1997.

[CHK$^+$06] S. Casalbuoni, M. Hagelstein, B. Kostka, R. Rossmanith, M. Weisser, E. Steffens, A. Bernhard, D. Wollmann, and T. Baumbach. Generation of x-ray radiation in a storage ring by a superconductive cold-bore in-vacuum undulator. *Physical Review Special Topics Accelerators and Beams*, 9:010702, 2006.

[Cla04a] J.A. Clarke. *The Science and Technology of Undulators and Wigglers*, chapter Synchrotron Radiation Output from Undulators, pages 52–83. Oxford Science Publication, 2004.

[Cla04b] J.A. Clarke. *The Science and Technology of Undulators and Wigglers*, chapter Measurement and Correction of Insertion Devices, pages 158–179. Oxford Science Publication, 2004.

[CRS$^+$03] S. Chouhan, R. Rossmanith, S. Strohmer, D. Doelling, A. Geisler, A. Hobl, and S. Kubsky. Field error compensation and thermal beam load in a supercondictive undulator. *Proceedings of the 2003 Partical Accelerator Conference*, pages 899–901, 2003.

[ECC97] P. Elleaume, O. Chubar, and J. Chavanne. Computing 3D Magnetic Fields from Insertion Devices. *Proceedings of the 1997 Partical Accelerator Conference, Vancouver*, 1997.

[Ell03] Pascal Elleaume, editor. *Workshop on superconducting Wigglers and Undulators*. ESRF, 2003.

[Far80] Y. Farge. Emission of photons by undulators. *Applied Optics*, 19:4021, 1980.

[HHM+99] T. Hezel, M. Homscheidt, H.O. Moser, R. Rossmanith, T. Schneider, H. Backe, S. Dambach, F. Hagenbuck, K.H. Kaiser, G. Kube, W. Lauth, A. Steinhof, and T. Walcher. Experimental results with a novel superconductive in-vacuum mini-undulator test device at the Mainz microtron MAMI. *Proceedings of the 1999 Particle Accelerator Conference*, (165-167), 1999.

[Hof04] Albert Hofmann. *The Physics of Synchrotron Radiation.* Cambridge University Press, first edition, 2004.

[IOR+98] T. Ishida, Kiichi Okuda, A. I. Rykov, S. Tajima, and I. Terasaki. In-plane anisotropy of vortex-lattice melting in large $YBa_2Cu_3O_7$ single crystals. *Physical Reviwe B*, 58(9):5222, 1998.

[Jac99a] J. D. Jackson. *Classical Electrodynamics.* John Wiley & Sons, Inc., third edition, 1999.

[Jac99b] J. D. Jackson. *Classical Electrodynamics*, chapter Magnetostatics, Faraday's Law, Quasi-Static Fields, pages 175–178. John Wiley & Sons, Inc., third edition, 1999.

[KO11] H. Kammerlingh-Onnes. Comm. Leiden, 1911.

[KRH+05] B. Kostka, R. Rossmanith, M. Hagelstein, T. Baumbach, A. Bernhard, M. Weisser, and E. Steffens. Generation of X-Ray radiation in a storage ring by a superconductive cold-bore in-vacuum undulator. *Physical Review Letters*, submitted, 2005.

[KSW91] Koch, Sasaki, and Winick. *Handbook on Synchrotron Radiation*, volume 3, chapter Synchrotron-radiation spectra, section Radiation from undulator magnets, pages 43–52. North-Holland, 1991.

[KSW00] Kories and Schmidt-Walter. *Taschenbuch der Elektrotechnik*, chapter Elektrische Felder, pages 88–89. Verlag Harri Deutsch, 2000.

[KT96] J. R. Kirtley and C. C. Tsuei. *Spektrum der Wissenschaft*, page 58, October 1996. German edition of Scientific American.

[Lab] Stanford Synchrotron Radiation Laboratory. http://www-ssrl.slac.stanford.edu/sr_sources.html.

[MD04] H.O. Moser and C.Z. Diao. Finite-Length field error and its compensation in superconducting miniundulators. *Nuclear Instruments and Methods, Section A*, (535):606–613, June 2004.

[MGS+08] Elena Mashkina, Andreas Grau, Theo Schneider, Axel Bernhard, Sara Casalbuoni, Michael Hagelstein, Barbara Kostka, Robert Rossmanith, Erhard Steffens, Daniel Wollmann, and Tilo Baumbach. CASPER - a magnetic measurement facility for superconducting undulators. *Journal of Physics: Conference Series*, 97, 2008.

[MKH91] H.O. Moser, B. Krevet, and H. Holzapfel. Mikroundulator. *Germ patent P 41 01 094.9-33*, Jan. 16 1991.

[MO33] W. Meissner and R. Ochsenfeld. Ein neuer Effekt bei Eintritt der Supraleitfaehigkeit. *Die Naturwissenschaften*, 21:787, 1933.

[Mos04] H.O. Moser. *Accelerator Physics, Technology, and Applications*, chapter A Guided Survey of Synchrotron Radiation Sources. Singapore, World Scientific Publishing, 2004.

[Mue05] A.-S. Mueller. Physik relativistischer Teilchenstrahlen. Lecture at the University of Siegen, SS 2005.

[MWY04] H.O. Moser, O. Wilhelmi, and P. Yang. *Accelerator Physics, Technology, and Applications*, chapter Introduction to Synchrotron Radiation Applications. Singapore, World Scientific Publishing, 2004.

[NNMZ01] J. Nagamatsu, N. Nakagawa, T. Muranaka, and Y. Zenitani. *Nature*, 410:63, 2001.

[NTME98] H. Nakagawa, T. Takamasu, N. Miura, and Y. Enomoto. DC and AC magneto-resistance measurement technique for$YBa_2Cu_3O_{7-\delta}$ thin films in megagauss fields. *Physica B*, 246:429, 1998.

[OE03] H. Onuki and P. Elleaume, editors. *Undulators, Wigglers and their Applications*, volume 1, chapter Technology of insertion devices, pages 148–213. Taylor & Francis, 2003.

[PDB+05] S. Prestemon, D. Dietderich, S. Bartlett, M. Coleman, S. Gourlay, A. Lietzke, S. Marks, S. Mattafirri, R. Scanlan, R. Schlueter, B. Wahrer, and B. Wang. Design, Fabrication, and Test Results of Undulators Using Nb_3Sn Superconductor. *IEEE Transactions on Applied Superconductivity*, 15(2):1236–1239, June 2005.

[Pfl05] J. Pflueger. Undulator systems for the X-FEL. *International Workshop on Undulator Systems for Free Electron Lasers, DESY, Hamburg, Germany*, 2005.

[PLT99] J. Pflueger, H. Lu, and T. Teichmann. Field fine tune by pole height adjustment for undulator of the TTF-FEL. *Nuclear Instruments & Methods in Physic Research*, A429:368–391, 1999.

[PWBF08] Peter Peiffer, Daniel Wollmann, Axel Bernhard, and Golo Fuchert. Phase errors from systematic distributions of mechanical errors. internal report, Oktober 2008.

[RMG+02] R. Rossmanith, H.O. Moser, A. Geisler, A. Hobl, D. Krischel, and M. Schillo. Superconductive 14 mm period undulators for single pass accelerators (fels) and storage rings. *Proceedings of EPAC 2002*, (2628-2630), 2002.

[RSSI90] B. Roas, L. Schultz, and G. Saemann-Ischenko. Anisotropy of the critical current density in epitaxial $YBa_2Cu_3O_x$ films. *Physical Review Letters*, 64(4):479–482, 1990.

[Sak67] J. J. Sakurai. *Advanced Quantum Mechanics*, chapter Classical Fields, pages 1–19. Addison-Wesley Publishing Company, 1967.

[TK] T. Tanaka and H. Kitamura. SPring-8/RIKEN. http://radiant.harima.riken.go.jp/spectra.

[Vac01] Vacuumschmelze. Weichmagnetische Kobalt-Eisen-Legierungen. http://www.vacuumschmelze.de//dynamic/docroot/medialib /documents/broschueren/htbrosch/Pht-004_d.pdf, 2001.

[VF] UK Vector Fields, Oxford. OPERA-3D.

[WBC+06] Daniel Wollmann, Axel Bernhard, Sara Casalbuoni, Michael Hagelstein, Barbara Kostka, Robert Rossmanith, Matthias Weisser, Erhard Steffens, Gerald Gerlach, and Tilo Baumbach. A concept on electric field error compensation for the ANKA superconducting undulator. In *Proceedings of EPAC 2006, Edinburgh, Scotland*, pages 3577–3579, 2006.

[WBP+08a] D. Wollmann, A. Bernhard, P. Peiffer, T. Baumbach, E. Mashkina, A. Grau, and R. Rossmanith. Experimental Demonstration of the Induction-Shimming Concept in Superconductive Undulators. *Physical Review Special Topics Accelerators and Beams*, 2008. submitted.

[WBP+08b] D. Wollmann, A. Bernhard, P. Peiffer, T. Baumbach, and R. Rossmanith. Induction-Shimming: a new shimming-concept for superconductive undulators. *Physical Review Special Topics Accelerators and Beams*, 11:100702, 2008.

[WBP+08c] D. Wollmann, A. Bernhard, P. Peiffer, R. Rossmanith, and T. Baumbach. A new concept for reducing phase errors in superconductive undulators: induction-shimming. In *Proceedings of EPAC08, Genoa, Italy*, pages 2323–2325, 2008.

[WBR08] D. Wollmann, A. Bernhard, and R. Rossmanith. Induction shimming. German patent, June 2008. pending.

[Wie03a] Helmut Wiedemann. *Particle Accelerator Physics I*, chapter Synchrotron Radiation, pages 300–336. Springer, second edition, 2003.

[Wie03b] Helmut Wiedemann. *Particle Accelerator Physics I*. Springer, second edition, 2003.

[Wie03c] Helmut Wiedemann. *Particle Accelerator Physics II*. Springer, second edition, 2003.

[Wil] Klaus Wille. Vorlesung zur Physik der Teilchenbeschleuniger. Lecture at the University of Dortmund.

[Wil92a] Klaus Wille. *Physik der Teilchenbeschleuniger*, chapter Synchrotronstrahlung, pages 36–49. B. G. Teubner Stuttgart, 1992.

[Wil92b] Klaus Wille. *Physik der Teilchenbeschleuniger*. B. G. Teubner Stuttgart, 1992.

[Wil92c] Klaus Wille. *Physik der Teilchenbeschleuniger und Synchrotronstrahlungsquellen*, chapter Wiggler und Undulatoren, pages 249–266. Teubner Stuttgart, 1992.

[Wol05] Daniel Wollmann. Reduktion des Phasenfehlers eines Supraleitenden Undulators. Master's thesis, Technische Universitaet Dresden, Germany, 2005.

[Zha02] X.-C. Zhang. Terahertz wave imaging: horizons and hurdles. *Physics in Medicine and Biology*, 47:3667–3677, 2002.

LIST OF FIGURES

LIST OF TABLES

APPENDIX

A. PHASE ERROR DERIVATION

The phase error can be derived from the equations of motion, as discussed in section 2.2 [Wil].
From the magnetic field of the undulator

$$\mathbf{B} = \begin{pmatrix} 0 \\ B_y(z) \\ 0 \end{pmatrix}$$

with $B_y(z) = \tilde{B}cos(\frac{2\pi}{\lambda_u}z)$, and the Lorentz-force

$$\mathbf{F} = m_e\gamma\dot{\mathbf{v}} = -e\mathbf{v} \times \mathbf{B},$$

the equation of motion for the electron is

$$\begin{pmatrix} \ddot{x} \\ 0 \\ \ddot{z} \end{pmatrix} = -\frac{e}{m_e\gamma}\begin{pmatrix} -\dot{z} \cdot B_y \\ 0 \\ -\dot{x} \cdot B_y \end{pmatrix}.$$

Integration of

$$\ddot{x} = \frac{e}{m_e\gamma}B_y\frac{dz}{dt},$$

leads to

$$\dot{x} = \int\limits_{t_0}^{t} \ddot{x} \cdot dt' = \frac{e}{m_e\gamma}\int\limits_{z_0}^{z} B_y(z')dz' = \frac{e}{m_e\gamma}I_1(z), \tag{A.1}$$

for $\dot{x}(t_0) = 0$. $I_1(z)$ is a periodic function in z.
The relativistic factor γ is

$$\gamma = \sqrt{\frac{1}{1-\left(\frac{|\mathbf{v}|}{c}\right)^2}}.$$

With $|\mathbf{v}|^2 = \dot{x}^2 + \dot{z}^2$ and $\frac{1}{\gamma^2} \ll 1$

$$\begin{aligned} \dot{z} &= \sqrt{c^2\left(1-\frac{1}{\gamma^2}-\frac{\dot{x}^2}{c^2}\right)} \\ &= \sqrt{c^2\left(1-\frac{1}{\gamma^2}-\left[\frac{e}{m_ec\gamma}I_1(z)\right]^2\right)} \\ &\approx c\sqrt{\left(1-\left[\frac{e}{m_ec\gamma}I_1(z)\right]^2\right)}. \end{aligned} \tag{A.2}$$

The slip between an electron and a light-wave is defined as:

$$s(z) := c \cdot [t_e(z) - t_L(z)].$$

Here, t_e is the time, that an electron needs to travel to a longitudinal position z. With the length $L(z)$ of the electron trajectory this translates into

$$t_e(z) = \frac{L(z)}{|\mathbf{v}|}. \tag{A.3}$$

t_L is the time, that a light-wave needs to travel to a longitudinal position z, i.e.

$$t_L(z) = \frac{z}{c}.$$

Considering the two previous equations the slip becomes (see figure 2.12)

$$s(z) = \frac{L(z)}{\frac{|v|}{c}} - z. \tag{A.4}$$

Transforming equation (A.3), the length of the electron trajectory can be described as

$$L(z) = \int\limits_{t_0}^{t} |\mathbf{v}| dt'.$$

Considering

$$dt = \frac{dz}{\dot{z}},$$

applying equation (A.2) and assuming that in first order approximation $|\mathbf{v}| \approx c$, the length of the electron trajectory becomes

$$L(z) = c \int\limits_0^z \frac{1}{\dot{z}'} dz' = \int\limits_0^z \frac{1}{\sqrt{1 - \frac{\dot{x}^2}{c^2}}} dz'.$$

Using equation (A.1) leads to

$$\begin{aligned} L(z) &= \int\limits_0^z \left(\frac{1}{\sqrt{1 - (\frac{e}{m_e c \gamma} I_1(z))^2}} \right) dz' \\ &= \int\limits_0^z \left(1 + \frac{1}{2} [\frac{e}{m_e c \gamma} I_1(z)]^2 + O(\frac{1}{\gamma^4}) \right) dz' \\ &\approx z + \frac{1}{2} (\frac{e}{m_e \gamma c})^2 \int\limits_0^z [I_1(z')]^2 dz'. \end{aligned} \tag{A.5}$$

With $J(z) = \int\limits_0^z [I_1(z')]^2 dz'$ and applying equation (A.5) to equation (A.4) the slip between an electron and a light-wave becomes

$$\begin{aligned} s(z) &= \frac{z + \frac{1}{2}(\frac{e}{m_e c\gamma})^2 J(z)}{\frac{|\mathbf{v}|}{c}} - z \\ &= \frac{z + \frac{1}{2}(\frac{e}{m_e c\gamma})^2 J(z)}{\frac{|\mathbf{v}|}{c}} - \frac{z\frac{|\mathbf{v}|}{c}}{\frac{|\mathbf{v}|}{c}} \\ &= \frac{z(1 - \frac{|\mathbf{v}|}{c}) + \frac{1}{2}(\frac{e}{m_e c\gamma})^2 J(z)}{\frac{|\mathbf{v}|}{c}}. \end{aligned}$$

Assuming

$$\begin{aligned} \gamma^2 &= \frac{1}{1 - \left(\frac{|\mathbf{v}|}{c}\right)^2} \\ \rightarrow \frac{1}{\gamma^2} &= 1 - \left(\frac{|\mathbf{v}|}{c}\right)^2 = (1 - \frac{|\mathbf{v}|}{c})(1 + \frac{|\mathbf{v}|}{c}) \end{aligned}$$

the slip can be rewritten as

$$\begin{aligned} s(z) &= \frac{\frac{z(1-\frac{|\mathbf{v}|}{c})(1+\frac{|\mathbf{v}|}{c})}{(1+\frac{|\mathbf{v}|}{c})} + \frac{1}{2}(\frac{e}{m_e c\gamma})^2 J(z)}{\frac{|\mathbf{v}|}{c}} \\ &= \frac{\frac{z}{\gamma^2(1+\frac{|\mathbf{v}|}{c})} + \frac{1}{2}(\frac{e}{m_e c\gamma})^2 J(z)}{\frac{|\mathbf{v}|}{c}}. \end{aligned}$$

Applying $|\mathbf{v}| \approx c$ yields

$$\begin{aligned} s(z) &= \frac{z}{2\gamma^2} + \frac{1}{2}(\frac{e}{m_e c\gamma})^2 J(z) \\ &= \frac{1}{2\gamma^2}\left(z + (\frac{e}{m_e c})^2 J(z)\right) \end{aligned} \tag{A.6}$$

The phase difference between photon and electron $\Phi(z)$, in radians is defined as the difference between $s(z)$ in units of the light wavelength λ_L and the z in units of the undulator period length λ_u:

$$\Phi(z) := 2\pi\left(\frac{s(z)}{\lambda_L} - \frac{z}{\lambda_u}\right).$$

Applying equation (2.10) with $k = 1$ and $\Theta = 0$:

$$\lambda_L = \frac{\lambda_u}{2\gamma^2}(1 + \frac{K^2}{2}),$$

and equation (A.6) the phase difference between photon and electron becomes

$$\begin{aligned}\Phi(z) &= 2\pi\left(\frac{\frac{1}{2\gamma^2}\left(z+(\frac{e}{m_e c})^2 J(z)\right)}{\frac{\lambda_u}{2\gamma^2}(1+\frac{K^2}{2})} - \frac{z}{\lambda_u}\right)\\ &= \frac{2\pi}{\lambda_u}\left(\frac{2\left(z+(\frac{e}{m_e c})^2 J(z)\right) - z(2+K^2)}{2+K^2}\right)\\ &= \frac{2\pi}{\lambda_u}\left(\frac{2(\frac{e}{m_e c})^2 J(z) - K^2 z)}{2+K^2}\right).\end{aligned}$$

Finally, to achieve equation (2.11), which is the phase difference between photon and electron for the half period i of an undulator with n periods, the substitution $z = z_i - z_0$, with $i = (1...2n)$ leads to

$$\Phi_i = \frac{2\pi}{\lambda_u}\left(\frac{2(\frac{e}{m_e c})^2 J(z_i - z_0) - (z_i - z_0)K^2}{2+K^2}\right).$$

B. SIMULATION WITH OPERA-3D

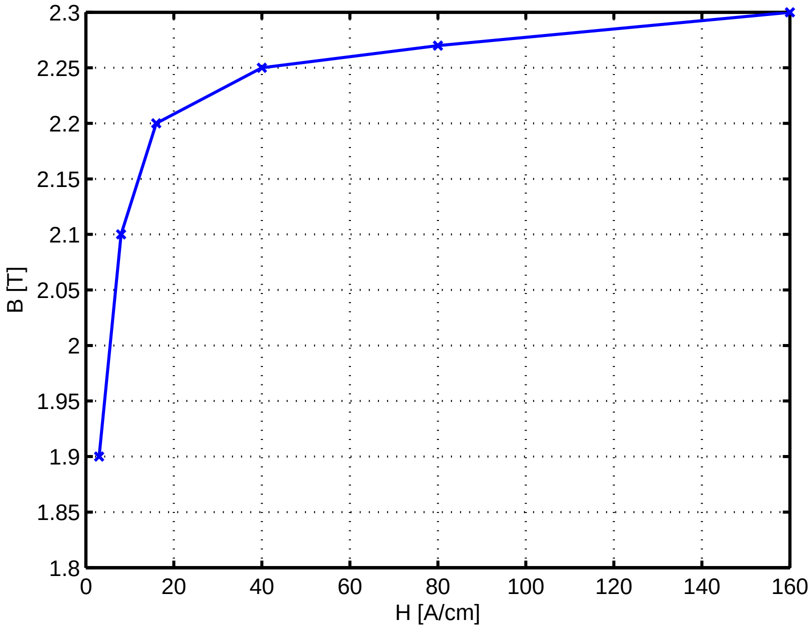

Fig. B.1: Vacoflux BH curve. [Vac01]

B [T]	H [A/cm]
1.9	3
2.1	8
2.2	16
2.25	40
2.27	80
2.3	160

Tab. B.1: Vacoflux50 BH data. [Vac01]